NOVEL DESIGN AND ANALYSIS OF PARALLEL

ROBOTIC MECHANISMS

ZHONGXING YANG

A DISSERTATION SUBMITTED TO

THE FACULTY OF GRADUATE STUDIES

IN PARTIAL FULFILLMENT OF THE REQUIREMENTS

FOR THE DEGREE OF

DOCTOR OF PHILOSOPHY

GRADUATE PROGRAM IN MECHANICAL ENGINEERING

YORK UNIVERSITY

TORONTO, ONTARIO

AUGUST 2019

ABSTRACT

A parallel manipulator has several limbs that connect and actuate an end effector from the base. The design of parallel manipulators usually follows the process of prescribed task, design evaluation, and optimization. This dissertation focuses on interference-free designs of dynamically balanced manipulators and deployable manipulators of various degrees of freedom (DOFs).

1) Dynamic balancing is an approach to reduce shaking loads in motion by including balancing components. The shaking loads could cause noise and vibration. The balancing components may cause link interference and take more actuation energy. The 2-DOF (2-$\underline{R}$R)R or 3-DOF (2-$\underline{R}$R)R planar manipulator, and 3-DOF 3-$\underline{R}$RS spatial manipulator are designed interference-free and with structural adaptive features. The structural adaptions and motion planning are discussed for energy minimization. A balanced 3-DOF (2-$\underline{R}$R)$\underline{R}$ and a balanced 3-DOF 3-$\underline{R}$RS could be combined for balanced 6-DOF motion.

2) Deployable feature in design allows a structure to be folded. The research in deployable parallel structures of non-configurable platform is rare. This feature is demanded, for example the outdoor solar tracking stand has non-configurable platform and may need to lie-flat on floor at stormy weathers to protect the structure. The 3-DOF 3-$\underline{P}$RS and 3-DOF 3-R$\underline{P}$S are re-designed to have deployable feature. The 6-DOF 3-[(2-$\underline{R}$R)UU] and 5-DOF PR$\underline{P}$U/2-[(2-$\underline{R}$R)UU] are designed for deployable feature in higher DOFs. Several novel methods are developed for rapid workspace evaluation, link interference detection and stiffness evaluation.

The above robotic manipulators could be grouped as a robotic system that operates in a green way and works harmoniously with nature.

ACKNOWLEDGEMENT

"I will extol the LORD at all times; His praise will always be on my lips." -Psalm 34:1 NIV.

I would like to thank my supervisor, Dr. Dan Zhang for all the supports that guide me to discover the beauty of robotics. His bountiful knowledge and state-of-the-art teaching shine the light on my road to research.

I would like to thank my supervisory committee members, Dr. Alex Czekanski and Dr. George Zhu, the external examiner, Dr. Siyuan He, and internal examiner, Dr. Jinjun Shan, for their inspiring questions and constructive advices that bless me and help me grow precious fruits from my PhD studies.

I would like to thank all the colleagues of the Advanced Robotics and Mechatronics Lab for peer support in exploring the marvelous world of robotics.

A warm thanks to my family and friends for their hugs and a relationship of love.

TABLE OF CONTENTS

LIST OF TABLES

LIST OF FIGURES

Chapter 1 Introduction

1.1 Robotics

Robots are controlled machines. The English word "Robot" originates from Czech word "Robota" which means forced labor. Czech writer Karel Čapek firstly used word "Robot" in his 1921 play Rossum's Universal Robots for mechanical men made and controlled to do work in factories. They finally rebelled against their human masters [1]. Robotics is the science and technology of robots. Since robotic science was introduced, it rapidly attracted research interests and grew broadly. Now robots are widely used for many applications [2].

As influenced by science fictions and public media, general public more often may think of robots as machines with human appearance that replace human labor. The robots that look like human are humanoid robots [3]. However, the robots don't necessarily have to look like human.

Jorge Angeles classified robots as mobiles and manipulators [4]. Mobile robots move around, such as the four-legged walking robot, Big Dog [5], swimming robotic fish [6], winged flying robots [7] and so on. The manipulators need to be installed on stage and are designed to reach to places with a moving end effector like the arm and hand.

Usually a manipulator has three parts: a moving end effector, a base, and some links that connect and actuate the end effector from the base. A moving or static object where the manipulator is installed on could be considered as a base. Jonathan Hodgins designed a manipulator to be installed on the bottom of drones [8]. Moritz Arns designed a dual functioning landing gear for the drones [9]. The CANADARM was designed to be sent to work in space [10]. The manipulators could also

be installed on fixed base. Industrial robots [11] are set along the production line to work on the work parts conveyed on the line.

Structures of the manipulators could be generally classified as serial and parallel. A serial robot has its links connected from base to the moving end effector in series like an arm. The design is straightforward and commonly seen. A planar serial robot is designed with three revolute joints perpendicular to the plane which could move horizontally and longitudinally on the plane and rotate as well [12]. A SCARA robot [13] adds one more joint to the three-mobility planar serial robot and makes it move vertically.

Another kind of manipulator structure is parallel.

1.2 Parallel Robots

Dan Zhang gives a review of advanced parallel robots, and he develops comprehensive design and analysis methodologies for parallel manipulators of multiple limbs and mobilities [14]. A limb is a group of jointed links. The parallel manipulators have several limbs that connected in parallel between two platforms. The fixed platform is the base, and the moving platform is the end effector.

An example of planar fully parallel manipulator [15] 3-$\underline{R}$RR has three legs each with one actuator. This robot has three mobilities that could move horizontally and longitudinally on a plane and rotate.

Compared to serial manipulators, the parallel manipulators have higher stiffness, loading capacity, operational precision, but smaller workspace. These structures are widely applied in many industries, such as training, surgical, manufacturing and so on [16].

As parallel structure has high stiffness while serial structure has large workspace. The parallel features and serial features could be integrated to design a hybrid manipulator [17] to take advantages of both.

Historically there were quite some mechanisms or machines designed with parallel nature, however D. Stewart firstly raised the awareness of parallel mechanism in academic research. Since D. Stewart published a significant fully parallel structure in 1965 named Stewart platform that has six mobilities [18], the researches on parallel robotic structures started to bloom.

In the kingdom of parallel manipulators, there are unique categories of designs. The parallel limbs could be flexible, such as the cable driven parallel manipulators [19] where the flexible cables pull and lift a moving platform. For some designs and applications, the moving platform doesn't need to be one rigid body. A configurable platform could be composed by more than one jointed body, so that the platform could change its shape [20] [21] [22]. The limbs of the parallel manipulators may not be individually connected between base and platform, for some structures have chains that connect between two limbs [23] [24].

The parallel structures discussed in this dissertation are the ones that have one rigid platform (non-configurable platform), have the limbs that are individual with no chains between them. The limbs are considered as a group of rigid bodies jointed together (non-cable driven) in kinematics and dynamics analysis. However, in stiffness analysis, the elasticity in actuated joints or deformable bodies are considered.

1.3 Objectives of the Study

Here are some important problems in the studies of parallel manipulators for further improvements.

The parallel manipulators contain a group of rigid bodies with mass and rotational inertia. When the manipulator is moving, the acceleration of the mass and rotational inertia could cause inertia loads. That could lead to vibration and noise. These loads are known as shaking forces and shaking moments. The elimination of these loads is known as dynamic balancing [25]. The balancing requires additional components which could have link interference and take more driving energy. Methods need to be discussed to design balanced manipulators with easier control, improved balancing performance, interference-free, optimized energy consumption, and larger workspace. This problem is important as it is about the precision and energy-saving of manufacturing.

The outdoor stormy weathers or compact indoor manufacturing tasks require parallel manipulators to be folded close to the base to protect the structure or to give space to other components. There are some researches on foldable parallel manipulators designs, but these parallel structures are of configurable platform. Parallel structures of non-configurable platform are demanded in applications. The researches of foldable designs for non-configurable platform manipulators are rare. The modification and re-design of some common parallel manipulators to be foldable need be discussed and novel designs with this feature will be developed. This feature is worth research awareness as it provides a protection for outdoor working machines in severe weathers.

The parallel manipulators have multiple limbs and these limbs are very close to each other. When the manipulator is actuated, these limbs may collide or interfere. The distance between the limbs need to be calculated to determine whether any two bodies may interfere with each other. The

interference detection of limbs could be complex and take time for analysis. Parallel structures need to be designed with less opportunity of interference and quick detection for potential interference. This is significant for parallel manipulators of higher mobilities since they contain more links between the platform and the base than the ones of lower mobilities. This problem will be discussed in the dynamically balanced manipulators and deployable manipulators.

1.4 Organization of the Dissertation

Chapter 1 gives a general knowledge of robotics and introduces the important problems the research of this dissertation is going to solve.

Chapter 2 reviews the knowledge and researches that are relevant to the problems. This provides the knowledge background to readers and it paves the way for the methods to be discussed in the next chapter.

Chapter 3 discusses the research challenges, describes the problems in more details and suggests the methods and theories that could be developed or used to address the problems.

Chapter 4 deals with designs of dynamically balanced parallel manipulators. It demonstrates the dynamic balancing and energy optimization methods for a planar parallel mechanism and then expands the methods to design and optimize a spatial dynamically balanced mechanism. Structural adaption and motion planning are involved in the energy optimization. The dynamic modeling in theory are verified by Simulink. It also discusses the further combination of two balanced mechanisms to make a balanced manufacturing machine of higher mobilities. Chapter 4 is written

according to author's papers on 2-DOF (2-$\underline{R}$R)R [26] and 3-DOF 3-$\underline{R}$RS [27], including materials from the sources with adaptions.

Chapter 5 deals with re-designs of some common low-mobility parallel manipulators. It analyzes the function that is designed to fold parallel mechanisms. It looks at the stormy weather protection for solar panel in solar tracking and presents the designs that enable the mechanisms to lie down flat to the floor when storm attacks the tracking field. The foldable designs are analysed for parallel mechanisms with three mobilities (two rotations and one translation). Methods such as minimum platform height and modified Jacobian matrix are developed to assist the analysis and evaluation of the designs. Chapter 5 is written according to author's papers on 3-DOF 3-$\underline{P}$RS [28] and 3-DOF 3-R$\underline{P}$S [29], including materials from the sources with adaptions.

Chapter 6 deals with novel designs of high-mobility parallel manipulators. It expands the foldable mechanism designs to higher mobilities. The synthesis design methods and interference avoidance/detection methods are researched. Modified Jacobian matrix is developed for these structures. Chapter 6 is written according to author's papers on 6-DOF 3-[(2-$\underline{R}$R)UU] [30] and 5-DOF PR$\underline{P}$U/2-[(2-$\underline{R}$R)UU] [31], including materials from the sources with adaptions.

Chapter 7 concludes the contribution of the dissertation and looks forward to future work.

Chapter 2 Literature Review

2.1 Synthesis Methodology

Tingli Yang et al [32] summarized the general process of manipulator design. As a manipulator is designed to work within designed space, first the task space is given, then a design comes up with a solution space, and finally the solution space is going to be optimized. The key factors of topology are joints, the connection of links by joints, and the constraint a joint implies on the links. The motion of links connected in series is the composition of the motions of these joints, while the motion of platform connect to the base by a group of limbs in parallel is the intersection of the motions of the limbs. A group of links connected in series is a single open chain unit. The single open chain units are easy and simple to analyze and use for design. It is common to use single open chain units as one of multiple limbs for a parallel manipulator.

Dan Zhang [14] developed tables of topologies for parallel manipulators with open chain units based on the Chebychev-Grübler-Kutzbach criterion. He summarized in the table the number of mobilities a topology could achieve with various possibilities of legs and joints combination. From this table, he continues to develop the parallel structures with one more leg than mobilities, so the extra leg could serve as an unactuated passive leg which enhances the stiffness and kinematic analysis of the structures. A passive leg determines and provides decoupled motion when the other legs have full mobilities of six because the motion of parallel limbs is the intersection of their motions. A family of parallel manipulators are designed with the passive leg [33] [34] [35], where the passive leg determines the total mobility of the parallel mechanisms considering the

7

intersection nature of the parallel mechanism motions. He also suggests the combination of manipulators to work beyond the mobilities of individual robots that involve in the combination.

After a mechanism is designed, its mobility also known as degree of freedom (DOF) needs to be determined. The formula developed based on Chebychev-Grübler-Kutzbach criterion are simplified called G-K formula. The G-K formula could easily be used to determine the degree of freedom based on number of links, number of joints, total mobilities of all joints [17].

A classical G-K formula is given below, where M represents the degrees of freedom, C is 3 for planar mechanism or 6 for non-planar mechanism, B is the number of bodies, J is the number of joints, and $\sum_{i=1}^{J} d_i$ represents the total degrees of freedom from all the joints in the mechanism.

$$M = C(B - J - 1) + \sum_{i=1}^{J} d_i \qquad (2.1.1)$$

Classical G-K formula is commonly known, and widely adopted by engineers and educators [36] [37]. The G-K formula is easy to use and gives quick and correct solution for most of the cases. However, in some special mechanisms, many researches discovered that the classical G-K formula didn't give correct solution for mobilities. For some circumstance, the G-K formula needs to be modified for certain usages [38].

Zheng Huang et al [39] reviewed the 150 years of history seeking a unified formula for mobilities (DOF). He concludes that G-K formula is not correct in all cases while a unified formula for mobilities is not found yet. He suggested his research based on screw theory and he also classified other categories of methods.

There is a category of methods based on Jacobian matrix [40]. Although Jacobian matrix is complex, it does not increase the calculation work because Jacobian matrix is also needed for

stiffness mapping [41] which is commonly conducted to evaluate the deformation under loading. The rank of the Jacobian matrix represents the mobility of the mechanism [42]. Some research uses lie group theory to design a mechanism and then use Jacobian matrix to determine the actuation joints [43]. This is an alternative of verifying mobility with Jacobian matrix.

After a designed mechanism has its mobility verified, a topology diagram and a notation in letters with signs are needed to represent this structure. Network diagram [44] [45] of circles connected by lines is common in representing structure, where the circles represent rigid bodies and the lines represent the joints that connect the bodies. Another diagraming method [46] also takes the network pattern but more specifically indicates the orientation of joints, which is not commonly used. There are generally two notation methods to indicate the structure. One method [47] is defining the structure by the output of end motion of platform in a given sequence (for example: 2R1T or 2T1R as the first or second types of Gf motion set). This method clearly shows the degree of freedom and motions of the structure however doesn't give details of how the links are connected. Another method [14] is defining the joints in sequence from base to platform where the numbers with hyphen followed by joints indicate the duplicate or identical chains in parallel (for example 3-RRR or 6-UPS as the name and order of the joints connection where the underlined joint is driven). For the cases when the limbs are not identical or when it is a hybrid limb, one could consider using the notation in [48], where the bracket holds a part in serial connection and slash indicate a non-identical chain is connected from base to platform in parallel (for example RRR/(2-RRR)R is the notation for the structure in figure 2.3.1 (e)). This method indicates how the links are connected but doesn't give information on the motions at the end effector. One may need to use both notations (end effector motion and links connection) to comprehensively describe a structure. One needs to notice some joints could be combined to equal to another joint. For

example, RRR or RU when their rotation axis intersect at one point could be equal to spherical joint. Sometimes, such replacement brings a better performance.

2.2 Family of 2R1T Manipulators

Newly developed structures may be uncertain in performance, which may need long term trial and modification before commercial usage.

Family of 2R1T robots could make two rotations and one translation in any order. Some of the examples have been developed long ago and already widely applied. It is safer to adopt or modify the commonly known structures, as the relevant technical documents are abundant.

QinChuan Li et al [49] reviewed a group of parallel manipulators of 2R1T motion and classified them into four categories according to the order of equivalent joint outputs from base to the moving platform. These are the motions equivalent to UP, P*U*, PU and RPR. Most of the existent 2R1T robots belong to one of the four types.

The UP type equals a universal joint and a prismatic joint connected in the given sequence. An example is the Tricept robot with a passive leg to constraint the motion as UP [50].

The P*U* type is close to a prismatic joint and a universal joint connected in the given sequence but with coupled translational motions. Examples are A3 and Z3 sprint heads for manufacturing [51]. This type includes many well known and adopted structures such as 3-PRS, 3-RPS, 3-RRS and so on.

The PU type equals to a prismatic joint and a universal joint connected in the given sequence. There are some examples designed with a passive leg that constraints the moving platform as to yield a PU output [52] [34] [53].

The PRP type equals to a prismatic joint, a revolute joint and another prismatic joint connected in the given sequence. One example is the Exechon machine [54].

The research [49] further analyzed the designs with or without the constraining passive leg. Theoretically the machines with constraining passive leg could output the motion equivalent to the joints connected in series, while the ones without constraining passive leg yield coupled motions, also known as parasitic motions. However, in reality, the platform has a thickness. For example, the end effector of a PU type has a distance away from the center of the last joint on the constraining leg, U joint. In other words, the platform centre is not exactly the joint center. Optimization could minimize the deviation but could not eliminate it.

Researches [49] and [14] reviewed many examples of designs and suggested the trend in 2R1T robot design. That leads to the combination of a 2R1T robot with a planar manipulator which has at least two motions (the x and y axis motions on the plane). The merits of the combination are first, to provides an offset to cancel the deviation motions in the 2R1T manipulator, and second, to add at least two translational motions to make the pair of robots eligible for at least five degrees of freedom.

There are plenty of common 2R1T structures. They could be modified to improve the performance.

2.3 Hybrid Structures

Dan Zhang [14] described the beauty of hybrid structures which integrate the parallel and serial structures for the beneficial natures of both. The parallel robots have higher stiffness while the serial robots have larger working space. Serdar Küçük [17] described the features of fully serial, fully parallel and hybrid manipulators. Examples of planar 3-DOF mechanisms are given [55] in fully serial, fully parallel and hybrid structures respectively.

As is summarized from review of many hybrid designs, there are mainly two types of hybridizing. These are the serial type hybridizing and parallel type hybridizing based on the pattern of how sub-mechanisms are connected into the manipulator.

The serial type hybridizing means connecting mechanisms or manipulators in series, just like the serial manipulator that connects the links in series. For example, the parallel robots and serial robots could be connected in series as in [55] [56]; and multiple parallel robots could be connected in series [57]; a parallel robot and a single joint could be connected in series [58] [59].

The parallel type hybridizing means connecting limbs in parallel between the moving platform and the base, where at least one limb contains at least two actuators. The limb that contains at least two actuators is similar with serial mechanisms. For example, some 6-DOF manipulators are composed of three limbs where each limb has links and joints connected in series and two joints of each limb are driven [60] [61] [62] [63] [64] [65].

For when a limb has two actuated joints in series the actuated joint, closer to base, needs to carry the load of the actuator in the middle of the limb. This requires more driving capability and larger size of the base actuators. So that, some researches discuss the parallel type hybridizing with limb that contains at least two driven joints, but the driving joints are in parallel [66] [48] [67] [68].

This is equivalent to a serial limb but the parallel driving provides a better driving loads distribution and a better mass distribution.

The figure 2.3.1 gives examples of 3-DOF planar manipulators in different formation. Sub-figure (d) and (e) are equivalent, but (e) uses parallel actuation which avoids heavy duty on base actuator and uneven mass distribution, besides, the force normal to the plane at end effector causes less deformation because the cantilever is stronger with parallel actuation.
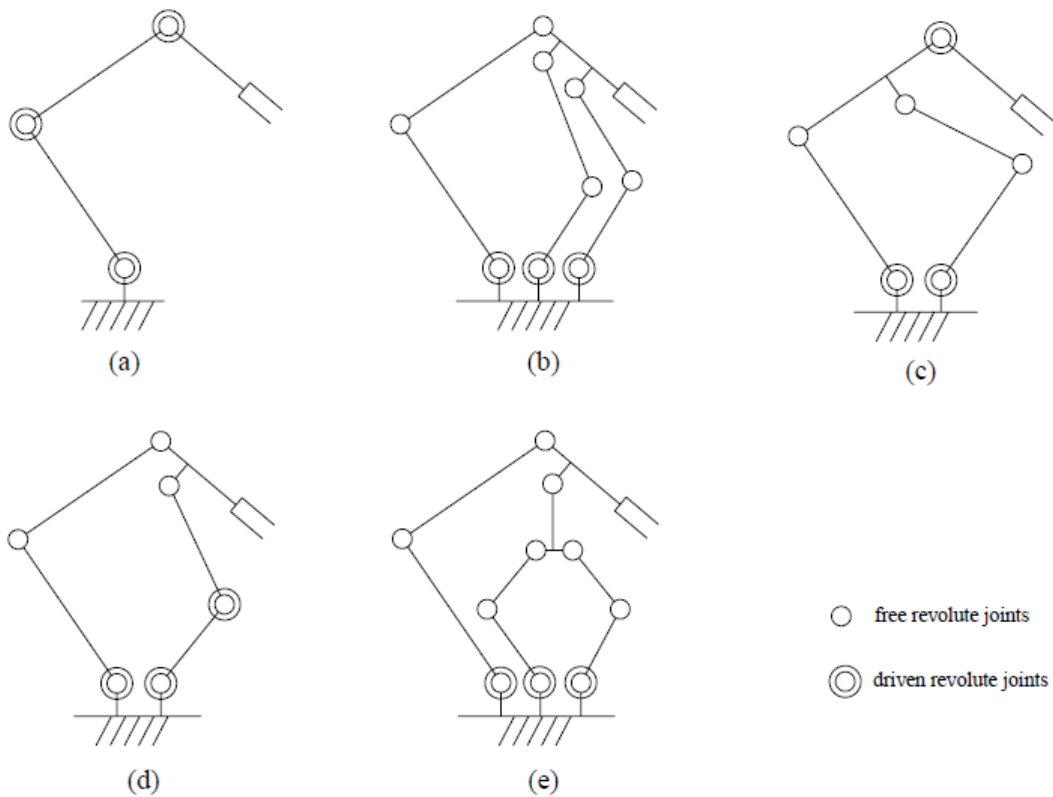
Figure 2.3.1 The 3-DOF planar mechanisms. (a) fully serial; (b) fully parallel; (c) hybrid serial type; (d) hybrid parallel type; (e) equivalent parallel actuation of hybrid parallel type.

The hybrid structures designed for higher degrees of freedom have a design merit which reduces the chances of link interference [60] [62] [64] [69] [65] [67] compared to the equivalent fully parallel counterparts, because the hybrid structures are simpler than equivalent fully parallel structures. This reduces the chances of interferences and offers a larger workspace.

2.4 Redundancy and Adaption

Joints bring degrees of freedom to a mechanism, but the added DOF may not contribute to add dimensions in end effector motions. For example, a serial open chain on a plane could at most translate in x and y and rotate about z axes, while adding more prismatic joints on that plane increases the DOF but doesn't make it a spatial mechanism. When joints provide redundant motions, they need to be locked or driven to eliminate idle motions. The redundancy describes this feature of structure where the number of actuators exceeds the degrees of freedom [14].

Some works have reviewed the redundancy in parallel robot design [70] [71] [72] [73]. Among the works, [72] has summarized that there are three types of redundancy. It gave the design process for redundancy as 1) original non-redundant structure, 2) modification, 3) geometric parameters to be chosen (set redundancy) to optimize some performances.

The three types of redundancy are described as following.

(a) Kinematic redundancy by definition [74] adds more degree of freedom through joints to the limbs and it needs actuators to control the additional degree of freedom. Benefits and applications are in eliminated singularity [75], improves dynamic performances [76] [77], optimized force distribution [78], and reduced operational gap [79].

(b) Actuation redundancy by definition [80] [81] doesn't add more degree of freedom but uses actuators on originally passive joints or adds additional actuated limb(s). Benefits and applications are in eliminated singularity, improved force and dynamic performances [82] [80] and tuned natural frequency [83].

(c) Internal redundancy by definition [72] is the additional degree of freedom which allows some mass to move for better dynamic performances, while the relative motion between the base and the moving platform is not affected by this redundancy. The counter mass position is adjusted for balancing [84]. Mass moving for balancing [85]. (See more examples in the active dynamic balancers). Parallel robot dynamic performance can be improved by reconfiguration, known as re-dyn [86] [87].

These types of redundancy are compared for their different properties. The actuation redundancy adds constraint to the motion thus is more difficult to control. The internal redundancy may involve additional motors and mass on a limb. The kinematic redundancy could be considered to allow adaption in design.

The adaption [88] and reconfiguration [89] though the redundancy improves the performances. The design could be modified from originally non-redundant structures for optimization.

2.5 Kinematics and Dynamics

Jorge Angeles [4] introduced transformation matrix for rigid body linear translation and angular rotation as for the positions, instant velocity and acceleration.

The inverse kinematics is suitable for parallel manipulators to calculate positions, velocities and accelerations. Such examples are the inverse kinematics analysis of planar 3-DOF 3-RRR parallel mechanism [15] and 2R1T 3-RRS manipulator inverse kinematics and dynamics [90].

There are algebraic method and geometric method to calculate the Jacobian matrix.

The algebraic method usually takes the constant length of a link and develop symbolic equations about the end effector motions for derivatives [14].

The geometric method uses vectors to represent the velocities of the links and develops a relationship between the end effector and the actuators. For a translational and rotational rigid link, the velocity could be simplified where only the velocity along the link needs to be equivalent at the two joints of the links. Such simplification uses dot multiplication with the vector that goes along the two points at the joints on the link [91] [92].

The relationship between the end effector velocity and the actuation velocity is needed to form a Jacobian matrix [4] which could be used for stiffness calculation or other purpose such as degree of freedom verification.

Once the inverse dynamics is conducted with acceleration from the end effector to the actuation, the d'Alembert's principle [93] could be applied which considers acceleration as the force with mass and then by equilibrium formula the reacting forces, moments along with driving requirements will be calculated. An example of such application in 3-PRPR planar robot is found in [94].

The MATLAB Simulink software [95] provides the dynamic simulation for multi-body mechanical systems, where the translational dynamics is simulated based on Newton's equation

and the rotational dynamics is simulated based on Euler's equation. The theoretical values could be verified.

2.6 Trajectory and Interpolation

The motion of the manipulator end effector could be adjusted for optimized performances. There are some examples of such applications, such as the motor reduces driving forces and driving torques with an optimized motion planning [96], the operation time is saved with motion planning [97] and [98].

The motion is adjusted by key points and needs interpolation methods to supply points between two key points. An interpolation by splines is adopted to supply points at time interval for energy optimization [99], another example uses Lagrange interpolation method for energy optimization [100]. The polynomial interpolation is easy to use [101] as it conveniently offers high degree of derivative equation to represent the displacement, velocity and acceleration.

A polynomial interpolation equation is given below, where $s(t_i)$ is a function of displacement about time at t_i. The order of the interpolation equation depends on the number of conditions that need to be met by the planned motion.

$$s(t_i) = m_n t_i{}^n + m_{n-1} t_i{}^{n-1} + \cdots + m_0 \tag{2.6.1}$$

$$s(t_i) = s_i, \dot{s}(t_i) = v_i, \ddot{s}(t_i) = a_i \tag{2.6.2}$$

2.7 Optimization

The performances could be changed when some features or parameters are adjusted. They could be adjusted to tune to the better performance. Such is known as the optimization.

The general aim of optimization is to find a global minimum [102] of an objective (cost function) within the search area. E. K. P. Chong et al [103] introduced classical methods and other more recent methods for optimization. For classical methods are not suitable for highly complex non-linear cost functions, genetic algorithm (GA) is often used for complex cost functions.

Here is the cost function f_j about the input variables $x_1, x_2, \cdots, x_n$.

$$f_j = g_j(x_1, x_2, \cdots, x_n) \tag{2.7.1}$$

The theory of genetic algorithm works as keeping only a group of best samples and mutating them for next generation of competition [103]. The input variables are the adjustable features in a design or a motion planning while the output is the cost function. Redundancy offers the room for adjustment without affecting the overall degree of freedom of the manipulators.

In some situations, it is not only one cost function that needs to be optimized. Some multiple objectives are sought together. The best result is not one single solution in these situations but are a group of solutions that seek the best of an objective without sacrificing the other objectives. The multi-objective optimization keeps a pareto front and updates the front in each generation [104]. In an example of two objective optimization, there are two cost functions, probably conflicting. The two-objective optimal results are a group of results where either objective couldn't be further optimized without compromising the other objective. In this way, the two objectives are both at their best fitness without sacrificing the other. Similarly, when more objectives are involved, the

optimization would yield a group of optimal results where each result represents the best of all objectives before sacrificing any of the objective.

The aims in a design are usually multiple and conflicting. Multi-objective optimization yields a group of optimal results. The results are considered as equally good if there is no preference on selection of privileged objective. One needs to select from the optimal results for a solution with most suitable combination of all objectives.

2.8 Chapter Conclusion

This chapter reviews the theories and general process in manipulator design from a design task to a design solution/analysis and finally the opportunity for optimization. According to this process, it navigates and introduces the knowledge in robotic structural design, modification, kinematic and dynamic analysis, motion planning and finally optimization.

Chapter 3 Research Motivation and Methods

3.1 Research Motivations

Some common planar parallel manipulators such as (2-RR)R, and some common 2R1T spatial parallel structures, such as 3-RRS, 3-PRS, 3-RPS, are widely employed in many industries. However, there is room for improvement in their performances. These common structures need to be modified, re-designed or combined to achieve better performance.

Novel structures are needed for special operation requirements. The designs need to be verified for actual degrees of freedom and modified to come up with various DOF manipulators of similar structure.

The improvement in dynamically balanced mechanisms and design of deployable manipulator are sought, where link-interference need to be avoided and checked.

3.1.1 Dynamic Balancing

The moving centres of mass generate shaking forces and moment which could cause vibration and noise. The dynamic balancing of robots is to improve the unbalanced conditions of robots and to eliminate the shaking forces and moments during motion [25].

Dan Zhang and Bin Wei [105] [106] [107] [108] classified the balancing methods in two types. They are 1) balancing before synthesis and 2) balancing after synthesis. Many designs and methods

are reviewed under the two types of balancing strategies. The main difference is the priority between balancing and functional requirements.

1) Balancing before synthesis is reviewed in paper [109]. This method, by definition, deals with balancing first and then composes a structure with balanced sub-mechanisms. The design examples are: a planar four bar mechanism [110] and a design of 6-DOF mechanism with three legs each is a balanced 3-DOF balanced mechanism [111]. The adjustment of design may be difficult.

2) Balancing after synthesis is more straightforward. This method, by definition, deals with design to satisfy the needs of functions and then adds balancing parts. An example is the planar 2-DOF manipulator which is designed for its function first and then it is added with counterweights for balancing [86] [112]. The adjustment of design is easier.

The balancing could be achieved by passive and active means.

Passive means include adding counter inertia [86] [112], reconfiguration that converts part of the functioning body to balancing mass [105], or sometimes optimal adjustment that is not seeking a complete balancing but reduced shaking forces and moments [113] [114] [84].

Active means include motion planning and driven balancers. Some designs are aimed at producing counter forces and counter moments under control to cancel out the shaking forces and shaking moments, such as a 3-DOF planar balancer [115] and a 6-DOF full balancer [116] designed to be attached to unbalanced sources.

Some designs integrate the passive and active balancing means together. A planar 3-RRR manipulator has counterweights attached to the legs so that the centre of mass is stationary while the shaking moment is balanced by an actively driving flywheel [117]. A group of 1-DOF, 2-DOF

and 3-DOF planar mechanisms are designed with passive counterweight force balancing and active rotation for moment balancing [118].

One needs to consider the nature and property of different balancing means.

The passive balancing needs to attach counter mass on each leg. However, high-DOF parallel manipulator has multiple legs so that the counter mass may require more installation space which could leads to interference and smaller workspace. Furthermore, the passive balancing assumes that the load is constant during operation. Tasks such as pick-and-place could not be completely balanced by passive balancing. The passively balanced multiple legs for higher degrees of freedom may have higher collision or interference chances, thus may need to be avoided. Instead, the combination of two balanced low degrees of freedom mechanisms could be a replacement. And unnecessary weight on legs or on platform should be avoided in passive balancing design, because this will multiply the counter mass weight on legs and takes more energy. For this reason, serial type hybridizing should be avoided since the weight on platform is largely increased although the workspace is large. The passive means is mainly applied in force balancing.

Active balancing increases the control difficulties because the real-time calculation of shaking loads is difficult. Besides, there will be local deformation or local unbalance between the shaking loads source and balancing loads. For this reason, active balancers need to be located where they could isolate the shaking source from the working table. (see figure 3.1.1)
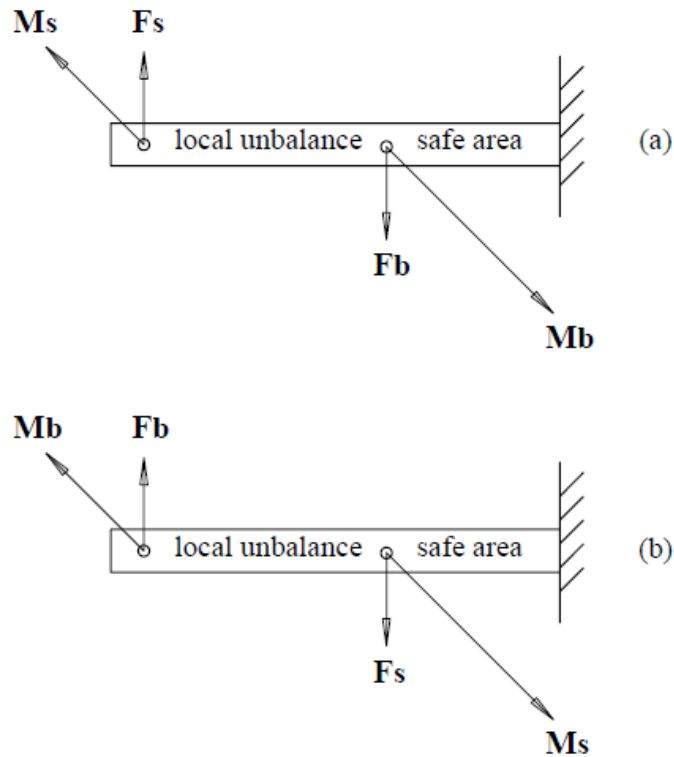
Figure 3.1.1 The shaking loads and balancing loads on a frame.

According to the above analysis, passive and active balancing means are recommended to be integrated for better balancing effects, such as passive force balancing and active moment balancing for manipulators with revolute joints. The shaking forces are passively balanced at the revolute joints while the sensing and real-time calculation of shaking moments at the driven joints are relatively easy as for the active moment balancer. Link interference and energy consumption need more research as additional balancing components are required for dynamic balancing. Motion planning should be considered when allowed. For balanced operation in higher mobilities, the combination of two lower degrees of freedom mechanism could be considered.

3.1.2 Deployable Structures

The challenging outdoor weathers such as storms could damage the structure especially when the structure has a large face that takes the wind loads. The storms are frequent in tropical regions [119]. In North America, solar panels destroyed by storms are heard in news or website [120] [121]. Besides the weather, the indoor compact manufacturing space may also require the structure to be folded to give way to other machines or workpieces that pass by.

The design that could be folded are known as deployable structures. The recent research shows the design of 1-DOF deployable platform which is used for lifting [122]. And another research shows the design of multi-DOF configurable platform with deployable feature [22]. In both cases, the limbs are in fixed vertical planes, perpendicular to the base.

There are some structures that have the potential to be modified as deployable parallel robots, but the development for deployable feature is not discussed in these designs yet. A serial arm is connected to the platform of a parallel manipulator whose limbs are in fixed vertical planes [56], so that the lower parallel stage could be folded. The 2T1R family of three-limb HALF [123] and HANA parallel robots [124] have the limbs in three fixed vertical planes. The 6-DOF 3-RUPU parallel manipulator [125] which has limb in mobile vertical planes. The sealion robots [60] are designed with 4-DOF, 5-DOF and 6-DOF which have the limbs in mobile vertical planes. In three leg robots with more than three degrees of freedom, the limb has at least two actuators. When the actuators are arranged in series, one actuator will take the weight of the other actuator. However, when legs are increased, there may be a small workspace or interference problem. The RHHR [67] is a design with two parallel actuations in each limb for a 6-DOF 3-leg parallel robot. This kind of

integrated joint is newly developed of which more data on its performance might be published in the future.

The research for multi-DOF non-configurable platform deployable parallel structure is rare. Some common designs of parallel manipulators, such as those from the 3-DOF 2R1T family, have non-configurable platform. They need to be re-designed for the deployable feature in applications where this feature is needed.

While 2R1T parallel manipulators are re-designed for deployable feature, the design method could be expanded to design higher-DOF deployable parallel manipulators. Using the modified G-K formula to make a disseminated G-K formula and applying the motion sets intersection for parallel structure, one could choose the end effector motions for the design through the main limb. Finally, the degrees of freedom need to be verified with Jacobian matrix for its rank. This doesn't increase development process as Jacobian matrix is needed also for stiffness calculation.

3.1.3 Link Interference

The parallel manipulators have several limbs. They have chances of colliding with each other (internal interference) or colliding with external objects (external interference). The interferences need to be avoided. This dissertation will analyze the link interference (internal interference). It is significant to reduce the chances of the link to link interferences as this affects the volume of workspace [126] [127] [128]. The pose should be interference free when evaluating or optimizing the workspace.

When links are modeled as line-segments, one needs to calculate the shortest distance between two line-segments. The distance between two line-segments in a certain degree of space is given

in [129], where the relative orientations and arrangements of the two line-segments need to be discussed and sorted in some cases for further discussion. However, the links are not line-segments, because they have width and thickness. Some researches have modeled the links as cylinders with a radius [130] [127] [131], and the distance calculation depends the relative orientations and arrangements of the two cylinders. The algorithms are based on discussion in categories.

Besides the interference detection algorithms, some design methods can avoid interference. As is researched in [132], the 3-RRR spherical parallel manipulator design proposes three design tips to avoid interference. And [133] also concludes that multiple layers, link shapes, joint replacements as the methods to avoid interferences.

The methods and relevant design examples are given in the following.

(a) modify link shape on the same layer [133].

(b) put links on difference planes.

(b.1) the planes (layers) are parallel to each other [134].

(b.2) the planes are intersecting.

(b.2.1) the intersecting planes are perpendicular to the moving platform, such as in 6-DOF 3-[(2-RR)SR] [66] or 6-DOF 3-USR [62].

(b.2.2) the intersecting planes are perpendicular to the base, such as in 3-DOF 3-RRS or 6-DOF 3-[(2-RR)UU].

(c) some special joint such as RHHR [67] that contains two non-conflicting motions. This example

is also applicable in (b.2.2). The RU pair of joints [135] is designed to have a larger motion range

and is equivalent to a spherical joint which is usually limited in motion range [136].

When design and its workspace are determined, motion planning is also an option to avoid link to

link interference [137].

Large number of links in three-dimensional space take longer time in interference detection. The

design should avoid link interferences where possible and make detection easier. The design and

detection methods will be discussed on 2R1T manipulators and higher-DOF parallel manipulators.

The high-DOF manipulator could arrange the limbs in different vertical planes or parallel layers

to reduce the changes of interference while making the detection easier.

3.2 Design Methods

Considering the needs for dynamic balancing, deployable feature and interference avoidance, the

parallel robots with limbs in vertical planes satisfy these requirements.

The 2R1T 3-RRS parallel manipulator could offer 2 rotations and 1 translation and ideal for force

balancing with the revolute joints. The moments are balanced by flywheels above the 3-RRS, so

the area under the 3-RRS robot is free from shaking forces and shaking moments. With a

combination to a balanced planar parallel manipulator, they could form a pair of large workspace

balanced manufacturing machine. The planar balanced parallel structure could be 3-RRR or (2-

RR)R, because the revolute joints are ideal for force balancing and they could have an active driven

flywheel for moment balancing. The 3-RRS have limbs in three intersecting fixed vertical planes, which could reduce the chances of limb to limb collision.

The 2R1T 3-RPS or 3-PRS have limbs in three fixed vertical planes which shares the same design feature of those deployable 1-DOF table [122] or a configurable platform parallel manipulator [22]. The 2R1T deployable robots could serve the duty of solar tracking and lie flat for stormy weather protection.

Figure 3.2.1 Higher DOF manipulator with mobile vertical plane on horizontal planar mechanism.

When designing deployable parallel robots of higher degrees of freedom, fixed vertical planes could be replaced with mobile vertical planes on horizontal actuators. The horizontal plane could take parallel actuations to avoid two actuations in serial arrangement in one limb. When a limb has

28

platform plane Po

connecting joint Pi

vertical plane Vi

horizontal plane Ho

Figure 3.2.1 Higher DOF manipulator with mobile vertical plane on horizontal planar mechanism.

When designing deployable parallel robots of higher degrees of freedom, fixed vertical planes could be replaced with mobile vertical planes on horizontal actuators. The horizontal plane could take parallel actuations to avoid two actuations in serial arrangement in one limb. When a limb has

28

two actuators, the design could put all actuation weights on the base. The loads and actuation duty need to be evenly distributed, and the limb needs to be tough in holding weight. Therefore, serial type hybrid manipulator is not considered; for parallel type hybrid manipulators, the two actuators are aligned in parallel on base for each limb.

3.3 Evaluation Methods

The design is going to be evaluated for performances such as workspace volume, stiffness and energy consumption.

The workspace volume is to be evaluated with inverse kinematics by finding the eligible end effector positions. For solar tracking applications with 2R1T manipulators where the translational motion is redundant, minimum platform height algorithm (intersection of possible solutions) is developed that could rapidly search for eligible workspace for 2R1T solar trackers. In high-DOF manipulators, where the horizontal actuations are arranged in parallel layers, only eligible pose without interference could be counted to evaluate workspace. The boundary offset method is developed for same layer interference scan.

General stiffness summation is taken as an overall evaluation index for stiffness in multiple directions [14]. Modified Jacobian matrix $\boldsymbol{J_e}$ is derived from classical Jacobian matrix $\boldsymbol{J_o}$ for stiffness evaluation in directions other than the global coordinate axes.

$$\boldsymbol{K_o} = \boldsymbol{J_o}^T \boldsymbol{K_q} \boldsymbol{J_o} \, , \ \boldsymbol{J_o}\dot{\boldsymbol{x}}_o = \dot{\boldsymbol{q}} \tag{3.3.1}$$

$$\boldsymbol{K_e} = \boldsymbol{J_e}^T \boldsymbol{K_q} \boldsymbol{J_e}, \ \boldsymbol{J_e}\dot{\boldsymbol{x}}_e = \dot{\boldsymbol{q}} \tag{3.3.2}$$

Energy index is taken to evaluate the energy consumption where many articles are taking actuation force squared or torque squared as the index of energy consumption [138] [139] [140].

3.4 Applications and Optimizations

The following chapters will present the designs and analysis of adaptive (2-RR)R or (2-RR)R balanced robot and 3-RRS balanced robot where the dynamic balancing and optimal energy consumption problem will be discussed through structural adaptive features and motion planning. Furthermore, the two balanced manipulators are combined for higher DOF balanced operations. The adaptive 3-PRS and 3-RPS robots from the 2R1T family are re-designed for applications as deployable solar trackers and multiple objectives are optimized. The deployable design has been expanded to higher degree of freedom, where hybrid parallel manipulator with limbs in mobile vertical planes on horizontal actuations are discussed and the designs are optimized for multiple objectives.

The design objectives can be larger workspaces with given platform orientations, minimum sizes and minimum lie-flat height, while operational objective can be minimum energy consumption, and higher stiffness dependant on what are demanded in a certain task which may be different from task to task. The design objectives usually take structural sizes as inputs to the optimization problem, while the operation objectives usually take adaptive variables as inputs to the optimization problem. Therefore, the optimizations in many cases are practiced in two stage. The first stage is a design optimization to decide design parameters (for example, the geometric sizes of links). Once these sizes are decided, they become fixed sizes. The second stage is an operational optimization that takes advantages of the kinematic redundancy or structural adaptive features of

a design to find an adjustment that is optimal to a certain task. Both design or operational optimizations could be single-objective or multi-objective. But they would be better to be done in two stages. If both design parameters and the adaptive parameters are optimized together, the computation time may be exponentially increased.

3.5 Chapter Conclusion

The motivation is to design various DOF dynamically balanced or deployable parallel manipulators with less link interference. Structures with limbs in vertical planes satisfy the requirements. This includes arranging the parallel limbs in fixed vertical planes (3-DOF 2R1T manipulators) or mobile vertical planes with parallel actuations on horizontal plane (higher DOF manipulators). The horizontal planes could be arranged in layers to avoid interference.

Minimum platform height algorithm, link boundary offset, modified Jacobian matrix, and torque squared are the methods that evaluate the performances of the design. When the performances have room for further improvement, the structure could be adapted, or best design parameters could be found through single or multi objective optimization.

The applications are manufacturing and energy harvesting. The designs will be demonstrated in the following chapters.

Chapter 4 Dynamic Balancing for Various DOF Motions

4.1 Chapter Introduction

The moving inertia of unbalanced machine brings about shaking forces and shaking moments which could cause vibration and noise. Finally, it affects the precision of manufacturing. Dynamic balancing is demanded to provide a solution.

This chapter discusses the dynamic balancing of common parallel manipulators by passive force balancing and active moment balancing, because the motor torques are easier to be actively sensed and balanced. Due to the additional balancing components, it has possibility of link interference and takes more energy to drive the system. The configuration change is suggested in the design for interference avoidance. Structural adaption and motion planning are discussed for energy consumption minimization.

A first example of an adaptive planar 2-DOF (2-$\underline{R}$R)R parallel mechanism is demonstrated, where the effect of adaption alone is examined for minimizing the driving energy. This machine can be modified to be a 3-DOF (2-$\underline{R}$R)$\underline{R}$ balanced planar mechanism by serial type hybridizing.

A second example is an adaptive 2R1T 3-DOF 3-$\underline{R}$RS parallel mechanism. The effect to minimize driving energy is compared between structure adaption alone and structure adaption with motion planning. The theoretic dynamic model is verified by Simulink software.

Finally, the combination of the two machines, (2-$\underline{R}$R)$\underline{R}$ and 3-$\underline{R}$RS, for a dynamically balanced 6-DOF manufacturing machine is discussed.

4.2 Theories and Methodologies

For (2-RR)R and 3-RRS robots, the mass and counter mass are passively balanced about the revolute joints, while the moments are actively balanced by flywheels.

The configuration needs to be changed to avoid link interference. The middle joint angle needs to be reversed to avoid the counter weight collision. In figure 4.2.1 and figure 4.2.2, the middle joint angles of (2-RR)R and 3-RRS are reversed in sub-figure (b) as compared to the original design in sub-figure (a).

D'Alembert's principle is used to calculate the forces and moments on dynamic models at fine steps of the planned trajectory. Structural adaption and motion planning are applied for optimal energy consumption.

(a)   (b)
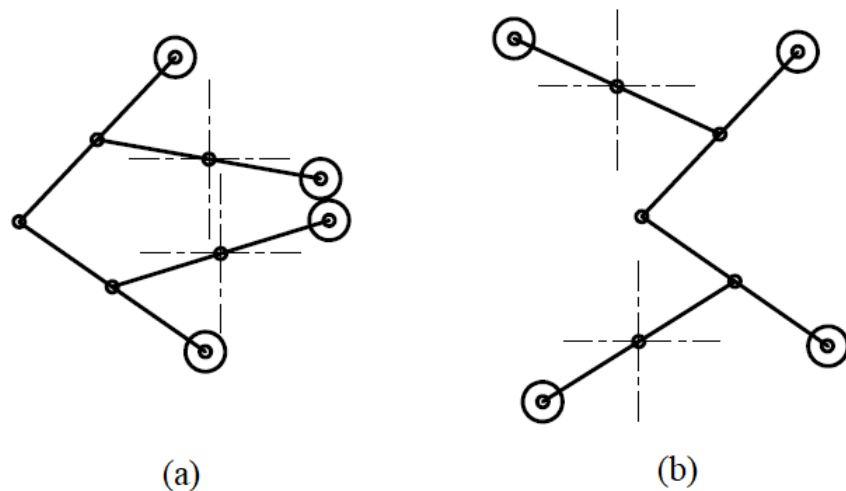
Figure 4.2.1 Planar (2-RR)R design. (a) convex; (b) concave.
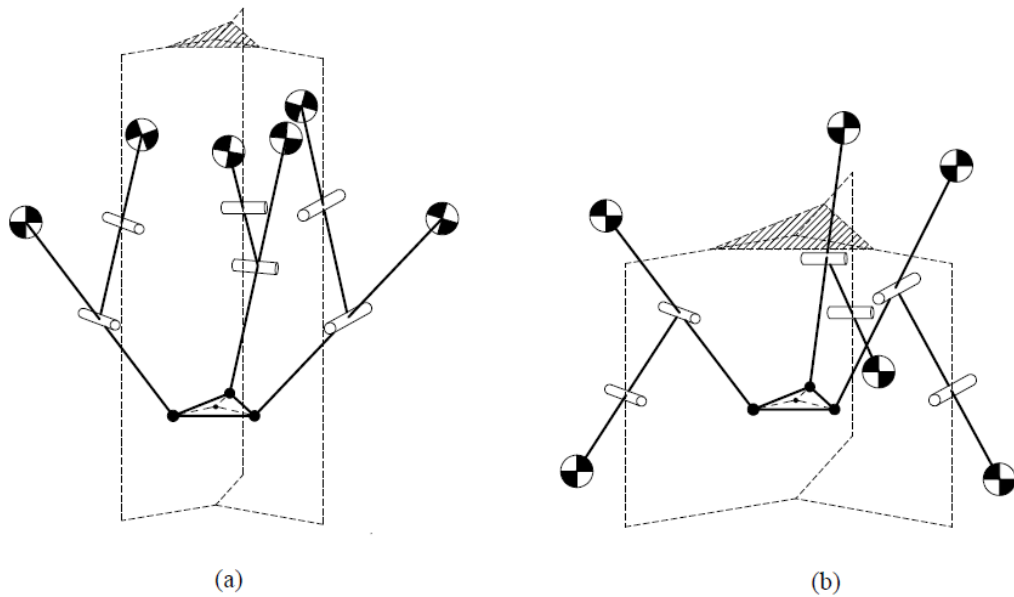
Figure 4.2.2 Spatial 3-RRS design. (a) convex; (b) concave.

4.3 Planar Dynamic Balancing

This section presents a dynamically balanced planar parallel manipulator, (2-RR)R robot, with structurally adaptive design which can be adjusted to minimize the overall energy consumption required to complete a defined cyclic motion of the end effector. The genetic algorithm is adopted to search for optimal adaption that results to minimum energy consumption. The (2-RR)R robot discussed in this section has shaking forces passively balanced by counter masses, and the shaking moments actively balanced by a flywheel. A balanced mechanism eliminates noise and vibration however may require additional driving energy due to its additional balancing components. As for a defined motion that ought to be repeated in cycles, adaption could be an energy saving strategy when alternating the motion is not applicable.

4.3.1 Planar (2-RR)R Mechanism Design

The (2-RR)R planar mechanism is designed with two degrees of freedom in the X-O-Y plane, that allows the end effector to move in x and y axes independently. It has two articulated legs, which are driven at the base revolute joints as is illustrated in figure 4.3.1.
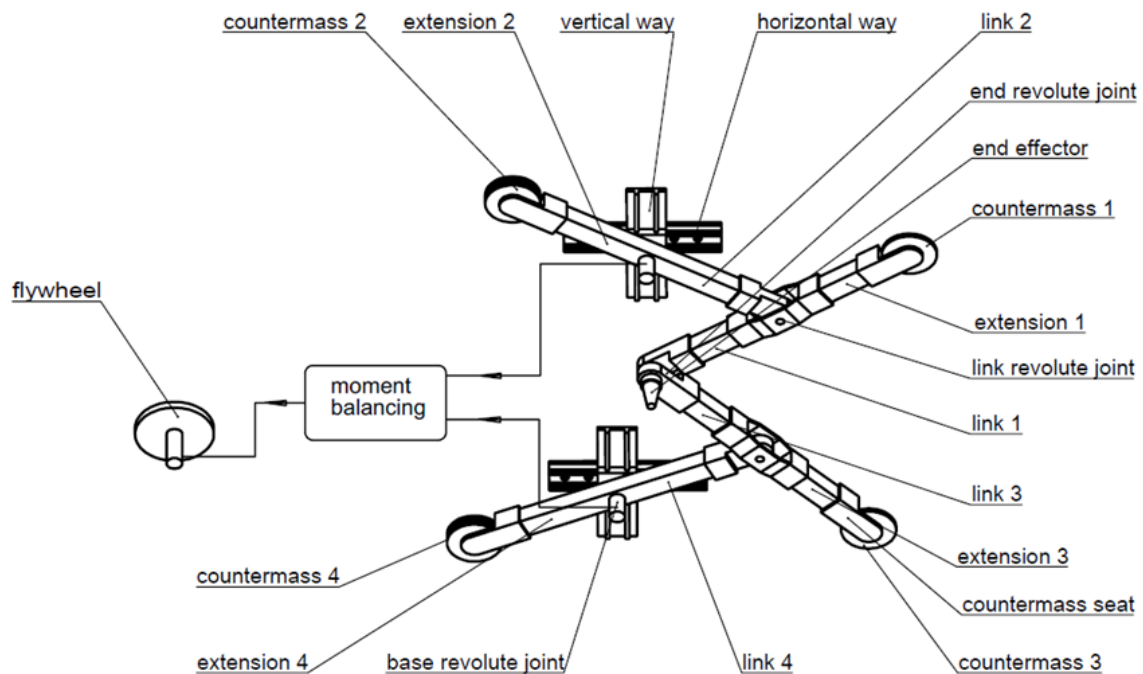
Figure 4.3.1 Mechanical design.

The leg carries counter masses for forces balancing, so that the mass center of each leg is located at the base revolute joints. A flywheel is controlled to actively balance the moment in X-O-Y

plane. Each base revolute joint is mounted on a stage that is able to adjust its position along the horizontal (x axis) and vertical (y axis) ways, which changes dynamic properties. Industrial engineers can reposition the input joints based on the defined motion of the end effector. These stages will be locked from moving once the positions of the base revolute joints are determined. During the end effector motion, the adaption is locked so that the input joints positions are fixed. The structure can be written in full as (2-PPRR)R.

4.3.2 Inverse Kinematics and Dynamics

The (2-RR)R robot is a rigid parallel robot thus the inverse kinematics method is practiced to calculate the mechanism pose from a given end effector position (figure 4.3.2 (a)). The rigidity applies to the velocity and acceleration calculations (figure 4.3.2 (b)).

The input revolute joints are at B_1 and B_2, and the end effector at position P. The positions are represented by vectors from coordinate origin O. There are two identical legs, where $i = 1 \, or \, 2$ represents the index of leg.

$$OB_i = [x_{bi} \quad y_{bi} \quad 0]^T, \; OP = [x_p \quad y_p \quad 0]^T \tag{4.3.1}$$

With these vectors, the angular displacements of the input joints are calculated.

$$\theta_i = tan^{-1}\left(\frac{y_p - y_{bi}}{x_p - x_{bi}}\right) + [-1]^i \cos^{-1}\left(\frac{|B_i P|^2 + l_2^2 - l_1^2}{2 \cdot |B_i P| l_2}\right) \tag{4,3.2.a}$$

Where,

$$|A_i P| = |A_i D_i| = l_1 \text{ and } |A_i B_i| = |B_i C_i| = l_2 \tag{4.3.2.b}$$

The positions of revolute joints A_1 and A_2 are given below.

36

$$OA_i = OB_i + l_2[\cos\theta_i \quad \sin\theta_i \quad 0]^T \qquad (4.3.3)$$
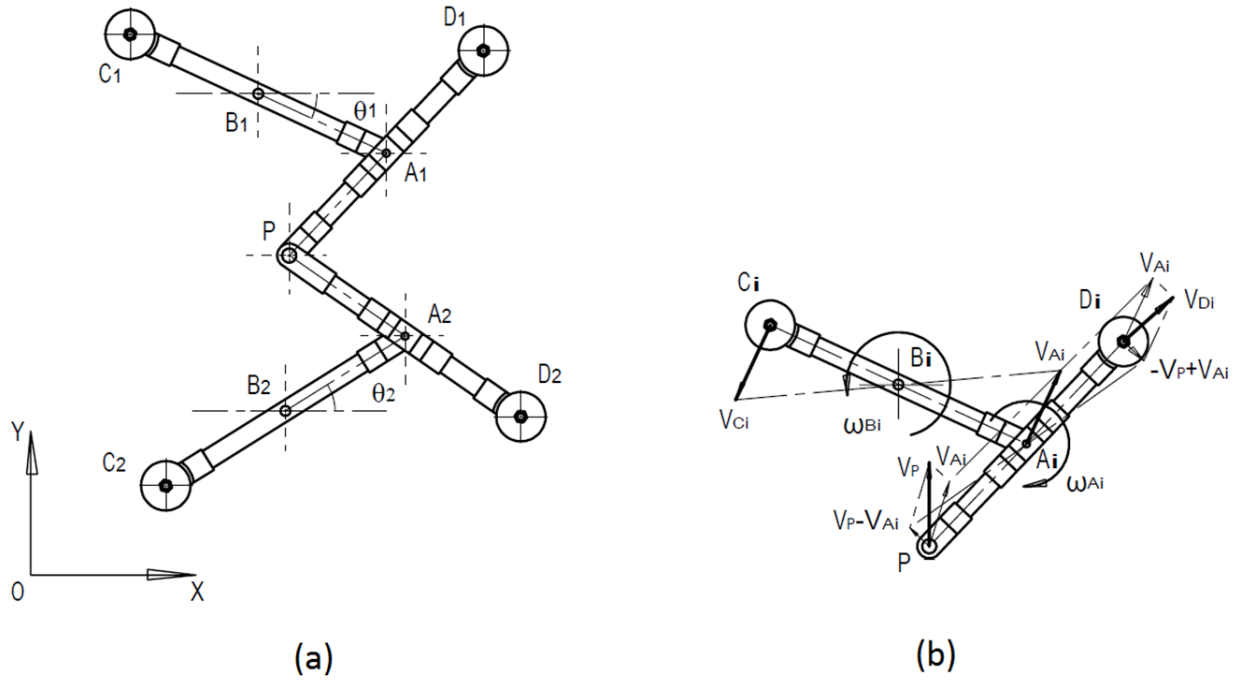
Figure 4.3.2 Kinematic analysis.

The values of the angular displacements need to be judged to determine if the given end effector position P is reachable. Only eligible pose is considered for further analysis.

The velocity relationship between the end effector and the input joints are given.

$$\omega_{Bi} \times B_iA_i + \omega_{Ai} \times A_iP = v_p \qquad (4.3.4.a)$$

Since the end effector has two degrees of freedom, its velocity has components along x axis and y axis. The angular velocities of the two links on each leg are obtained.

$$\omega_{Bi} = [0 \quad 0 \quad \dot{\theta}_i]^T, \omega_{Ai} = [0 \quad 0 \quad \dot{\theta}_{ai}]^T \qquad (4.3.4.b)$$

The angular velocities of the links are needed in acceleration analysis.

The angular acceleration of the links can be calculated through the end effector acceleration.

$$\boldsymbol{a_{Ai}} = \boldsymbol{\alpha_{Bi}} \times \boldsymbol{B_iA_i} + \boldsymbol{\omega_{Bi}}^2 \boldsymbol{A_iB_i} \qquad (4.3.5.\text{a})$$

$$\boldsymbol{a_{Bi}} = \boldsymbol{0} \qquad (4.3.5.\text{b})$$

$$\boldsymbol{a_{Ci}} = -\boldsymbol{a_{Ai}} \qquad (4.3.5.\text{c})$$

The acceleration of point $\boldsymbol{P}$ is $\boldsymbol{a_p}$.

$$\boldsymbol{a_p} = \boldsymbol{a_{Ai}} + \boldsymbol{\alpha_{Ai}} \times \boldsymbol{A_iP} + \boldsymbol{\omega_{Ai}}^2 \boldsymbol{PA_i} \qquad (4.3.5.\text{d})$$

$$\boldsymbol{a_{Di}} = 2\boldsymbol{a_{Ai}} - \boldsymbol{a_p} \qquad (4.3.5.\text{e})$$

Since the end effector has two degrees of freedom, its acceleration $\boldsymbol{a_p}$ has components along x axis and y axis. The angular accelerations of the two links on each leg are obtained.

$$\boldsymbol{\alpha_{Bi}} = [0 \quad 0 \quad \ddot{\theta}_i]^T, \boldsymbol{\alpha_{Ai}} = [0 \quad 0 \quad \ddot{\theta}_{ai}]^T \qquad (4.3.5.\text{b})$$

The inertias need to be given to determine loads and actuation forces.

Counter mass 1, m_{d1}, is at point $\boldsymbol{D_1}$; counter mass 2, m_{c1}, is at $\boldsymbol{C_1}$; counter mass 3, m_{d2}, is at point $\boldsymbol{D_2}$; counter mass 4, m_{c2}, is at $\boldsymbol{C_2}$; and the end effector mass, m_p, is at point $\boldsymbol{P}$. These are modeled as concentrated masses.

The four rotating bodies of the (2-R̲R)R robot are aligned with vectors $\boldsymbol{D_1P}$, $\boldsymbol{D_2P}$, $\boldsymbol{A_1C_1}$ and $\boldsymbol{A_2C_2}$, have masses noted as m_{a1}, m_{a2}, m_{b1}, and m_{b2} respectively, excluding the counter masses and the end effector mounted on them. These masses are modeled as evenly distributed along the vectors with the center of mass at the rotating axis of the bar.

For the links D_iP, since $|A_iD_i| = |A_iP|$, if $m_{di} = \frac{1}{2}m_p$, the centripetal forces and the tangential

forces are cancelled. For the links C_iA_i, since $|B_iA_i| = |B_iC_i|$, if $m_{ci} = \frac{1}{2}m_p + m_{di} + m_{ai}$, the

centripetal forces and the tangential forces are cancelled. The whole (2-<u>RR</u>)R robot is completely

force balanced.

Rotational inertia of links PD_i about revolute joint A_i with all masses loaded on it is denoted as I_{ai}.

$$I_{ai} = \frac{1}{12}m_{ai}(2l_1)^2 + m_{di}l_1^2 + \frac{1}{2}m_pl_1^2 \tag{4.3.6.a}$$

Rotational inertia of links C_iA_i about revolute joint B_i with all masses loaded on it is denoted

as I_{bi}.

$$I_{bi} = \frac{1}{12}m_{bi}(2l_2)^2 + 2m_{ci}l_2^2 \tag{4.3.6.b}$$

At the revolute joint of end effector P, the two legs are connected. A force F_p acts on link $|A_1P|$,

its reaction force $-F_p$ acts on link $|A_2P|$. The mutual forces form the moments around joint A_1

and A_2 which cause the angular accelerations.

One could consider adding a rotation to the 2-DOF motion by adding a rotary motor that exerts a

moment M_p around z axis on link $|A_1P|$. The output torque of this motor is $T_p = -M_p$. This

makes it a 3-DOF planar hybrid mechanism. If there is no extra motor added, then $M_p = 0$.

$$A_1P \times F_p + M_p = I_{a1}\alpha_{A1}, \tag{4.3.7.a}$$

$$A_2P \times (-F_p) = I_{a2}\alpha_{A2} \tag{4.3.7.b}$$

The forces F_{A1} and F_{A2} act on links $|A_1P|$ and $|A_2P|$ respectively.

$$F_p + F_{A1} - m_{a1}a_{A1} - m_{d1}a_{D1} - \frac{1}{2}m_pa_p = 0 \tag{4.3.7.c}$$

$$-F_p + F_{A2} - m_{a2}a_{A2} - m_{d2}a_{D2} - \frac{1}{2}m_p a_p = 0 \qquad (4.3.7.d)$$

The forces F_{Bi} act on links $|B_i A_i|$ from the base joint B_i.

$$F_{Bi} - F_{Ai} - m_{ci}a_{C1} = 0 \qquad (4.3.7.e)$$

As the forces are balanced for both legs, only moments are remained to be balanced. The driving torques around the input joints B_1 and B_2 are given as below.

$$T_i = B_i A_i \times F_{Ai} + I_{bi}\alpha_{Bi} \qquad (4.3.8.a)$$

The third torque T_3 is controlled to balance the overall moment on the base.

$$T_1 + T_2 + T_3 = 0 \qquad (4.3.8.b)$$

The energy consumption of direct current electric motor consists the mechanical energy and the heat loss [141]. For each of the three motors in the balanced (2-RR)R robot, the supplied power is formed by two parts as described in the equation below.

$$U_i I_i = E_i I_i + I_i^2 R , \quad \text{i=1, 2 or 3} \qquad (4.3.9.a)$$

The back electromagnetic force is proportional to the rotating speed of the input joints, where K_e is a constant parameter of the motor.

$$E_i = K_e \omega_i , \quad \text{i=1, 2 or 3} \qquad (4.3.9.b)$$

The current is proportional to the torque exerted around the input joints, where K_t is a constant parameter of the motor.

$$I_i = K_t(z \cdot T_i) , \quad \text{i=1, 2 or 3} \qquad (4.3.9.c)$$

The mechanical energy consumption is from the back electromagnetic force and the current.

$$E_i I_i = K_e K_t \omega_i (\mathbf{z} \cdot \mathbf{T_i}) \tag{4.3.9.d}$$

The rest of the energy consumption is the heat loss which is proportional to the current squared. As the current is proportional to torque, the heat loss is proportional to the torque squared.

$$I_i^2 R = K_t^2 R \mathbf{T_i}^2 \tag{4.3.9.e}$$

The acceleration of the input joints consumes electric energy while the braking by reversing plugs generates electric energy [142], which is reflected in the back electromagnetic force. The (2-$\underline{RR}$)R robot is accelerating and braking during the cycle of motion. If the friction is not considered during the motion, the energy consumption is the total heat loss on the resistances of the motors, which is proportional to current squared. Current squared, or torque squared, has been considered as the rate of energy consumption based on algorithm in [138] [139] [140]. The integration of the rate over time is the total energy consumption of the robot.

Torques $\mathbf{T_1}$ and $\mathbf{T_2}$ act at joints $\mathbf{B}_1$ and $\mathbf{B}_2$; $\mathbf{T_3}$ acts on the flywheel for moment balancing. Power P_i is proportional to torque $\mathbf{T_i}$ squared.

$$P_i = I_i^2 R \propto \mathbf{T_i}^2 R \tag{4.3.9.f}$$

4.3.3 Operation Optimization of Energy Consumption Index

Since the dynamic properties change as the positions $\mathbf{B_1}$ and $\mathbf{B_2}$ are relocated, a single-objective optimization is run for optimal $\mathbf{B_1}$ and $\mathbf{B_2}$ positions that lead to least energy consumption for a prescribed motion.

With the design parameters given in table 4.3.1, the dynamic simulation can be performed in MATLAB.

Table 4.3.1 The (2-<u>RR</u>)R robot design parameters.

Symbols	Units	Values
m_p	kg	0.2
m_{di}	kg	0.1
m_{ci}	kg	0.3
m_{ai}	kg	0.1
m_{bi}	kg	0.1
l_1	m	0.2
l_2	m	0.2

The end effector travels in cycles along a close-loop trajectory that is L in length. Each cycle takes period time T to travel. T is evenly divided to n pieces of steps, each with an index number j. The magnitude of velocity $|v_p|$ is constant. At each step marked by j, the kinematic and dynamic index are calculated with respect to time.

Table 4.3.2 Trajectory parameters.

Parameters	Values
L	$0.36\ m$
T	$3.6\ s$
n	360
$|v_p|$	$0.1\ m/s$
Starting point	$[0.0 \quad 0.1 \quad 0.0]$

Two examples, a triangle and a four-semicircle close-loop trajectories, will be practiced which are required to obey the parameters given in table 4.3.2 for simulation.

The cost function of energy consumption is the summation of power consumption index p_j from all division points during the motion. It is assumed that the torques T_1, T_2 and T_3 have the same electric parameters so that the three torques have same weight in the cost function f.

$$p_j = (T_1{}^2 + T_2{}^2 + T_3{}^2)_j \text{ and } f_j = \sum_{j=1}^{n} p_j \qquad (4.3.10.\text{a})$$

$$f = f_n \qquad (4.3.10.\text{b})$$

Due to the complexity of f, genetic algorithm is a suitable optimization process and is run by MATLAB optimization tool. The positions B_1 and B_2 are allowed to be adapted within the adjustment range of the horizontal and vertical ways, which determines the constraints of the input variables $x(1){\sim}x(4)$ given in table 4.3.3.

Table 4.3.3 Optimization variables.

Parameters	Values and range
OB_1	$[0.0 + x(1) \quad 0.25 + x(2) \quad 0.0]$
OB_2	$[0.0 + x(3) \quad 0.0 + x(4) \quad 0.0]$
$x(1)$	$[-0.03 \quad 0.03]$
$x(2)$	$[-0.03 \quad 0.03]$
$x(3)$	$[-0.03 \quad 0.03]$
$x(4)$	$[-0.03 \quad 0.03]$

Only the simulation result that can finish the n steps are eligible for selection. The least f and its results $x(1){\sim}x(4)$ are tracked as the best fitness and are compared with upcoming results from

trials. This will only be replaced once better fitness is found. The optimization terminates after all generations of candidates are attempted.

Trajectory 1 parameters are given in table 4.3.4. The trajectory is a close-loop triangle. The points K_0, K_1 and K_2 are the three vertices of the triangle. The end effector starts the motion at K_0 then moves to K_1, and then K_2, finally returns to K_0 when a cyclic motion is complete.

Table 4.3.4 Trajectory 1 parameters.

Parameters	Values
OK_0	[0.0 0.10 0.0]
OK_1	[0.9 0.22 0.0]
OK_2	[0.9 0.10 0.0]

The trajectory 1, and the results are plotted in figure 4.3.3. The values of original and optimized results are given in table 4.3.5 for trajectory 1.

Table 4.3.5 Original and optimized results of trajectory 1.

Parameters	Original values	Optimized values
x(1)	0.0	-0.028
x(2)	0.0	0.029
x(3)	0.0	0.03
x(4)	0.0	-0.03
f	0.375	0.12538
Optimization efficiency	1-0.12538/0.375=66.57%	

Trajectory 2 parameters are given in table 4.3.6. The trajectory is a close-loop with four semi-circles. The points O_1, O_2, O_3 and O_4 are the centers of the semi-circles with radius R_1, R_2, R_3 and R_4 respectively. The first semi-circle route is from π to 0 clockwise; the second semi-circle route is from π to 2π counter clockwise; the third semi-circle route is from π to 2π counter clockwise; the fourth semi-circle route is from 2π to π clockwise. The end effector starts from the first semi-circle route, then second semi-circle route, then third semi-circle route, finally the fourth semi-circle route and returns to the starting point of the first semi-circle route.

Table 4.3.6 Trajectory 2 variables.

Parameters	Values
R_1	$0.12/\pi$
R_2	$0.06/\pi$
R_3	$0.15/\pi$
R_4	$0.03/\pi$
OO_1	$[0.12/\pi \quad 0.0 \quad 0.0]$
OO_2	$[0.30/\pi \quad 0.0 \quad 0.0]$
OO_3	$[0.21/\pi \quad 0.0 \quad 0.0]$
OO_4	$[0.03/\pi \quad 0.0 \quad 0.0]$

The trajectory 2, and the results are plotted in figure 4.3.4. The values of original and optimized results are given in table 4.3.7 for trajectory 2.

Table 4.3.7 Original and optimized results of trajectory 2.

Parameters	Original values	Optimized values
x(1)	0.0	0.029
x(2)	0.0	0.03
x(3)	0.0	0.022
x(4)	0.0	-0.029
f	8.8623	5.5890
Optimization efficiency	1-5.5890/8.8623=36.94%	

For trajectory 1, joint relocation is able to save 66.57% of energy within constraints. For trajectory 2, joint relocation is able to save 36.94% of energy. If both trajectories are to be repeated in large number of cycles as in production line operations, the saving in energy is remarkable.

Figure 4.3.3 First demonstration. (a) trajectory 1; (b) genetic algorithm optimization; (c) driving torques original; (d) driving torques optimized; (e) power consumption index p_j over time; (f) energy consumption index f_j over time.
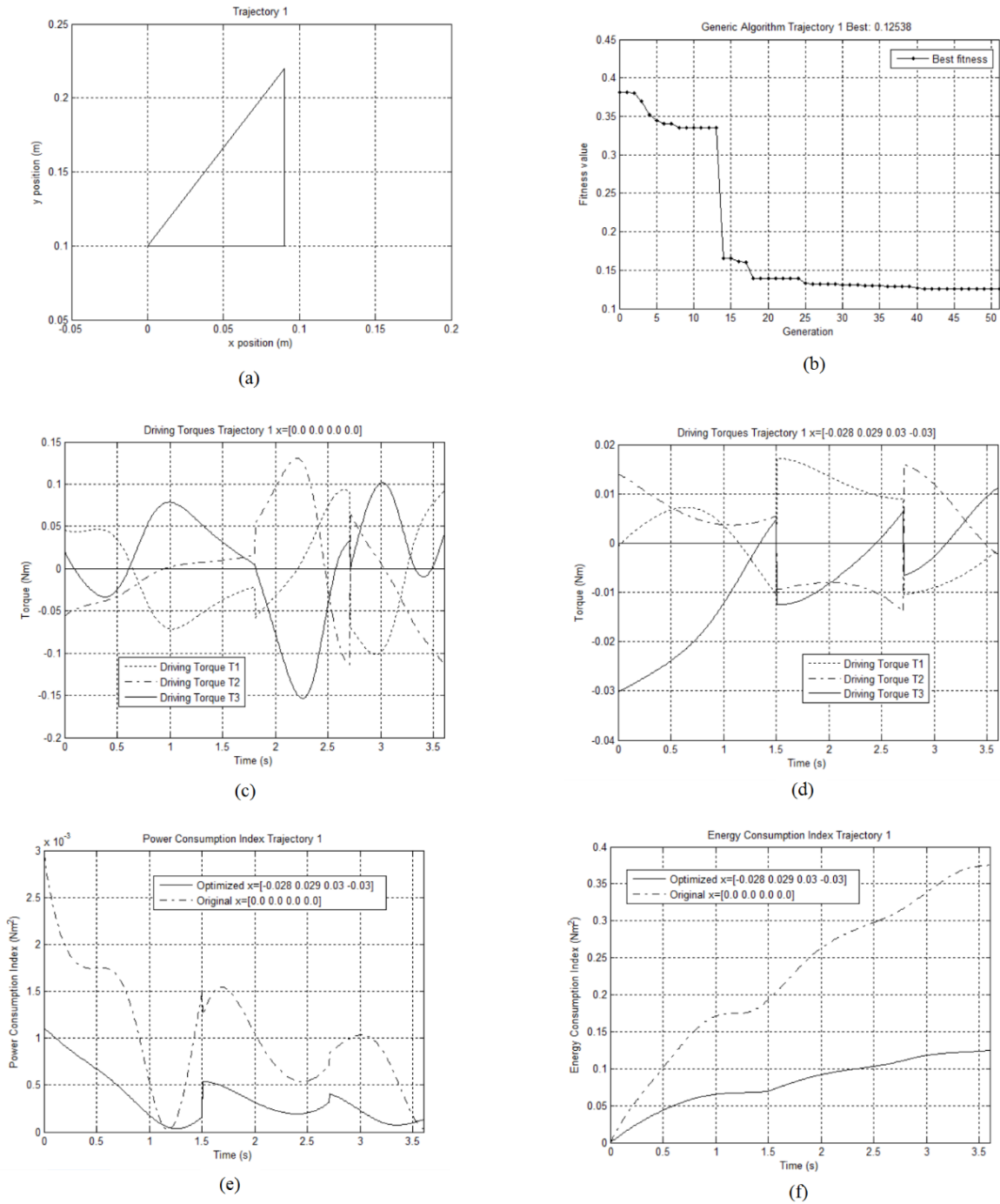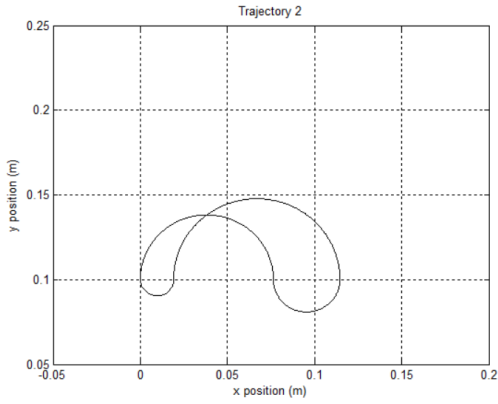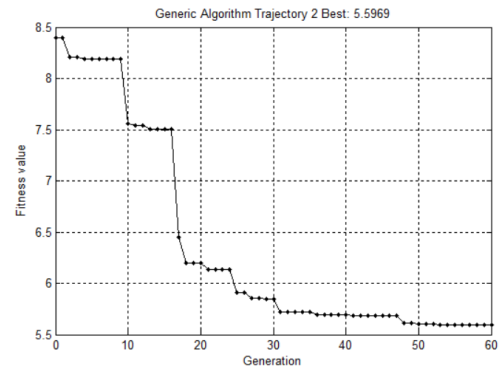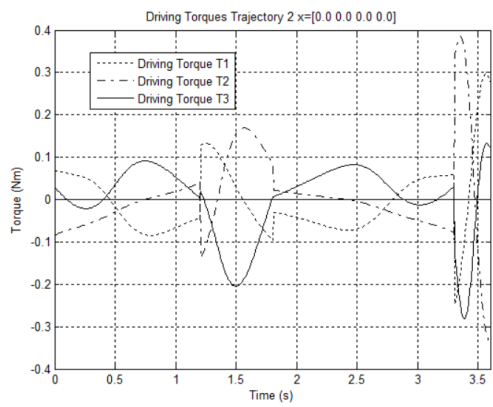
Figure 4.3.4 Second demonstration. (a) trajectory 2; (b) genetic algorithm optimization; (c) driving torques original; (d) driving torques optimized; (e) power consumption index p_j over time; (f) energy consumption index f_j over time.
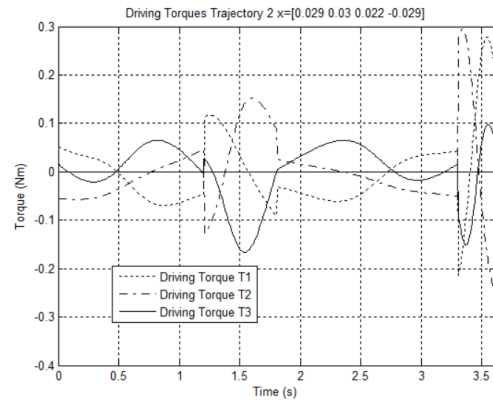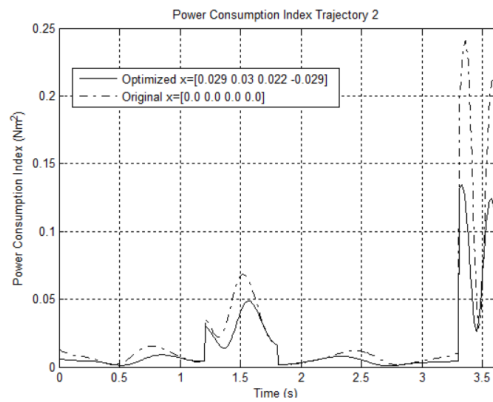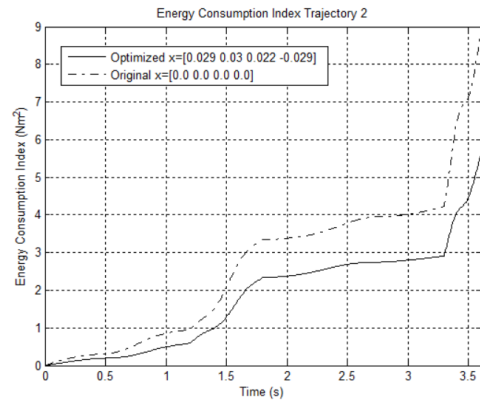
48

4.3.4 Re-design to be (2-<u>RR</u>)<u>R</u> for Planar 3-DOF Operation

At the end effector, a driven rotation could be added to make it a 3-DOF planar hybrid manipulator. The balancing weight and balancing moment are to be adjusted accordingly.

4.3.5 Section Conclusion

The dynamically balanced (2-<u>RR</u>)R robot is free from vibration and noise problems, however it has additional mass and balancing components which cause the machine to be more energy-consuming. Through repositioning its input joints on the base, the energy consumption can be minimized without the need to change the motion of end effector. Two trajectory examples with defined motion have been conducted and the optimization efficiency is obvious. The optimization effect is dependent on trajectories. This method may effectively save energy for robots that repeat a given cyclic motion and it is easy to adopt. Its applications may be developed in automated manufacturing plants that largely rely on robots, as to promote an energy saving and environmental friendly production. This mechanism could be re-designed by adding an actuator at the end effector to make a 3-DOF (2-<u>RR</u>)<u>R</u> planar mechanism.

4.4 Spatial P*U* Dynamic Balancing

This section discusses the adaptive relocation of a manipulator joints and motion planning as methods to reduce energy consumption in robotic manipulators. A 3-<u>RR</u>S dynamically balanced parallel manipulator is designed for manufacturing operations and on which numerical simulations

is practiced for demonstration. The dynamically balanced manipulator contains additional balancing components and requires additional energy in actuation which makes energy problem significant. It promotes environment-friendly green operations of manipulators in energy saving through optimization of adaptive joint locations in supplement to motion planning, meanwhile it eliminates vibration and noise problems by dynamic balancing.

4.4.1 A 3-RRS Mechanism Design

In figure 4.4.1, the 3-RRS is composed of three identical sets of arms that hold the platform and move it in 3D space. Each arm is actuated by the motor which is seated in the motor box. Each arm has two links which are the up arm and the fore arm. The up arm is driven by the rotary motor. The fore arm is a follower which is connected to the up arm with a revolute joint and is connected to the platform with a spherical joint. Counter masses are attached to arms on their extension parts to locate centers of gravity at revolute joints to achieve passive force balancing. The total moment needs to be actively balanced by flywheels which are actuated by two motors on the roof top in two orthogonally aligned axes. The height of each motor box is adjustable and self-locking by the vertical lead screw. The structure can be written in full as 3-PRRS.
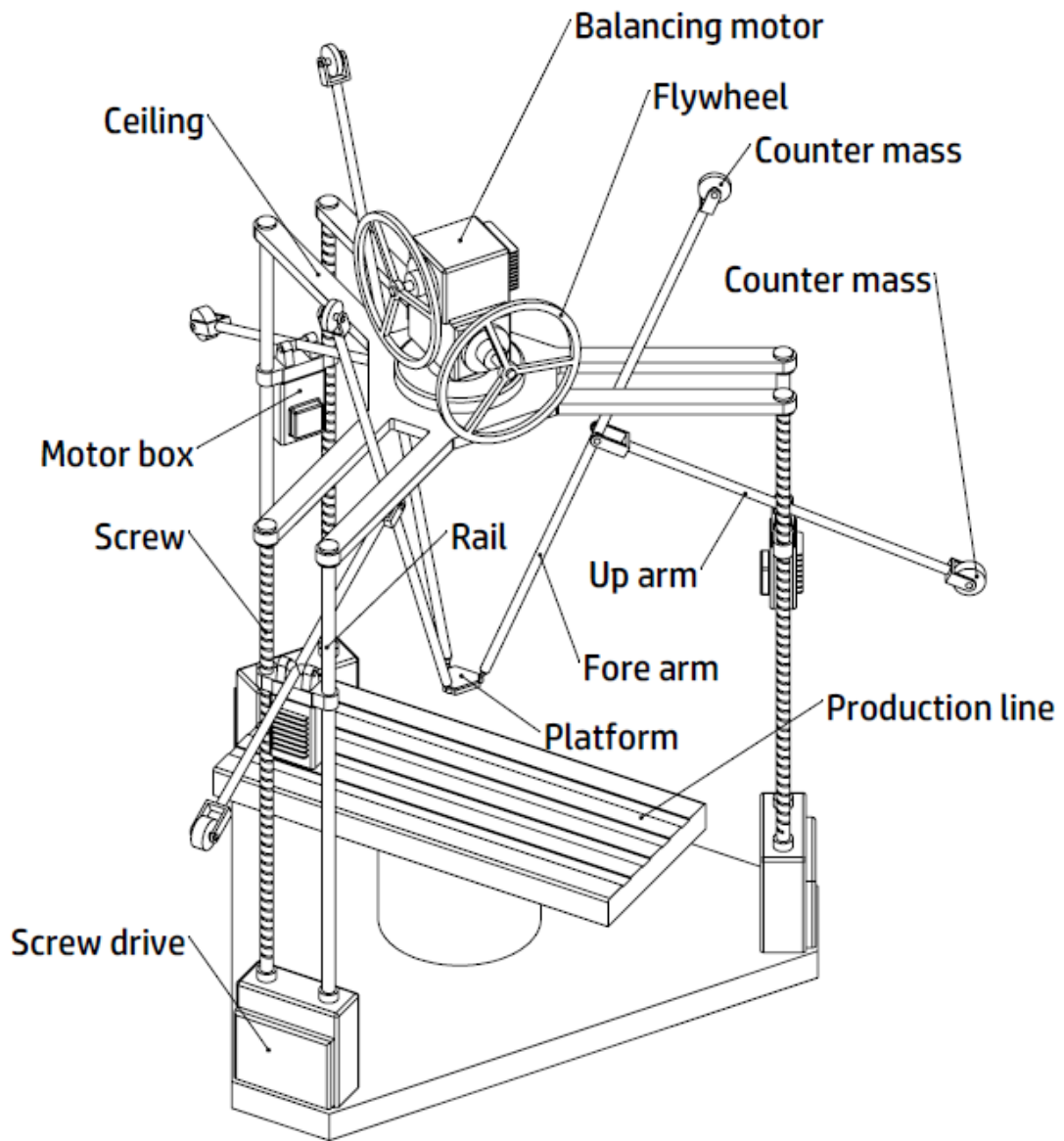
Figure 4.4.1 3-RRS robot design.

Figure 4.4.2 3-RRS robot modelling.

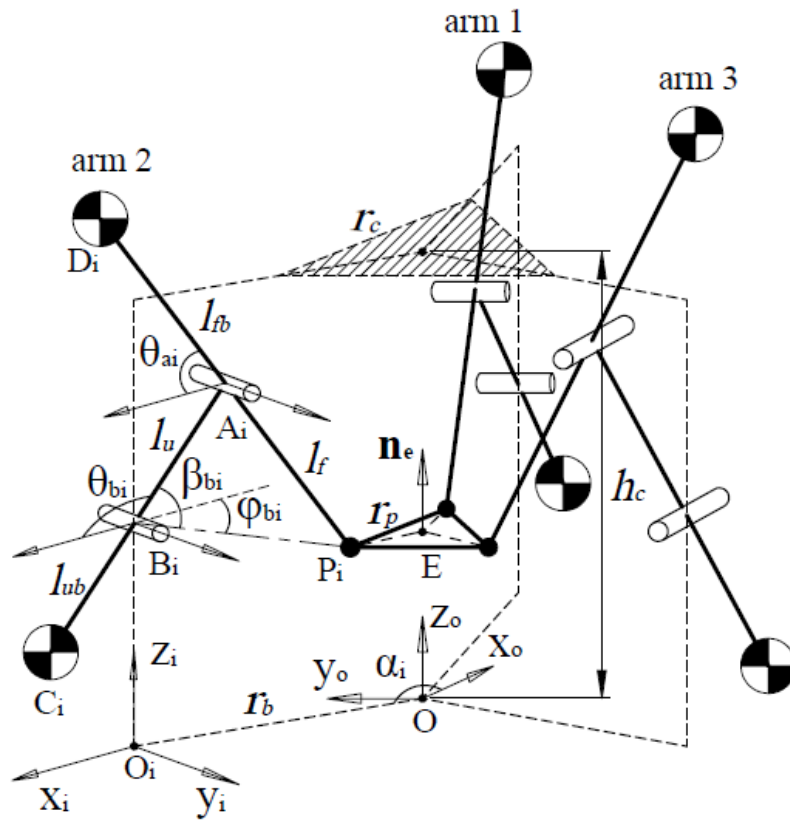### 4.4.2 Inverse Kinematics and Dynamics

The inverse kinematics and dynamics [4] [90] is employed for position, velocity and dynamic analysis.

In figure 4.4.2, each arm is set in a fixed plane. The rotation matrix Q_i about axis z_o that transforms from $x_o O z_o$ to $x_i O_i z_i$, coordinate system of each plane, is given below. Let i ($i = 1,2,3$) be the index of the three arms.

52

$$Q_i = \begin{bmatrix} cos\alpha_i & -sin\alpha_i & 0 \\ sin\alpha_i & cos\alpha_i & 0 \\ 0 & 0 & 1 \end{bmatrix} \quad (4.4.1.a)$$

The e_x, e_y and e_z are unit vectors parallel to the global coordinate axes x_o, y_o, and z_o respectively.

$$e_x = [1 \quad 0 \quad 0]^T, e_y = [1 \quad 0 \quad 0]^T, e_z = [1 \quad 0 \quad 0]^T \quad (4.4.1.b)$$

The actuated rotational joints are in position B_i.

$$OB_i = [\, r_b cos\alpha_i \quad r_b sin\alpha_i \quad z_{bi}\,]^T \quad (4.4.2)$$

The 3-R̲RS manipulator has 3 DOFs. The platform has its center at point E which has two orientation motions θ_{ex}, θ_{ey} , ($\theta_{ez} = 0$), and three linear motions x_e, y_e, z_e. The variables θ_{ex}, θ_{ey}, z_e are independent motions, while x_e, y_e are following motions.

The orientation of the platform is given as rotation matrix R in global coordinate. Its rotation angle $\theta_e = \sqrt{\theta_{ex}{}^2 + \theta_{ey}{}^2}$ is around unit axis vector $U_e = [u_x \quad u_y \quad 0]^T$, where $u_x = \frac{\theta_{ex}}{\theta_e}$, $u_y = \frac{\theta_{ey}}{\theta_e}$ [143].

$$R = \begin{bmatrix} c\theta_e + u_x{}^2(1 - c\,\theta_e) & u_x u_y(1 - c\,\theta_e) & u_y s\theta_e \\ u_x u_y(1 - c\,\theta_e) & c\theta_e + u_y{}^2(1 - c\,\theta_e) & -u_x s\theta_e \\ -u_y s\theta_e & u_x s\theta_e & c\theta_e \end{bmatrix} \quad (4.4.3.a)$$

The triangle platform has three vertices P_i that $OP_i = R_i + OE$ is perpendicular to the y_i axis, where $R_i = R \cdot [r_p cos\alpha_i \quad r_p sin\alpha_i \quad 0]^T$. Therefore x_e and y_e from $OE = [x_e \quad y_e \quad z_e]^T$ are calculated.

$$(Q_i e_y) \cdot OP_i = (Q_i e_y) \cdot (R_i + OE) = 0 \quad (4.4.3.b)$$

The rotation angles θ_{ai} θ_{bi} are calculated on each set of arms accordingly, and the solution needs to satisfy kinematic criteria to be an eligible solution.

$$\theta_{ai} = -\cos^{-1}\frac{(Q_i e_x)\cdot A_i P_i}{l_f} \qquad (4.4.3.c)$$

$$\theta_{bi} = \pi - \beta_{bi} - \varphi_{bi} \qquad (4.4.3.d)$$

where,

$$\beta_{bi} = \cos^{-1}\left(\frac{l_u{}^2+|B_i P_i|-l_f{}^2}{2l_u|B_i P_i|}\right) \qquad (4.4.3.e)$$

$$\varphi_{bi} = \sin^{-1}\left(\frac{(B_i P_i)\cdot e_y}{|B_i P_i|}\right) \qquad (4.4.3.f)$$

The positions of A_i, C_i and D_i are calculated as below.

$$OA_i = OB_i + Q_i\begin{bmatrix}\cos\theta_{bi}\\0\\\sin\theta_{bi}\end{bmatrix}l_u \qquad (4.4.4.a)$$

$$OC_i = OB_i + \frac{l_{ub}}{l_u}A_i B_i \qquad (4.4.4.b)$$

$$OD_i = OA_i + \frac{l_{fb}}{l_f}P_i A_i \qquad (4.4.4.c)$$

The compliant angle at joint A_i from x_i axis in O_i coordinate is calculated.

$$\theta_{ai} = -\cos^{-1}\frac{[A_i P_i]_{oi}\cdot e_x}{l_f} \qquad (4.4.4.d)$$

Some criteria need to be satisfied. Only meaningful results are selected from pose solution to avoid singularity and collision.

Criteria 1 judges whether a real solution of pose can be obtained.

$$l_u + l_f > |\boldsymbol{B_i P_i}| \tag{4.4.5.a}$$

Criteria 2 ensures that links are never aligned so as to avoid singularity.

$$[\boldsymbol{A_i B_i} \times \boldsymbol{A_i P_i}]_{oi} \cdot \boldsymbol{e_y} > 0 \tag{4.4.5.b}$$

Criteria 3 ensures that the arms be above the platform surface so as to avoid singularity.

$$\boldsymbol{n_e} = \boldsymbol{R_1} \times \boldsymbol{R_2} \tag{4.4.5.c}$$

$$\boldsymbol{P_i A_i} \cdot \boldsymbol{n_e} > 0 \tag{4.4.5.d}$$

Criteria 4 ensures $\boldsymbol{D_i}$ keep a distance from the $\boldsymbol{z_o}$ axis as to avoid arms collision.

$$[\boldsymbol{OD_i} - \boldsymbol{OD_i} \cdot \boldsymbol{e_z} \cdot \boldsymbol{e_z}]_{oi} \cdot \boldsymbol{e_x} > d_{min} \tag{4.4.5.f}$$

Criteria 5 limits actuation angle within operational range.

$$\theta_{bi} > \theta_{min} \tag{4.4.5.g}$$

Criteria 6 ensures that $\boldsymbol{D_i}$ is under ceiling, or is above ceiling but not touching the ceiling.

$$\boldsymbol{OD_i} \cdot \boldsymbol{e_z} < h_c \tag{4.4.5.h}$$

or,

$$ext_i \left[\frac{\boldsymbol{P_i A_i}}{|\boldsymbol{P_i D_i}|}\right]_{oi} \cdot \boldsymbol{e_x} > r_c \tag{4.4.5.i}$$

where,

$$ext_i = \frac{h_c - \boldsymbol{OP_i} \cdot \boldsymbol{e_z}}{(\boldsymbol{P_i D_i}/|\boldsymbol{P_i D_i}|) \cdot \boldsymbol{e_z}} \tag{4.4.5.j}$$

Criteria 7 ensures that $\boldsymbol{P_i}$ is above the production line surface.

$$OP_i \cdot e_z > z_{min} \qquad (4.4.5.k)$$

Once the criteria for eligible pose are given, an optimization is run for largest workspace in defined boundary. To reduce the overall machine weight by design, let balancing arm be in same length as operation arm.

The linear velocity of point P_i is v_{pi} which has a relationship with $v_e = [\dot{x}_e \quad \dot{y}_e \quad \dot{z}_e]^T$ and $\omega_e = [\dot{\theta}_{ex} \quad \dot{\theta}_{ey} \quad \dot{\theta}_{ez}]^T$, $v_{pi} = \omega_e \times R_i + v_e$. The velocity v_{pi} is perpendicular to the y_i axis.

$$(Q_i e_y) \cdot v_{pi} = (Q_i e_y) \cdot (\omega_e \times R_i + v_e) = 0 \qquad (4.4.6)$$

Also, the linear velocity of P_i can be expressed by the angular velocities at joints A_i and B_i, as v_{pi}^*. The angular velocities $\omega_{ai} = \dot{\theta}_{ai} \cdot y_i$ and $\omega_{bi} = \dot{\theta}_{bi} \cdot y_i$ can be calculated.

$$v_{pi}^* = \omega_{bi} \times B_i A_i + \omega_{ai} \times A_i P_i \qquad (4.4.7)$$

$$(Q_i e_x) \cdot v_{pi} = (Q_i e_x) \cdot v_{pi}^* \qquad (4.4.8.a)$$

$$(Q_i e_z) \cdot v_{pi} = (Q_i e_z) \cdot v_{pi}^* \qquad (4.4.8.b)$$

The linear acceleration of point P_i is a_{pi} which has a relationship with $a_e = [\ddot{x}_e \quad \ddot{y}_e \quad \ddot{z}_e]^T$ and $\alpha_e = [\ddot{\theta}_{ex} \quad \ddot{\theta}_{ey} \quad \ddot{\theta}_{ez}]^T$, $a_{pi} = \alpha_e \times R_i + \omega_e \times (\omega_e \times R_i) + a_e$. Acceleration a_{pi} is perpendicular to the y_i axis.

$$(Q_i e_y) \cdot a_{pi} = (Q_i e_y) \cdot [\alpha_e \times R_i + \omega_e \times (\omega_e \times R_i) + a_e] = 0 \qquad (4.4.9)$$

Also, the linear acceleration of P_i can be expressed by the angular acceleration at joints A_i and B_i, as a_{pi}^*. The angular accelerations $\alpha_{ai} = \ddot{\theta}_{ai} \cdot y_i$ and $\alpha_{bi} = \ddot{\theta}_{bi} \cdot y_i$ can be calculated.

$$a_{pi}^* = a_{ai} + \alpha_{ai} \times A_i P_i + \omega_{ai} \times (\omega_{ai} \times A_i P_i) \qquad (4.4.10.a)$$

$$a_{ai} = \alpha_{bi} \times B_i A_i + \omega_{bi} \times (\omega_{bi} \times B_i A_i) \qquad \text{(4.4.10.b)}$$

$$(Q_i e_x) \cdot a_{pi} = (Q_i e_x) \cdot a_{pi}{}^* \qquad \text{(4.4.11.a)}$$

$$(Q_i e_z) \cdot a_{pi} = (Q_i e_z) \cdot a_{pi}{}^* \qquad \text{(4.4.11.b)}$$

The angular accelerations α_{ci} and α_{di} are in y_i axis.

$$a_{ci} = \alpha_{bi} \times B_i C_i + \omega_{bi} \times (\omega_{bi} \times B_i C_i) \qquad \text{(4.4.11.c)}$$

$$a_{di} = a_{ai} + \alpha_{ai} \times A_i D_i + \omega_{ai} \times (\omega_{ai} \times A_i D_i) \qquad \text{(4.4.11.d)}$$

In similar way, the accelerations of the counter masses would be obtained accordingly.

One could apply D'Alembert's principle for force and moment analysis [93]. The mass m_e, m_p, m_d, and m_c are concentrated at points E, P_i, D_i and C_i. The mass m_a and m_b are evenly spread along links $P_i D_i$ and $A_i C_i$. The inertia J_a and J_b are rotational around revolute joints at A_i and B_i.

The force F_e and the moment M_e are the overall force and overall moment acting on the platform, by the inertia.

$$F_e = \sum_{i=1}^{m} \left[(a_{pi} - a_g) m_p \right] + (a_e - a_g) m_e \qquad \text{(4.4.12.a)}$$

$$M_e = \sum_{i=1}^{m} \left[R_i \times (a_{pi} - a_g) m_p \right] \qquad \text{(4.4.12.b)}$$

Force F_{pi} that acts on the platform at point P_i from the arms causes the overall reaction F_e and M_e on platform.

$$F_e = \sum_{i=1}^{m} F_{pi} \qquad \text{(4.4.12.c)}$$

$$M_e = \sum_{i=1}^{m} \left[R_i \times F_{pi} \right] \qquad \text{(4.4.12.d)}$$

The moment on the fore arm is balanced about joint A_i.

$$[A_i P_i \times (-F_{pi})]_{oi} \cdot e_y = [A_i D_i \times (a_{di} - a_g) m_d + \alpha_{ai} \cdot J_a]_{oi} \cdot e_y \qquad (4.4.13.a)$$

The force on the fore arm is also balanced. The force F_{ai} is from up arm to fore arm.

$$F_{ai} = F_{pi} + (a_{di} - a_g) m_d + (a_{ai} - a_g) m_a \qquad (4.4.13.b)$$

The forces on up arm is balanced.

$$F_{bi} = F_{ai} + (a_{ci} - a_g) m_c - a_g m_b \qquad (4.4.13.c)$$

The force and moment acting on the fore arms and the up arms shall be balanced with the inertia and acceleration given or obtained from above, at A_i and B_i. The actuation torques T_i are calculated. α_{bi} is the angular acceleration about revolute joint at B_i. The magnitude value of the T_i is T_i.

$$T_i = -(Q_i e_y) \cdot (B_i A_i \times F_{ai}) - (B_i C_i \times (a_{ci} - a_g) m_c) - \alpha_{bi} J_b \qquad (4.4.14.a)$$

$$T_i = Q_i e_y \cdot T_i \qquad (4.4.14.b)$$

The total moment on base the frame should be balanced with T_b, thus the total moment on base the frame would be zero at all time.

$$T_b = -(T_1 + T_2 + T_3) \qquad (4.4.14.c)$$

The balancing moment T_b should be output by the two balancers (flywheels) in x_o and y_o axes respectively.

$$T_{bx} = T_b \cdot e_x \qquad (4.4.14.d)$$

58

$$T_{by} = \mathbf{T_b} \cdot \mathbf{e_y} \qquad\qquad (4.4.14.e)$$

Mechanical energy and the heat loss constitute the total energy consumption of a DC motor. The transformation is reversible between electric energy and mechanical energy. When the friction is neglected, the energy consumption is solely the heat loss on the electric resistances of the DC motors which is reflected by the actuation torque squared, accumulated over operation time. The instant power $\mathbf{P_i}$ is proportional to actuation torque $\mathbf{T_i}$ squared.

$$P_i = I_i{}^2 R \propto \mathbf{T_i}{}^2 R \qquad\qquad (4.4.14.f)$$

4.4.3 Design Optimization

An optimization for largest workspace is conducted for the design based on the parameters given in table 4.4.1 which considers the manipulator's space requirements.

Over the expected search area for the three motions of the end effector which are θ_{ex} [-1.5, 1.5], θ_{ey} [-1.5, 1.5], z_e [0.5, 1.0], the design parameters are optimized from their evaluated ranges. Table 4.4.2 gives the results of the optimization for largest workspace.

Table 4.4.1 Design parameters.

Variables	Units	Values
r_b	m	1.0
r_c	m	0.3
h_c	m	2.0
α_1	rad	0.75π/3
α_2	rad	2.75π/3
α_3	rad	4.75π/3

Table 4.4.2 Optimization constraints and results.

Parameters	Units	Ranges	Results
r_p	m	[0.05, 0.1]	0.07
l_u	m	[0.2, 1.0]	0.79
l_f	m	[0.2, 1.0]	0.733
z_{bi}	m	[1.0, 1.7]	1.394

The r_p, l_u, l_f are the non-adjustable design parameters, while z_{bi} is an adjustable parameter that could be adapted thus its value obtained here would be considered as a default value for largest workspace. The result of the workspace is visualized with an enclosed convex hull in figure 4.4.3.
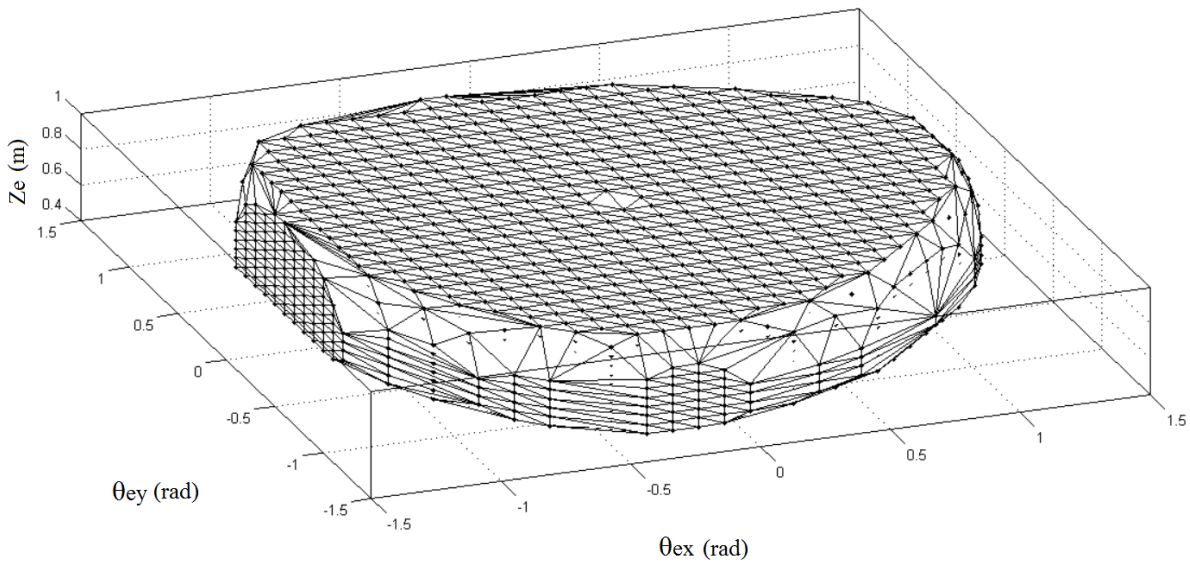
Figure 4.4.3 Largest workspace by r_p, l_u, l_f and z_{bi}.

4.4.4 Operation Optimization of Energy Consumption Index

In table 4.4.3, the end effector travels a trajectory where the three motions θ_{ex}, θ_{ey} and z_e are each expressed in a unique polynomial function, with displacement $s(t)$, velocity $\dot{s}(t)$ and acceleration $\ddot{s}(t)$. In table 4.4.3, the optimization variables are $x_1 \sim x_{12}$, where $x_1 \sim x_3$ set the adaptive relocations of $\boldsymbol{B_i}$ by z_{bi}. The key points of time $t_0 \sim t_6$ are set in the column. At t_0, t_2 and t_4, the displacement and velocity allow no alteration at all. At t_1, t_3, t_5, motion planning is optionally allowed with $x_4 \sim x_{12}$.

$$s(t) = a_{12}t^{12} + a_{11}t^{11} + \cdots + a_1t^1 + a_0t^0 \qquad (4.4.15)$$

Table 4.4.3 Trajectory features of θ_{ex}, θ_{ey} and z_e.

	t_0	t_1	t_2	t_3	t_4	t_5	t_6
t	0	1	2	3	4	5	6
$\theta_{ex}(t)$	0	x_4	0.7	x_5	-0.5	x_6	0
$\dot{\theta}_{ex}(t)$	0	NA	0.2	NA	0.2	NA	0
$\ddot{\theta}_{ex}(t)$	0	NA	NA	NA	NA	NA	0
$\theta_{ey}(t)$	0	x_7	-0.8	x_8	-0.6	x_9	0
$\dot{\theta}_{ey}(t)$	0	NA	-0.4	NA	0.3	NA	0
$\ddot{\theta}_{ey}(t)$	0	NA	NA	NA	NA	NA	0
$z_e(t)$	0.5	x_{10}	0.6	x_{11}	0.7	x_{12}	0.5
$\dot{z}_e(t)$	0	NA	0.1	NA	-0.1	NA	0
$\ddot{z}_e(t)$	0	NA	NA	NA	NA	NA	0

Based on inertial parameters in table 4.4.4, the numerical simulations are conducted.

Table 4.4.4 Inertial parameters.

Variables	Units	Values
m_a	kg	0.733
m_b	kg	0.790
m_c	kg	1.733
m_d	kg	0.500
m_e	kg	0.900
m_p	kg	0.200
J_a	$kg \cdot m^2$	0.1313
J_b	$kg \cdot m^2$	0.1643
$\boldsymbol{a_g}$	m/s^2	$[0\ 0 - 9.8]^T$

The energy index objective is accumulative with the power index over time. The whole cycle of motion needs to be divided to fine steps of time by n nodes (0.01 seconds apart), and the torques need to be calculated at each division node. At the node j, the energy index $(e)_j$ is the accumulated value of power index $(p)_j$ since the start node. When it completes a cycle at the finish node, the cost function $f = (e)_j = (e)_n$ that reflects the total energy consumption from the start node to the finish node. The genetic algorithm will optimize for the minimum value of f.

$$(p)_j = \left(T_1{}^2 + T_2{}^2 + T_3{}^2 + T_{bx}{}^2 + T_{by}{}^2 \right)_j \qquad (4.4.16.a)$$

$$(e)_j = \sum_{j=0}^{n}(p)_j \qquad (4.4.16.b)$$

$$f = (e)_n \qquad (4.4.16.c)$$

Three runs are defined according to constraints. Among the three runs, run 1 takes all default values, allowing neither relocation of joints nor motion planning of trajectory; run 2 allows joint relocation alone but no motion planning; run 3 allows joint relocation plus motion planning. In table 4.4.5, optimization results of variables $x_1 \sim x_{12}$, and the corresponding cost function f are given for run 1~3.

Table 4.4.5 Simulation results.

Run	x_1	x_2	x_3	x_4	x_5	x_6	x_7
1	1.394	1.394	1.394	-0.0732	0.2492	0.1221	-0.2808
2	1.511	1.196	1.21	-0.0732	0.2492	0.1221	-0.2808
3	1.515	1.173	1.216	0.025	0.237	0.056	-0.217

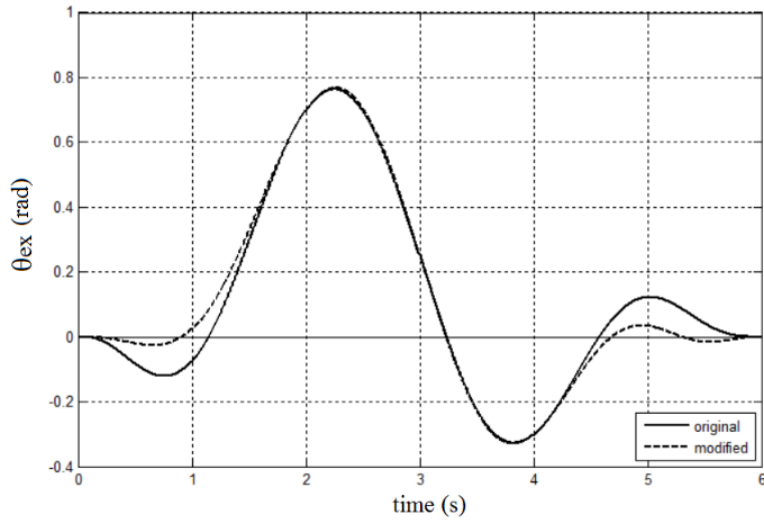| Run	x_8	x_9	x_{10}	x_{11}	x_{12}	f
1	-0.6051	0.1221	0.6083	0.7937	0.5778	1110.1
2	-0.6051	0.1221	0.6083	0.7937	0.5778	1010.8
3	-0.525	0.166	0.62	0.788	0.574	908.22

Figure 4.4.4 The displacement of θ_{ex}, solid: original; dash: modified.
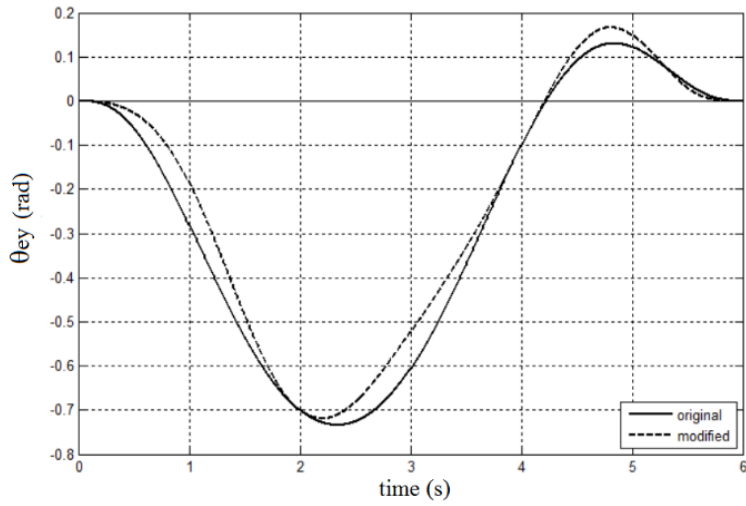

Figure 4.4.5 The displacement of θ_{ey}, solid: original; dash: modified.
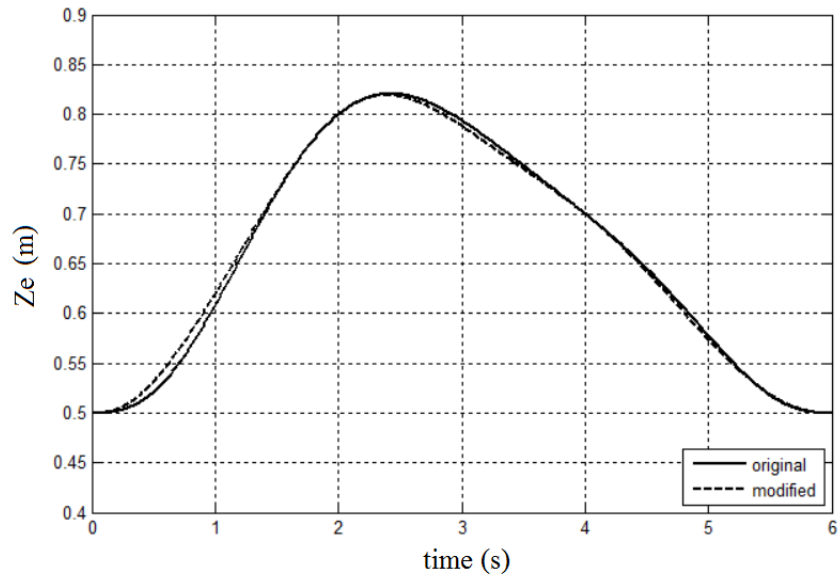
64

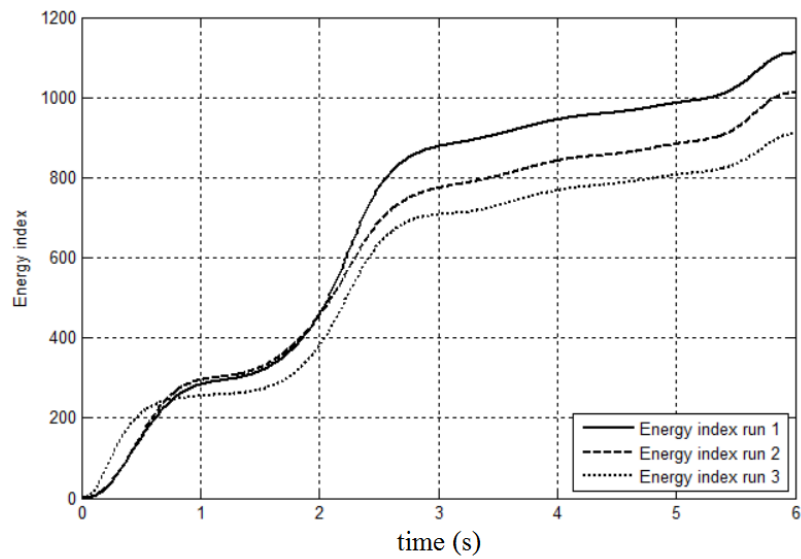Figure 4.4.6 The displacement of z_e, solid: original; dash: modified.

Figure 4.4.7 Energy index $(e)_j$ increases over time, run 1, run 2, run 3.

Table 4.4.6 Trajectory function factors.

Run		a_{12}	a_{11}	a_{10}	a_9	a_8	a_7
1	$\theta_{ex}(t)$	0	-0.0003	0.0047	-0.0398	0.2161	-0.8180
	$\theta_{ey}(t)$	0	0	0	-0.0001	0.0023	-0.0223
	$z_e(t)$	0	0	0	-0.0001	0.0008	-0.0034
2	$\theta_{ex}(t)$	0	-0.0003	0.0047	-0.0398	0.2161	-0.8180
	$\theta_{ey}(t)$	0	0	0	-0.0001	0.0023	-0.0223
	$z_e(t)$	0	0	0	-0.0001	0.0008	-0.0034
3	$\theta_{ex}(t)$	0	0	-0.0008	0.0160	-0.134	0.6020
	$\theta_{ey}(t)$	0	-0.0006	0.0085	-0.0733	0.3888	-1.3027
	$z_e(t)$	0	0.0001	-0.0017	0.01563	-0.0901	0.3367

Run		a_6	a_5	a_4	a_3	a_2	a_1	a_0
1	$\theta_{ex}(t)$	2.2409	-4.2723	4.8451	-2.2496	0	0	0
	$\theta_{ey}(t)$	0.1282	-0.4440	0.9003	-0.8451	0	0	0
	$z_e(t)$	0.0033	0.0411	-0.1847	0.2513	0	0	0.5
2	$\theta_{ex}(t)$	2.2409	-4.2723	4.8451	-2.2496	0	0	0
	$\theta_{ey}(t)$	0.1282	-0.4440	0.9003	-0.8451	0	0	0
	$z_e(t)$	0.0033	0.0411	-0.1847	0.2513	0	0	0.5
3	$\theta_{ex}(t)$	-1.4876	1.8284	-0.7968	-0.00248	0	0	0
	$\theta_{ey}(t)$	2.7363	-3.4804	2.5779	-1.0716	0	0	0
	$z_e(t)$	-0.8202	1.2826	-1.2416	0.6385	0	0	0.5

The values of $x_4 \sim x_{12}$ in table 4.4.5 will be interpreted to the displacement/velocity/acceleration polynomial functions for run1~3 in table 4.4.6. The results are plotted in figure 4.4.4 ~ figure 4.4.7. Run 3 saves more energy than run 2, while run 1 takes highest energy consumption.

4.4.5 Theory Verification

The dynamic model of the 3-<u>R</u>RS is a group of rigid bodies that are connected by mechanical joints. These elements have been established as editable blocks in Simulink library. The Simulink simulation verifies the dynamic model based on classical Newton second law. The Simulink model in linked blocks (figure 4.4.8) practices a sample task to validate the driving torques and dynamic balancing. The modeled structure in 3D and its calculated dynamic motion could be viewed from the visualization window (figure 4.4.9). So that one could check that the model is correctly built.

The inputs to the joint actuators are the required angular motions of joint B_i of run1. The reaction torques $-T_i$ are measured from sensors which match the theoretical calculation (figure 4.4.10). Furthermore, the reaction forces on base are measured at the B_i joints which are equivalent to the gravity of the manipulator (figure 4.4.11). The shaking forces is eliminated.

The dynamic simulation for a group of jointed rigid bodies is a common and mature function in Simulink, of which the results can be trusted. The theoretical results and simulated results also mutually prove each other. The experiments of real prototype may have errors due to manufacturing/control defects thus is not recommended, while the Simulink could build an ideal model for theory verification.
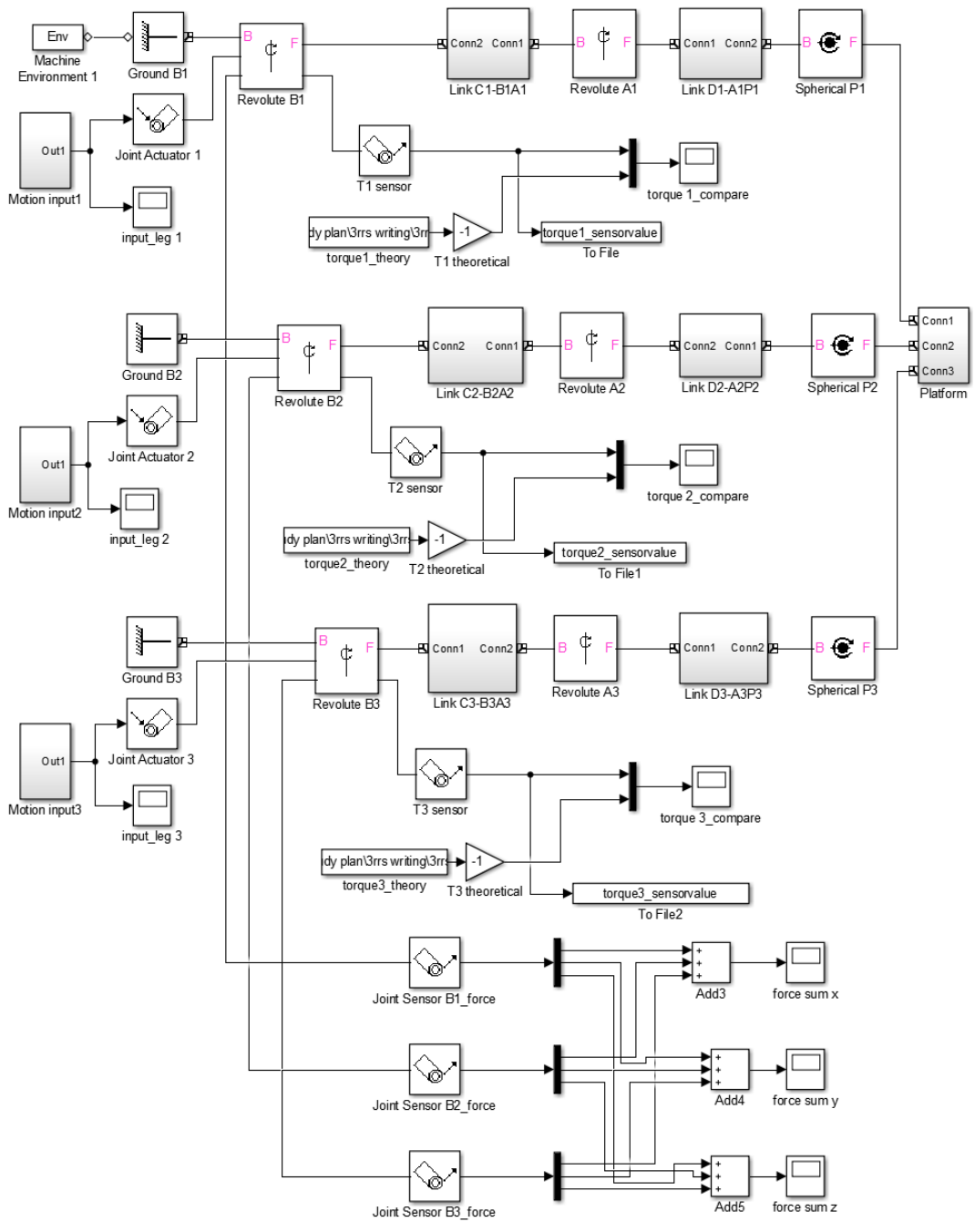
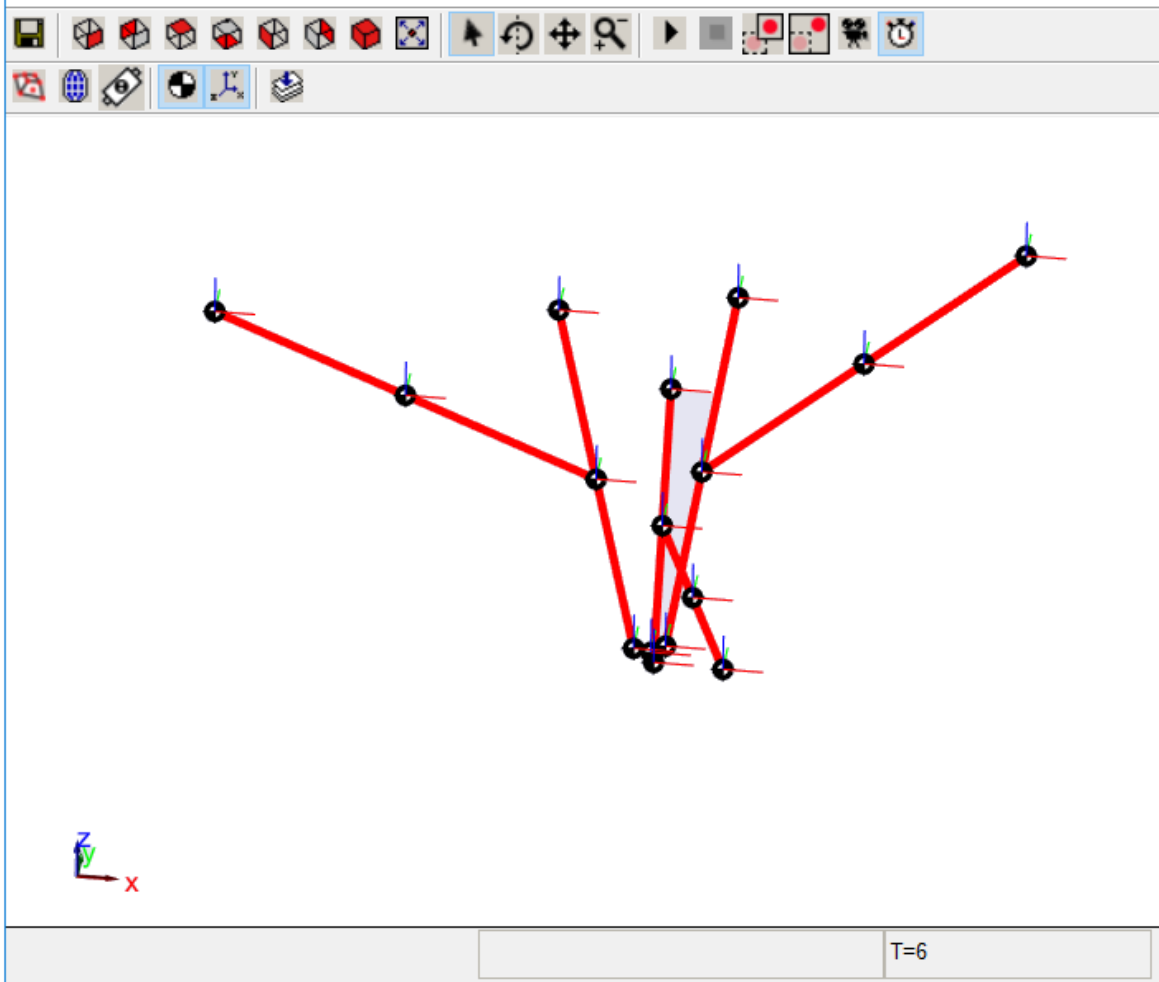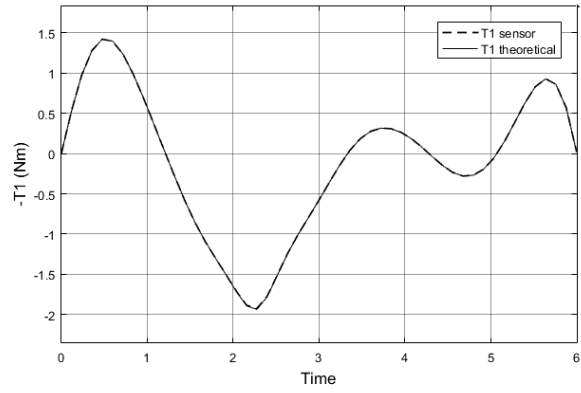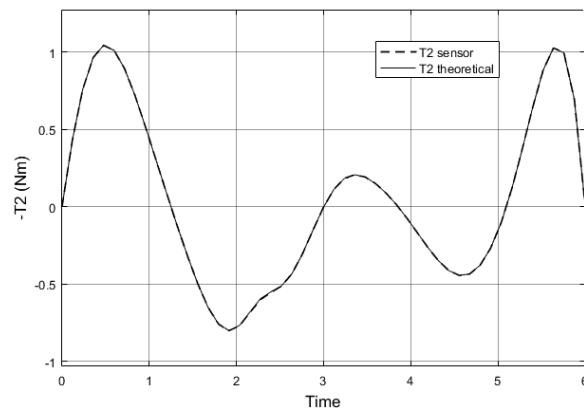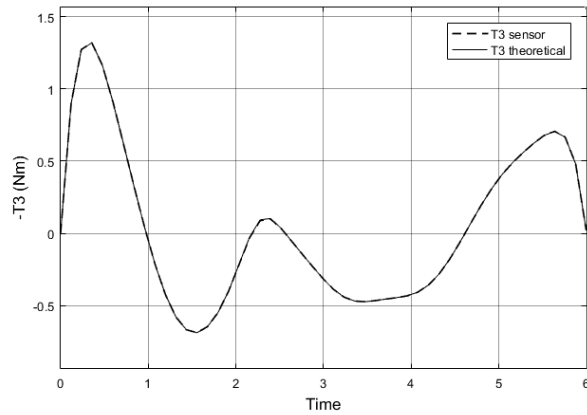Figure 4.4.8 The Simulink model of the manipulator in blocks.

Figure 4.4.9 The Simulink model of the manipulator in 3D visualization window.

(a)

(b)

(c)

Figure 4.4.10 The reaction torques $-T_1$, $-T_2$ and $-T_3$ sensor value and theoretical value.
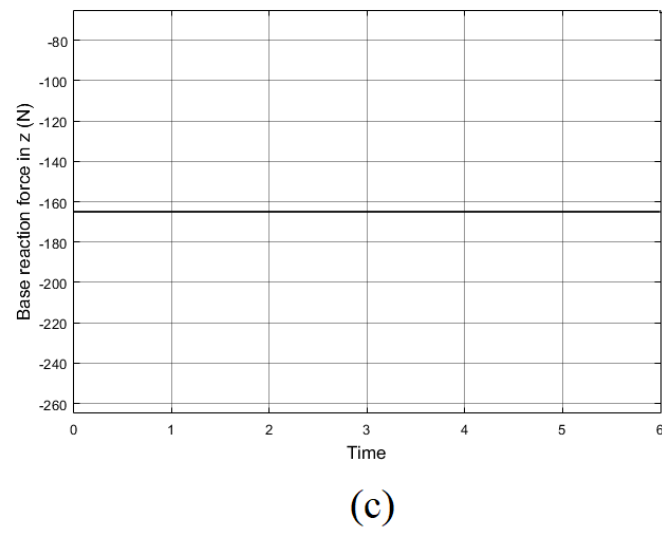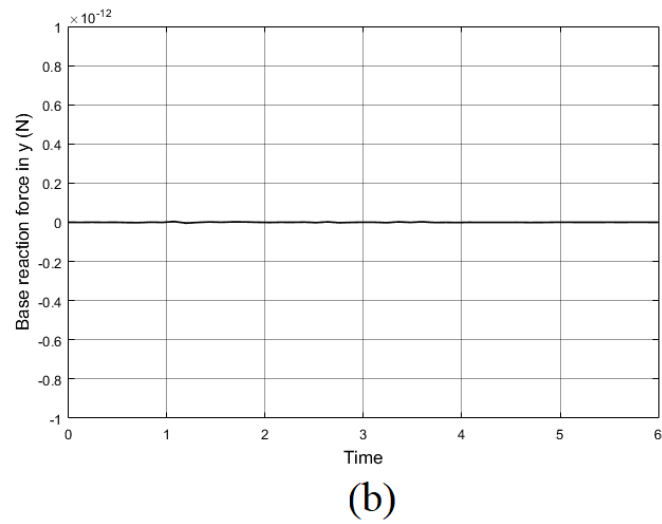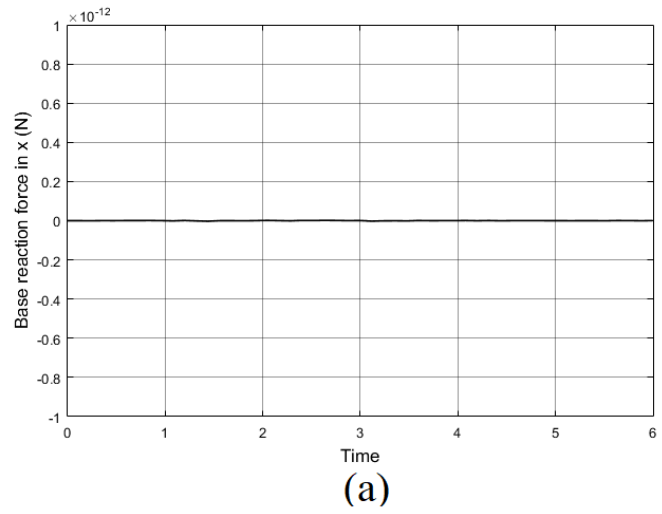
Figure 4.4.11 The base reaction forces along x_o, y_o and z_o axes.

4.4.6 Section Conclusion

A balanced 3-R̲RS parallel manipulator is designed with passive force balancing and active moment balancing. Joints relocation and trajectory planning are the adaption that provides solution to energy saving while the task requirements of the motion are satisfied. When more variables are involved, the better optimization results would be obtained. The structural adaption plus motion planning yields the best optimization effect. The dynamic model is verified by Simulink simulation. In automated manufacturing industry that largely rely on parallel robotic manipulators, the adaption promotes environment-friendly green operations as large amount of energy can be saved in repeated cyclic motions on production lines. The energy saving impact would be remarkable when this design and its method are implemented on large scale.

4.5 Combination for High DOF Mechanism

Fully parallel robots of high-DOF have more limbs that restrict the workspace. Balancer or limb interference avoidance is more complex. Serial type hybrid robots have larger workspace but the increased load on platform greatly increase the counter mass on the parallel limbs which could take more energy. The design is a challenge. Structure adaption is even more challenging.

The (2-R̲R)R and 3-R̲RS are interference free and structural adaptive. They could be combined. The combined manipulator is interference free. The DOF is combined and the structural adaption is also combined.

When the (2-<u>R</u>R)R planar manipulator adds one more motor at the end effector, this manipulator will have 3 DOFs that are two translations and one rotation on a plane. The combined (2-<u>R</u>R)<u>R</u> and 3-<u>R</u>RS will have 6 DOF in total.

There are merits of the combined manipulator compared to an individual manipulator with same DOFs. It uses a separate planar manipulator, the (2-<u>R</u>R)<u>R</u>, for planar motions instead of having to move the 3-<u>R</u>RS. therefore it is simpler and lighter. It requires less actuation energy as the actuation is distributed to two manipulators.

This application of the design could be in manufacturing where one manipulator holds a work piece and the other manipulator is working on it.
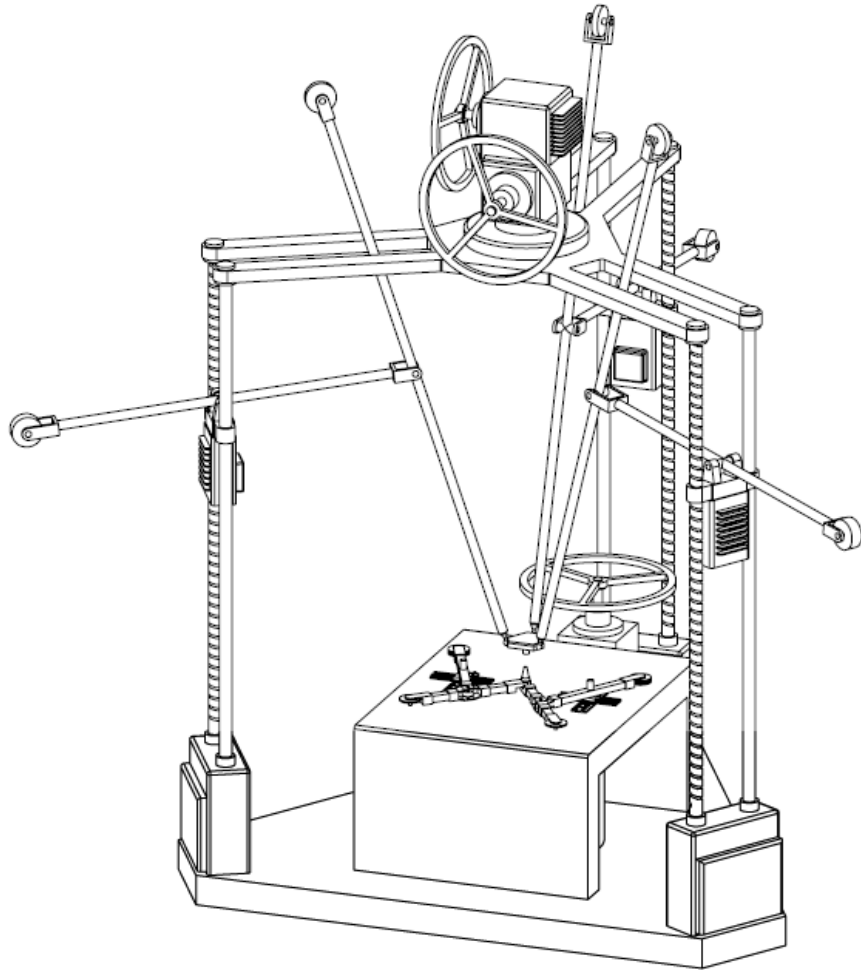
Figure 4.5.1 The combination of balanced robots.

4.6 Chapter Conclusion

This chapter discusses the interference-free design for dynamically balanced manipulators and their energy consumption optimization. The passive force balancing and active moment balancing are integrated for a planar (2-RR)R robot and a spatial 3-RRS robot dynamic balancing solution. The configurations are changed through middle revolute joint angle reversal to avoid link

interference. The structure adaption and motion planning are conducted for optimal energy purposes. As is seen from the planar (2-$\underline{R}$R)R operations, the structural adaption could reduce energy consumption for a certain trajectory and the optimization effect depends on the trajectory. As is seen from the spatial 3-$\underline{R}$RS operations, the structural adaption alone could save energy while the integration of structural adaption and motion planning could save more energy. The inclusion of more variables could result to better optimization effect. The dynamic model of the spatially balanced 3-$\underline{R}$RS manipulator obtained by D'Alembert's principle is verified by Simulink.

The planar 2-DOF (2-$\underline{R}$R)R robot can be modified to become a planar 3-DOF (2-$\underline{R}$R)R robot which is to be combined with 3-$\underline{R}$RS to make a 6-DOF balanced robot interference-free. Structural adaptions are also combined from two manipulators which simplifies the complexity of structure. The five joints with adaptive relocation in the combined machine conveniently offer many opportunities for optimization. The actuation loads are distributed to two manipulators which make the combined 6-DOF manipulator lighter, simpler and energy saving.

Chapter 5 Deployable 3-DOF P*U* Parallel Manipulators

5.1 Chapter Introduction

This chapter discusses the re-design of 3-DOF P*U* parallel manipulators with adaptive features for optimization. The applications of the designs are in solar tracking.

As the sun rises in the east, sets in the west and inclination angle changes with seasons, the solar trackers are designed to follow the sun. There are some designs of solar trackers. A 1-DOF solar tracker is designed with one rotation [144]. Serial robots of 2-DOF [145] [146] so that the tracker could rotate from east to west and from north to south. The solar panel is heavy. As the parallel robots have advantages in precision and loading, some solar trackers are designed with parallel manipulator as the stand. A parallel solar tracker is designed with 2-DOF [147] for the two rotation angles. A parallel tracker is designed with 2R1T 3-PRS [148] so it has one more vertical translational motion in addition to the two rotations. Another 2R1T parallel structure is designed with 3-RPS [149]. The parallel tracker which could provide two rotations and one vertical translation has one more degree of freedom. It provides convenience for repair and maintenance, while some performance such as stiffness or actuation could be optimized through adjustable height of the platform.

Although one could find plenty of solar tracker designs, the deployable re-design of the solar trackers and relevant researches are rare.

 The solar panel is a large surface. Wind loads on panel needs to be considered. As suggested in researches [150] and [151], the wind loads could be divided to a lift force and a drag force, where

the lift force is normal to the panel and the drag force is parallel to the panel. Storm hazards are frequent in tropical Asia Pacific regions [119]. In North America, the news report of solar field destroyed by storm or tips of storm protection [120] [121] are heard.

Wind is a destructive power but also a clean source of energy. Piezo materials could convert mechanical motion or deformation to electric energy [152]. Piezo chips are used in several designs to collect energy from wind loads [153] [154] [155]. Besides wind energy, some structure is designed to harvest energy from mechanical motion. A 6-DOF parallel structure is designed which is not actuated by motors but passively receive vibration for energy harvesting [156].

Parallel solar trackers could be designed to harvest energy from wind loads on the large solar panel which makes them hybrid energy harvesters. The parallel manipulators have higher stiffness and loads capacity suitable for working in the winds and can be re-designed with deployable function that allows them to lie down for storm protection. Adaption is considered and added to the original structure for optimization.

The minimum deployable height could be determined after evaluation of loading capacity and other constraints.

An adjustable 3-PRS solar tracking stand is designed to show the concept of deployable solar tracker with lie-flat function. The larger workspace and higher general stiffness are the outcome of multi-objective optimization through structural adaption.

Another adjustable 3-RPS hybrid energy harvester is designed considering the operational requirements of dust proof and real models of actuation products are selected for the design. Minimum height algorithm and Jacobian transformation are developed to assist the evaluation of the design. Piezo chips are included for wind energy harvesting.

5.2 Theories and Methodologies

The design needs to provide a folded pose considering the loading capacity and the retracted length of the actuators. A lie-flat vectors diagram is given in the design of 3-R<u>P</u>S parallel manipulator which determines the height of the platform at lie-flat pose.

Minimum platform height algorithm is the intersection of qualified solutions for constraints. This algorithm could rapidly calculate the eligible orientations of the platform due to the nature of solar tracking functions.

Jacobian matrix is modified to analyse the stiffness in directions other than the cartesian global coordinate axes. This assists the stiffness evaluation in practical situation where the wind loads may be horizontal in any direction.

The 3-<u>P</u>RS and 3-R<u>P</u>S are designed with adjustable base joint locations for optimization. Paper [78] discussed a 3-<u>P</u>RS robot which changes between different operational modes through the rail angle adjustments. The angles or locations of the base joints could indicate a specific operational mode the manipulator is in. The working and lie-flat are two operational modes of solar trackers as well.

5.3 Adaptive 3-<u>P</u>RS Parallel Manipulator

The solar tracking stand adjusts its pose timely to have the solar panel properly face to the moving sun. A 3-<u>P</u>RS parallel manipulator is designed that provides high stiffness and easy maintenance. The structural adaption of the 3-<u>P</u>RS parallel stand allows further optimization of workspace and

stiffness with respect to seasons. The research discusses an optimized design for green energy collection.

5.3.1 The 3-PRS Mechanism Design

The solar tracking stand needs to be designed satisfying large workspace, high stiffness, and easy maintenance. The parallel legs of the stand share the load of the panel, and reduce the deformation thus taking the advantage of higher stiffness. Besides the advantage in stiffness, it should facilitate maintenance. The design should be able to reach a pose to avoid storm damage. This design can keep the solar panel flat and in a very low position when destructive weather occurs.

The non-adaptive 3-PRS stand (figure 5.3.1 (a)) with flat base rails on the ground can fold its legs and stay low, close to the ground when strong storms hit so as to protect the structure from the powerful blow on its panel face (figure 5.3.1 (b)). And the motion of the platform in vertical way helps to adjust the height for convenience in panel maintenance and repair. The concept of adaptive can be considered to have the prismatic rails adjustable in the inclination angle to the ground (figure 5.3.1 (c)). The main benefit of the structure adaption is that it adds more parameters to be tuned in favor of the operation conditions, while it can still reach the storm protection pose (figure 5.3.1 (d)).

The adaptive 3-PRS is the design to be discussed in this section. The adjustable prismatic rails can set the inclination angles. The slider moves along the rail, and is attached to the bottom of the leg with a revolute joint. At the top of the leg, it is attached to the platform each with a spherical joint. There are three identical sets of adaptive rails and legs, each can be adjusted individually. The structure can be written in full as 3-$\underline{PR}^*\underline{PRS}$.
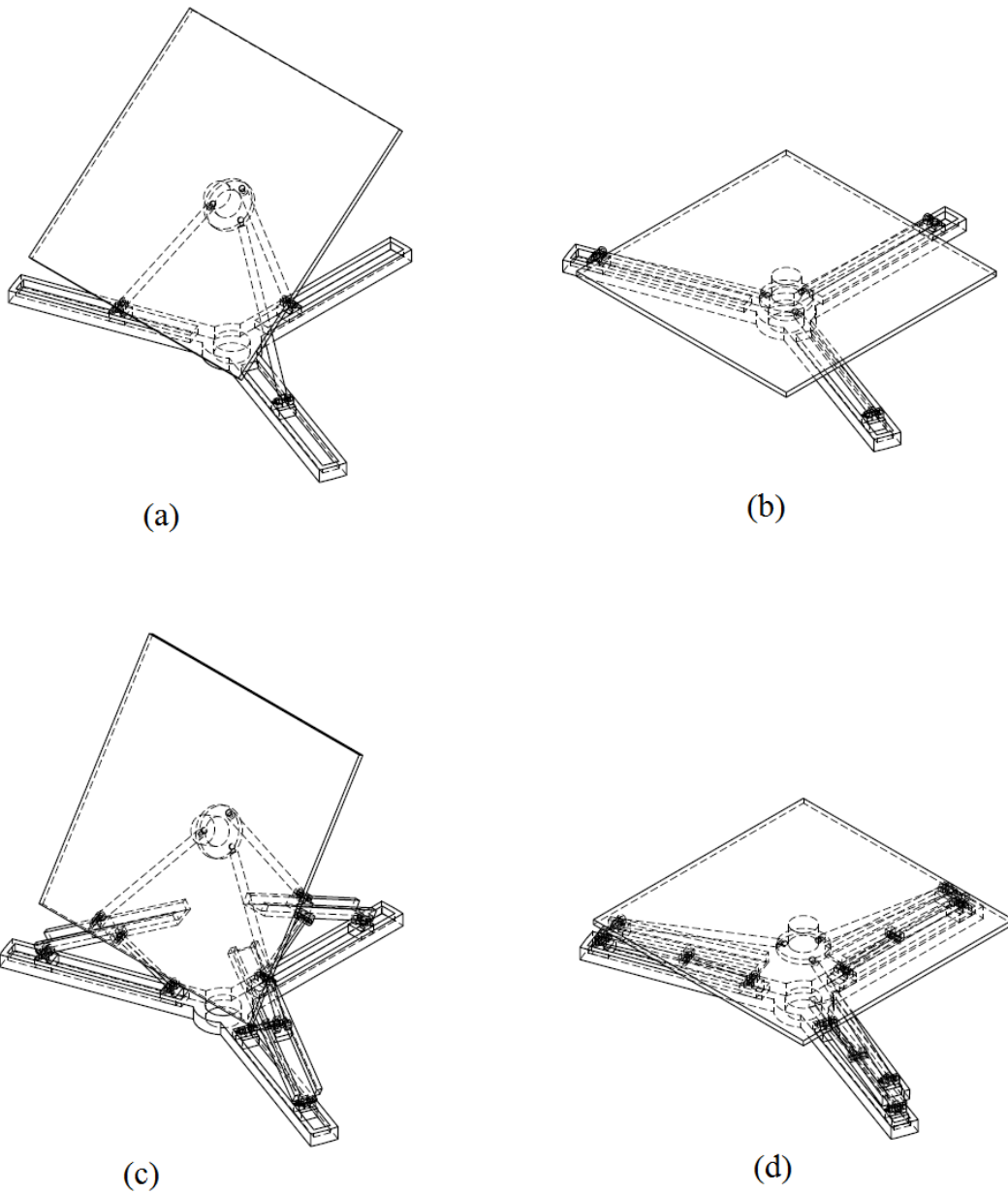
courtesy of ASME

Figure 5.3.1 The 3-PRS parallel stand. (a) non-adaptive 3-PRS design; (b) storm protection pose for non-adaptive design; (c) adaptive 3-PRS design; (d) storm protection pose for adaptive design.

5.3.2 Inverse Kinematics and Stiffness

(a)

(b)
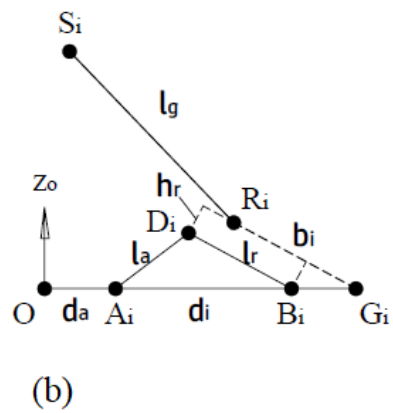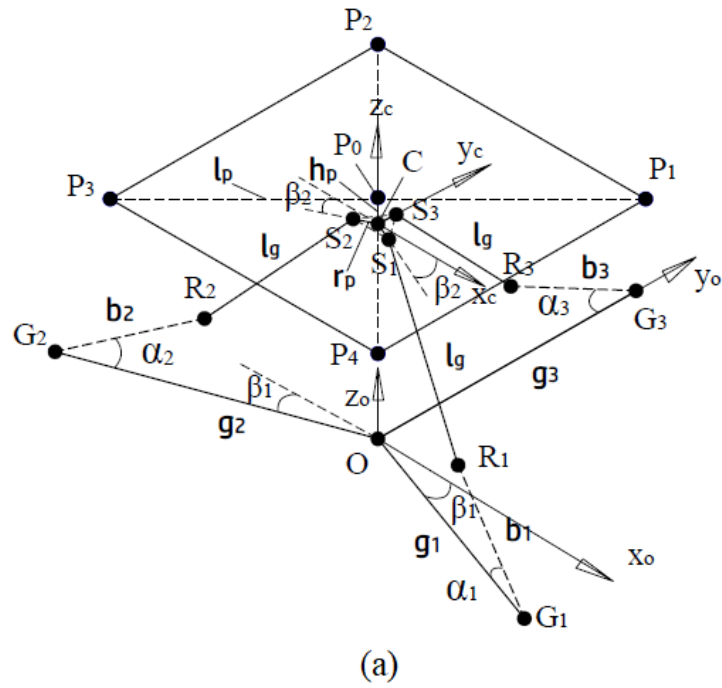
courtesy of ASME

Figure 5.3.2 The structure for analysis. (a) the stand; (b) the rail and leg set.

As is shown in figure 5.3.2, a square solar panel is mounted on the top of the stand with four vertices P_i at a distance of l_p from the panel center at P_0. A moving coordinate $x_c y_c z_c$ is set at point C which is the center of the platform attached to the three spherical joints, and it is under the solar panel center P_0 by distance h_p. The spherical joints are represented with points S_i, and the revolute joints at the end of the leg are R_i. The length of the leg l_g is measured from the spherical joint to the revolute joint. The slider attached to these revolute joints slide along the rails parallel to rail bottom line $D_i B_i$, which connects revolute joints at D_i and B_i. The revolute joint R_i measures a distance h_r from $D_i B_i$. There is a revolute joint A_i on each base guideway. The distance d_i is adjusted to adjust the rail inclination angle α_i. A line parallel to $D_i B_i$ passing revolute joint R_i intersect the ground at point G_i, which is an imaginary point. A fixed coordinate $x_o y_o z_o$ is at the point O where the three ground guide ways meet.

The coordinate axes are given below.

$$x_o = [1 \quad 0 \quad 0]^T, \ y_o = [0 \quad 1 \quad 0]^T, \ z_o = [0 \quad 0 \quad 1]^T \tag{5.3.1}$$

The rail inclination angle is adjusted as the equation explains.

$$\alpha_i = \cos^{-1}(\frac{l_r^2 + d_i^2 - l_a^2}{2 l_r d_i}) \tag{5.3.2.a}$$

and it is adjusted through sliders on the base guideways.

$$g_i = d_a + d_i + \frac{h_r}{\sin \alpha_i} \tag{5.3.2.b}$$

Inverse Kinematic method is used to solve for the actuator positions based on the given end effector positions. The orientation of the platform is R_{xy}. The positions of the spherical joints are calculated.

$$S_i = R_{xy}S + C \qquad (5.3.3.a)$$

where

$$R_{xy} = \begin{bmatrix} \cos\theta_y & 0 & \sin\theta_y \\ \sin\theta_x\sin\theta_y & \cos\theta_x & -\sin\theta_x\cos\theta_y \\ -\cos\theta_x\sin\theta_y & \sin\theta_x & \cos\theta_x\cos\theta_y \end{bmatrix} \qquad (5.3.3.b)$$

and the spherical joints positions with reference to the platform center are expressed as below,

$$S = [r_p \cos\beta_{Gi} \quad r_p \sin\beta_{Gi} \quad 0]^T \qquad (5.3.3.c)$$

Where

$$\beta_{G1} = -\beta_1, \beta_{G2} = \pi + \beta_2, \beta_{G3} = \frac{\pi}{2} \qquad (5.3.3.d)$$

and the center of the moving platform, center of the spherical joints, is positioned as below.

$$C = [x_c \quad y_c \quad z_c]^T \qquad (5.3.3.e)$$

The three coordinates of S_i is given below.

$$S_i = [s_{ix} \quad s_{iy} \quad s_{iz}]^T \qquad (5.3.3.f)$$

The S_i points are in three vertical planes.

$$s_{3x} = 0 \text{ and } s_{2y} = s_{2x}\tan\beta_{s2} \qquad (5.3.3.g)$$

83

So that

$$x_c = -r_p \cos\beta_{s3} \cos\theta_y \tag{5.3.3.h}$$

$$y_c = r_p(\cos\beta_{s2} - \cos\beta_{s3}) \cos\theta_y \tan\beta_{s2} + r_p(\sin\beta_{s2} \cos\theta_x - \cos\beta_{s2} \sin\theta_x \sin\theta_y) \tag{5.3.3.i}$$

The revolute joints at the bottom of each leg is represented by $\boldsymbol{R_i}$, where b_i is to be solved.

$$\boldsymbol{R_i} = [r_{ix} \quad r_{iy} \quad r_{iz}]^T \tag{5.3.4.a}$$

$$\boldsymbol{R_i} = [(g_i - b_i\cos\alpha_i)\cos\beta_{Gi} \quad (g_i - b_i\cos\alpha_i)\sin\beta_{Gi} \quad b_i\sin\alpha_i]^T \tag{5.3.4.b}$$

The length of three legs are known.

$$|\boldsymbol{S_i R_i}| = l_g \tag{5.3.5}$$

The relationship can be written using the expressions given above.

$$(s_{ix} - r_{ix})^2 + (s_{iy} - r_{iy})^2 + (s_{iz} - r_{iz})^2 = l_g{}^2 \tag{5.3.6}$$

So that the actuator positions about b_i are solved from the quadratic equation.

$$\boldsymbol{G_i} = [g_{ix} \quad g_{iy} \quad g_{iz}]^T \tag{5.3.7.a}$$

$$a_{bi} = \cos^2\alpha_i \cdot \cos^2\beta_{gi} + \cos^2\alpha_i \cdot \sin^2\beta_{gi} + \sin^2\alpha_i \tag{5.3.7.b}$$

$$b_{bi} = 2\cos\alpha_i \cdot \cos\beta_{gi} \cdot (s_{ix} - g_{ix}) + 2\cos\alpha_i \cdot \sin\beta_{gi} \cdot (s_{iy} - g_{iy}) - 2s_{iz} \cdot \sin\alpha_i \tag{5.3.7.c}$$

$$c_{bi} = (s_{ix} - g_{ix})^2 + (s_{iy} - g_{iy})^2 + s_{iz}{}^2 - l_g{}^2 \tag{5.3.7.d}$$

$$b_i = \frac{-b_{bi} - \sqrt{b_{bi}{}^2 - 4a_{bi}c_{bi}}}{2a_{bi}} \tag{5.3.7.e}$$

The actuator displacements are solved, but there are poses that need to be avoided, so that criteria need to be set for eligibility of poses. Only the solutions that make sense can be considered as valid.

Criteria 1. The edge of the platform should be above ground. So all the vertices are above the ground.

$$(P_j)_z > 0, j = 1,2,3,4 \qquad (5.3.8.a)$$

Criteria 2. The leg should be above the rail, and the leg with rail should be under the platform.

For the leg to be above the inclined rails, the following criteria need to be met.

$$n_o = [0 \quad 0 \quad 1]^T \qquad (5.3.8.b)$$

$$dp_{gi} = \left((n_o \times OG_i) \times G_iR_i\right) \cdot R_iS_i > 0 \qquad (5.3.8.c)$$

For the leg and rail to be under the platform surface, the following criteria should be met.

$$n_c = P_1P_2 \times P_2P_3 \qquad (5.3.9.a)$$

$$P_o = \frac{(P_1+P_3)}{2} \qquad (5.3.9.b)$$

$$dp_{si} = P_0G_i \cdot n_c < 0 \qquad (5.3.9.c)$$

Criteria 3. The actuator displacements b_i need to be real positive values. And the slider needs to stay on the rail.

$$\left(b_i - \frac{h_r}{tan\alpha_i}\right) \in [r_{min}, r_{max}] \qquad (5.3.10)$$

The Jacobian matrix represents the relationship between velocities of actuators and end effector.

An algebraic method for solution to 3-PRS manipulator can be found in [14].

The relationship of the constant leg length is utilized to obtain the matrix.

$$e_i = (s_{ix} - r_{ix})^2 + (s_{iy} - r_{iy})^2 + (s_{iz} - r_{iz})^2 - l_g{}^2 \qquad (5.3.11.\text{a})$$

So that,

$$e_i = (\cot^2 \beta_{Gi} + 1) \cdot (s_{iy} - r_{iy})^2 + (s_{iz} - r_{iz})^2 - l_g{}^2 \qquad (5.3.11.\text{b})$$

First, the actuator displacement about spherical joint is found. (This equation below is modified

from the one in [28] to reflect the mutual relationship between δs_{ix} and δs_{iy}.)

$$\left(\frac{\partial e_i}{\partial b_i}\right) \delta b_i = \begin{bmatrix} \dfrac{\partial e_i}{\partial s_{iy}} & \dfrac{\partial e_i}{\partial s_{iz}} \end{bmatrix} \cdot [\delta s_{iy} \quad \delta s_{iz}]^T \qquad (5.3.11.\text{c})$$

Then the motion of actuators is related to the end effector.

$$[\delta s_{iy} \quad \delta s_{iz}]^T = [J_i][\delta \theta_x \quad \delta \theta_y \quad \delta z_c]^T \qquad (5.3.12.\text{a})$$

where,

$$[J_i] = \begin{bmatrix} \dfrac{\partial s_{iy}}{\partial \theta_x} & \dfrac{\partial s_{iy}}{\partial \theta_y} & \dfrac{\partial s_{iy}}{\partial z_c} \\ \dfrac{\partial s_{iz}}{\partial \theta_x} & \dfrac{\partial s_{iz}}{\partial \theta_y} & \dfrac{\partial s_{iz}}{\partial z_c} \end{bmatrix} \qquad (5.3.12.\text{b})$$

So that, the actuator displacement is solved. This is expressed in an equation about the end effector.

$$\delta b_i = \begin{bmatrix} \dfrac{\partial e_i}{\partial s_{iy}} \Big/ \dfrac{\partial e_i}{\partial b_i} & \dfrac{\partial e_i}{\partial s_{iz}} \Big/ \dfrac{\partial e_i}{\partial b_i} \end{bmatrix} [J_i][\delta \theta_x \quad \delta \theta_y \quad \delta z_c]^T \qquad (5.3.13)$$

The Jacobian matrix is built from the above equations.

86

$$J = \begin{bmatrix} \left[\dfrac{\partial e_1}{\partial s_{1y}} \Big/ \dfrac{\partial e_1}{\partial b_1} \quad \dfrac{\partial e_1}{\partial s_{1z}} \Big/ \dfrac{\partial e_1}{\partial b_1}\right] [J_1] \\[2ex] \left[\dfrac{\partial e_2}{\partial s_{2y}} \Big/ \dfrac{\partial e_2}{\partial b_2} \quad \dfrac{\partial e_2}{\partial s_{2z}} \Big/ \dfrac{\partial e_2}{\partial b_2}\right] [J_2] \\[2ex] \left[\dfrac{\partial e_3}{\partial s_{3y}} \Big/ \dfrac{\partial e_3}{\partial b_3} \quad \dfrac{\partial e_3}{\partial s_{3z}} \Big/ \dfrac{\partial e_3}{\partial b_3}\right] [J_3] \end{bmatrix} \qquad (5.3.14.a)$$

where

$$\frac{\partial e_i}{\partial s_{iy}} = 2(\cot^2 \beta_{Gi} + 1)(s_{iy} - r_{iy}) \qquad (5.3.14.b)$$

$$\frac{\partial e_i}{\partial s_{iz}} = 2(s_{iz} - r_{iz}) \qquad (5.3.14.c)$$

and

$$\frac{\partial e_i}{\partial b_i} = 2b_i - 2s_{iz} sin\alpha_i + 2cos\alpha_i \left[cos\beta_{gi}(s_{ix} - g_i cos\beta_{gi}) + sin\beta_{gi}(s_{iy} - g_i sin\beta_{gi})\right] \quad (5.3.14.d)$$

The end effector stiffness K is calculated with the actuation stiffness K_J.

$$K = J^T K_J J \qquad (5.3.15)$$

The general stiffness (global stiffness) the summation of the diagonal elements of matrix, judges the overall stiffness performance of a mechanism and is to be optimized.

$$g_s = K(1,1) + K(2,2) + K(3,3) \qquad (5.3.16)$$

5.3.3 Adaption and Operation Optimization

The solar tracking stand is expected to have a large workspace to follow the motion of the sun and it needs high stiffness to restrict deformation due to the wind blow. To maximize both workspace and general stiffness of the parallel stand, the Pareto front can be used to find the optimized points.

87

Optimization with regards to the changing seasons can serve the objectives better than keeping the same configuration for the whole year. This is a benefit of having adaptive solar tracking stand.

With Pareto front, it is capable to practice double objective optimization. In MATLAB, it seeks minimum value. In order to seek maximum, the value is presented in minus. The two objectives are given below.

$$f_1 = -n \qquad (5.3.17.a)$$

$$f_2 = -ln((\textstyle\sum_{i=1}^{n} g_s)/n) \qquad (5.3.17.b)$$

where the first objective is to count eligible points in a given area by defined intervals so as to measure the workspace, while the second objective is to calculate the natural logarithm of general stiffness on average for all the points counted in the first objective. The two objectives serve as the cost functions of the optimization.

The above two objectives are dependant on selected seasons. There is a pre-optimization before this two-objective operation optimization. The pre-optimization guides the setting of design parameters in table 5.3.1.

The workspace is defined as a coordinate with respect to θ_x and θ_y based on the installation position that has x axis of the base align with the east-west and y axis align with north-south. Suppose the required motions during each season are located in areas separated with boundaries by the parabola (figure 5.3.3), the points within a given area represent the orientations needed for the solar tracking in this season. This allows seasonal optimization for best workspace and general stiffness. The parabola boundaries vary when latitude changes.

The parameters are in table 5.3.2.

Table 5.3.1 Design parameters of the adaptive stand.

Parameters	Unit	Values
β_{pi}	rad	$[\frac{\pi}{4}, \frac{\pi}{2}, \frac{3\pi}{4}, \pi]$
h_p	m	0.05
β_1	rad	$\frac{\pi}{6}$
β_2	rad	$\frac{\pi}{6}$
r_p	m	0.04
l_g	m	0.4
l_p	m	0.5
$K_{a,e,n}$	N/m	100000
d_a	m	0.08
h_r	m	0.05
l_a	m	0.16
l_r	m	0.16

Parabola 0:

$$\theta_x = a_0 \theta_y{}^2 + c_0 \qquad\qquad (5.3.18.a)$$

Parabola 1:

$$\theta_x = a_1 \theta_y{}^2 + c_1 \qquad\qquad (5.3.18.b)$$

Parabola 2:

$$\theta_x = a_2 \theta_y{}^2 + c_2 \qquad\qquad (5.3.18.c)$$

Parabola 3:

$$\theta_x = a_3 \theta_y{}^2 + c_3 \qquad\qquad (5.3.18.d)$$

Table 5.3.2 Parabola definition about seasons.

	i=0	i=1	i=2	i=3
a_i	0.1	0.1	0.1	-0.1
c_i	-1.2	-0.7	-0.3	0.3

The optimization and result are analyzed with regard to seasons. For a given point (θ_x^*, θ_y^*) in workspace, the equations below determine which season it belongs to.

$$\theta_{xi} = a_i(\theta_y^*)^2 + c_i, i = 0,1,2,3 \qquad (5.3.19.a)$$

Winter:

$$\theta_{x0} \leq \theta_x^* \leq \theta_{x1} \qquad (5.3.19.b)$$

Fall/Spring:

$$\theta_{x1} < \theta_x^* < \theta_{x12} \qquad (5.3.19.c)$$

Summer:

$$\theta_{x2} \leq \theta_x^* \leq \theta_{x3} \qquad (5.3.19.d)$$

The optimization using Pareto front is practiced for each season (figure 5.3.4). The optimized result with largest workspace is chosen, meanwhile the general stiffness is also at its maximum with the workspace reached.
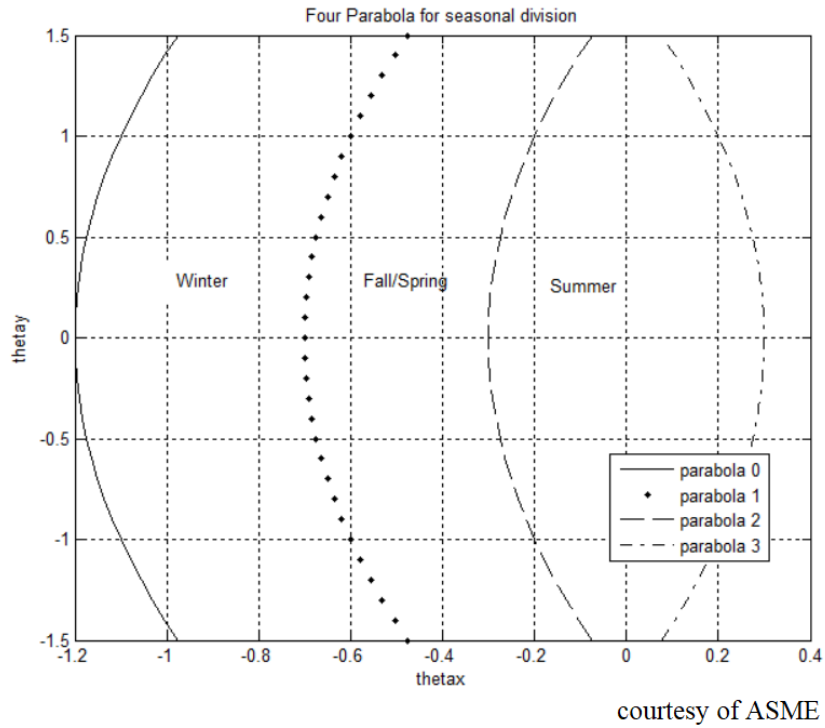
Figure 5.3.3 Four parabola for seasonal division.

The table 5.3.3, 5.3.4 and 5.3.5 shows the adjustment of d_1, d_2, d_3 and z_c, with optimized results for each season respectively.

Table 5.3.3 Winter optimization.

Parameters	Unit	Range	Values
d_1, d_2	m	[0.1,0.32]	0.167
d_3	m	[0.1,0.32]	0.274
z_c	m	[0.3,0.7]	0.7
f_1	NA	NA	-119
f_2	NA	NA	-15.166

Table 5.3.4 Fall/Spring optimization.

Parameters	Unit	Range	Values
d_1, d_2	m	[0.1,0.32]	0.147
d_3	m	[0.1,0.32]	0.273
z_c	m	[0.3,0.7]	0.694
f_1	NA	NA	-97
f_2	NA	NA	-15.478

Table 5.3.5 Summer optimization.

Parameters	Unit	Range	Values
d_1, d_2	m	[0.1,0.32]	0.173
d_3	m	[0.1,0.32]	0.279
z_c	m	[0.3,0.7]	0.654
f_1	NA	NA	-116
f_2	NA	NA	-15.604

Seasonal adaption reaches an optimized result with largest workspace and the largest general stiffness with this workspace. The eligible reachable workspace by the platform for each season, and the general stiffness mapping over the workspace are given in figure 5.3.5.
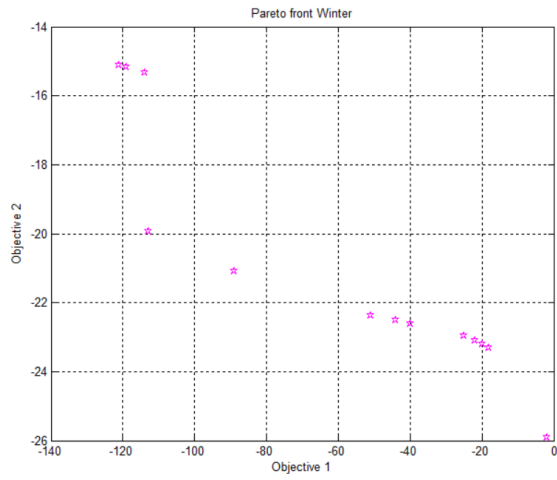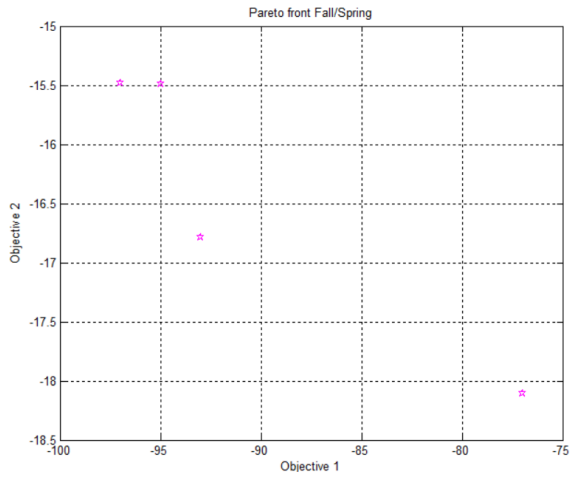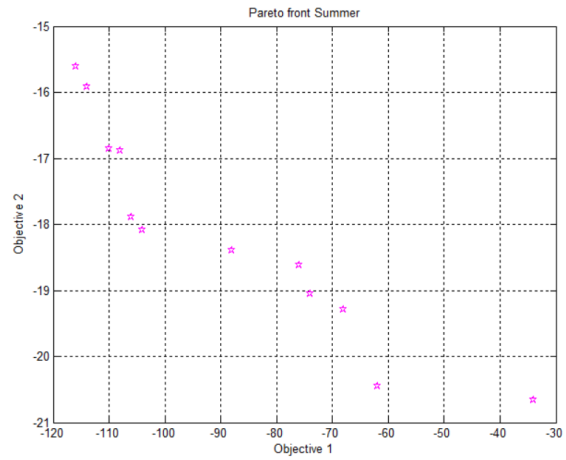
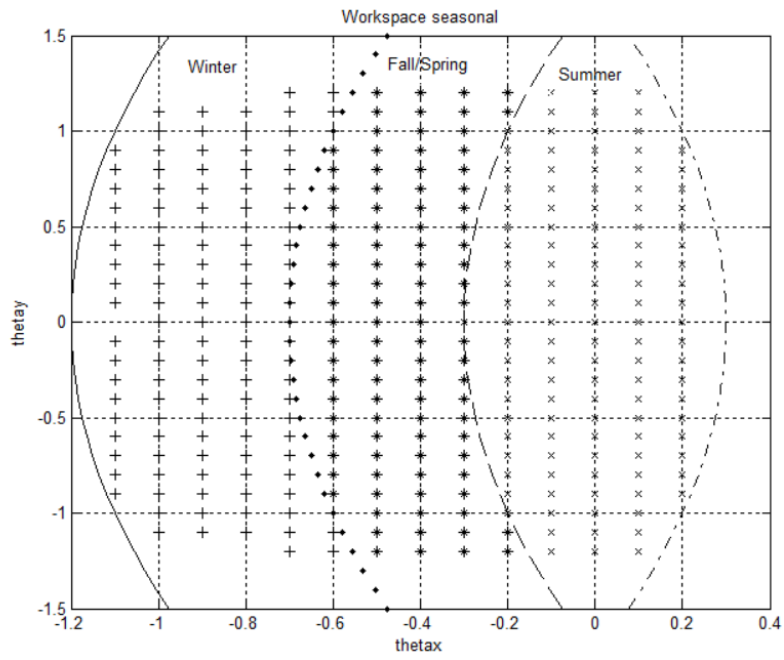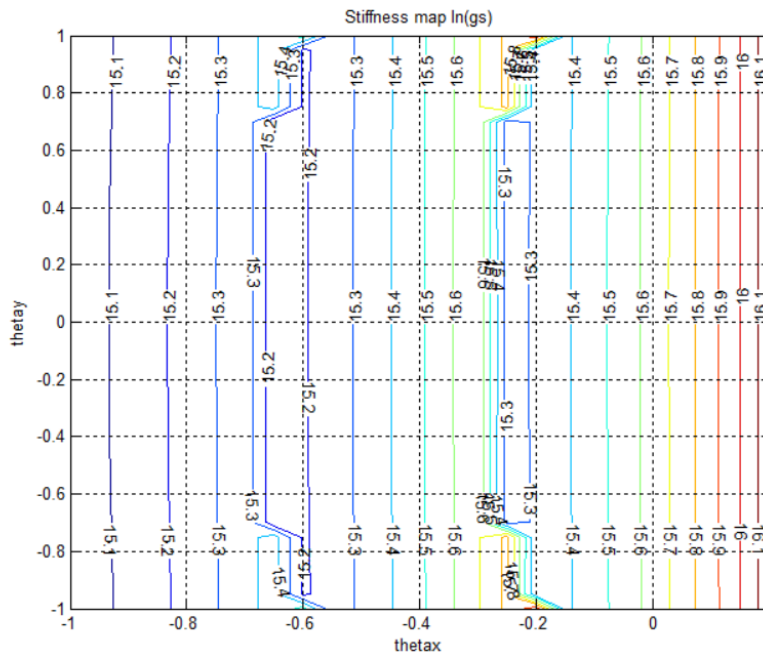Figure 5.3.4 Optimization using pareto front. (a) winter; (b) fall/spring; (c) summer.

(a)

(b)

courtesy of ASME

Figure 5.3.5 Optimization results display. (a) workspace; (b) stiffness.

In a same season, the centre of mass of platform is at constant height, so to keep the platform height from being fluctuating to save the energy.

5.3.4 Section Conclusion

The solar tracking stand in parallel 3-$\underline{P}$RS has a pre-optimization to the guide the setting of design parameters, and a separate two-objective optimization that deals with operational objectives in selected areas for workspace and general stiffness. This design has advantage of high general stiffness and easy maintenance including a protection pose that allows it to lie flat on ground during destructive storms. The parallel stand can be adjusted with regards to seasons. Best workspace and stiffness are sought as season changes. Optimizing the objectives by season provides a better performance than any fixed configuration. This is an important advantage of the adaptive solar tracking stand, which contributes to solar energy collection, a source of clean and free energy.

This is a concept design. One needs to consider the displacement limits of real actuators, dust proof requirements in the fields. The inclination rail has three jointed points thus it is subject to bending. Next section will discuss adaptive 3-R$\underline{P}$S design fulfilling these requirements.

5.4 Adaptive 3-R$\underline{P}$S Parallel Manipulator

This section presents the robotic structure and analysis of a hybrid energy harvester designed in the form of a structural adaptive 3-R$\underline{P}$S parallel manipulator, which tracks and collects solar energy as a main function and also harvests energy from wind loads on the large solar panel. The adaptive

design allows the harvester to lie flat on floor when destructive storms occur and then return to a working configuration after the storms. The workspace of the manipulator is determined by a minimum platform height algorithm that is developed to find all reachable positions that compose the workspace and also bring bending at root to least. The stiffness mapping of the harvester is significant in evaluating its capacity to take wind loads, which a transformation matrix is developed to convert to polar horizontal stiffness at end effector that is crucial to the intelligent control strategy in decision to enter lie-flat configuration.

5.4.1 The 3-RPS Mechanism Design

This tracking stand is a 3-RPS parallel manipulator with lie-flat and working configuration features.

The orientation angle and height of the solar panel could be adjusted by three actuated legs which are jointed to motor-driven adjustable bases. The structure can be written in full as 3-PRPS.

As to meet the dust-proof, load capacity and geometric requirements for out-door working conditions, the linear tables (model: Alpha 15-B-155) [157] and the linear actuators (model: DLA-12-40-311-200-IP65) [158] are selected to function as adjustable base locations and telescopic legs respectively. The spherical joint with large motion range [135] and piezo-chips incorporated parallel structures are considered. Figure 5.4.1 shows the design in two configurations.
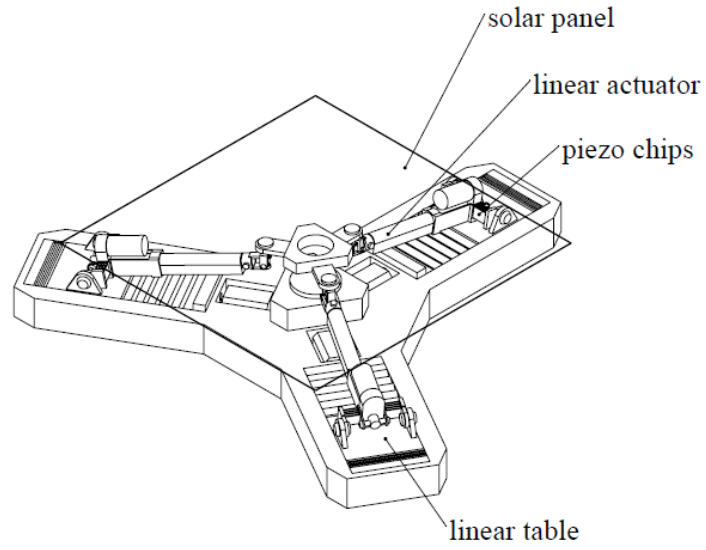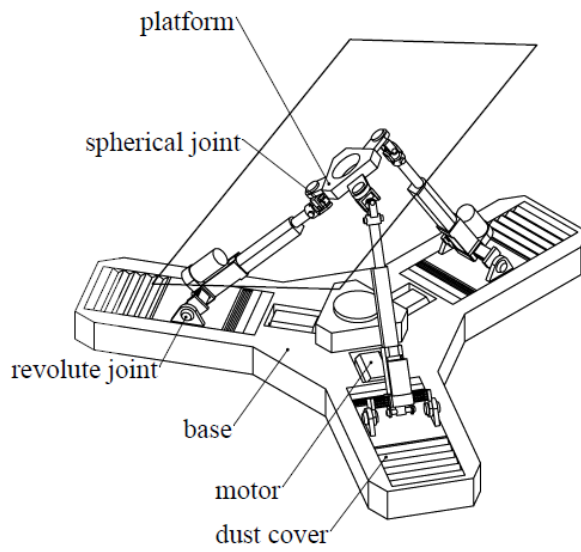
Figure 5.4.1 The hybrid harvester. (a) lie-flat configuration; (b) working configuration.

5.4.2 Inverse Kinematics and Stiffness

The inverse kinematics solves for the actuation displacements from a given posture of the platform.

In figure 5.4.2, the plane A represents the floor and the plane B represents a parallel plane above floor. The global coordinate system $A_o - X_o Y_o Z_o$ is located at A_o underneath B_o by h_b.

$$X_o = [1 \quad 0 \quad 0]^T; Y_o = [0 \quad 1 \quad 0]^T; Z_o = [0 \quad 0 \quad 1]^T \tag{5.4.1}$$
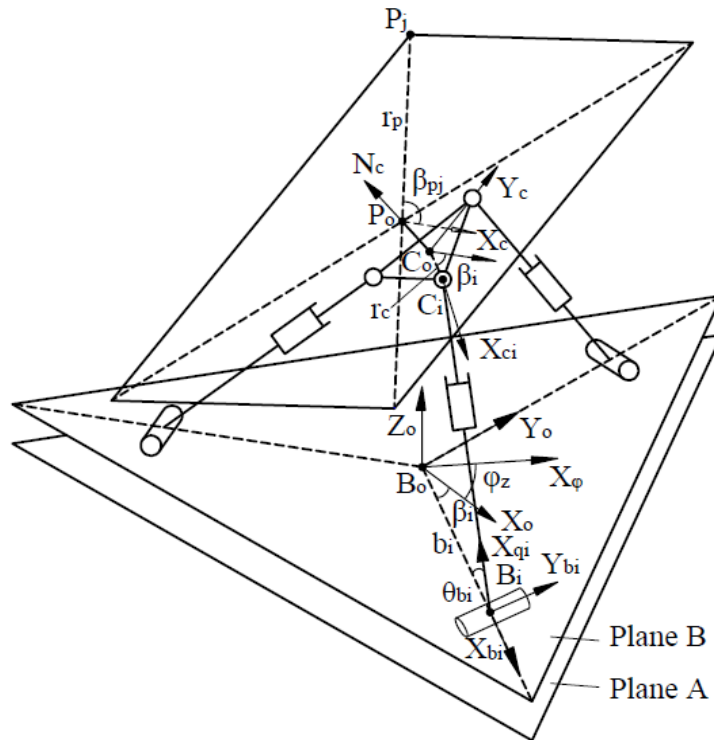
$$A_o = [0 \quad 0 \quad 0]^T; B_o = A_o + h_b Z_o \tag{5.4.2}$$

Figure 5.4.2 Inverse kinematic parallel structure.

Three points B_1, B_2, and B_3 are located on plane B where revolute joints are. One can connect lines B_oB_i, and finds angle β_i between X_o and B_oB_i. The length of B_oB_i is b_i which can be adjusted by base joint relocation. Sub-coordinates $B_i - X_{bi}Y_{bi}Z_o$ are established at B_1, B_2, and B_3.

$$X_{bi} = Q_iX_o \ ; \ Y_{bi} = Q_iY_o; \text{where } Q_i = \begin{bmatrix} \cos\beta_i & -\sin\beta_i & 0 \\ \sin\beta_i & \cos\beta_i & 0 \\ 0 & 0 & 1 \end{bmatrix} \quad i = 1,2,3 \qquad (5.4.3)$$

The platform is a triangle with C_o at the center, while points C_1, C_2, and C_3 are at the three vertices of the triangle where spherical joints are. One can connect lines C_oC_i, the length of C_oC_i is a fixed value r_c. One can set a sub-coordinate $C_o - X_cY_cN_c$ at C_o, where Y_c aligns with vector C_oC_1, X_c lies on the triangle plane, and N_c be a unit vector normal to the platform. The angle β_i is between X_c and C_oC_i.

A square solar panel is attached above the platform by h_p in N_c direction. The four points P_1, P_2, P_3 and P_4 are at the four points of the solar panel square. One can connect lines P_oP_j, which forms an angle β_{pj} from X_c, and the length of the lines is a fixed value r_p.

The vectors C_oC_i and P_oP_j from the perspective of coordinate $C_o - X_cY_cN_c$ are given below.

$$R_{ci} = [r_c \cdot \cos\beta_i \quad r_c \cdot \sin\beta_i \quad 0]^T, i = 1,2,3 \qquad (5.4.4.a)$$

$$R_{pj} = [r_p \cdot \cos\beta_{pj} \quad r_p \cdot \sin\beta_{pj} \quad 0]^T, j = 1,2,3,4 \qquad (5.4.4.b)$$

One can connect B_iC_i along which the prismatic joints are, the length of which is $q_i \in [q_{min}, q_{max}]$, and a unit vector X_{qi} is set along B_iC_i. Vector X_{qi} forms an angle θ_{bi} above the plane B. In order to make sure that linear actuators operate under the moving platform, an angular

constraint γ_{cm} is set which is the minimum angle the vector $\boldsymbol{X_{qi}}$ can form to platform plane ($C_o - C_1C_2C_3$).

Relocation of the $\boldsymbol{B_i}$ along $\boldsymbol{X_{bi}}$ introduces an adjustment variable b_{i-adj}. When $b_{i-adj} = 0$, variable b_i is determined to allow minimum height of platform at the lie-flat posture.
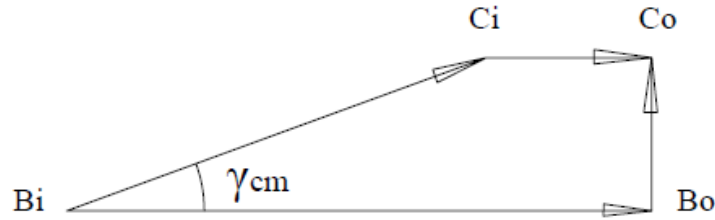
Figure 5.4.3 Lie-flat vectors diagram.

The lie-flat vector diagram is shown in figure 5.4.3. It determines the height of the lie-flat pose.

$$\boldsymbol{B_i} = b_i \boldsymbol{Q_i} \boldsymbol{X_o} + \boldsymbol{B_o}, \text{ where } b_i = q_{min}\cos\gamma_{cm} + r_c + b_{i-adj} \qquad (5.4.5)$$

Rotational matrix needs platform rotation variables θ_x and θ_y around $\boldsymbol{X_o}$ and $\boldsymbol{Y_o}$ to convert vectors or matrix in $C_o - X_cY_cN_c$ to that in $B_o - X_oY_oZ_o$.

$$u_x = \frac{\theta_x}{\theta} \text{ and } u_y = \frac{\theta_y}{\theta}, \text{ where } \theta = \sqrt{\theta_x{}^2 + \theta_y{}^2} \qquad (5.4.6.a)$$

$$R = \begin{bmatrix} c\theta + u_x^2(1 - c\theta) & u_x u_y(1 - c\theta) & u_y \, s\theta \\ u_x u_y(1 - c\theta) & c\theta + u_y^2(1 - c\theta) & -u_x \, s\theta \\ -u_y \, s\theta & u_x \, s\theta & c\theta \end{bmatrix} \qquad (5.4.6.b)$$

One can set $C_o = [x_c \quad y_c \quad z_c]^T$ as its position in global coordinate. As B_i is a revolute joint, then $B_o C_i$ is perpendicular to Y_{bi}, which is a relationship to find kinematic solutions for x_c and y_c.

So that,

$$C = \begin{bmatrix} Y_{b2} \cdot X_o & Y_{b2} \cdot Y_o \\ Y_{b3} \cdot X_o & Y_{b3} \cdot Y_o \end{bmatrix}^{-1} \cdot \begin{bmatrix} RR_{c2} \cdot Y_{b2} \\ RR_{c3} \cdot Y_{b3} \end{bmatrix} \qquad (5.4.7.a)$$

which satisfies,

$$(RR_{ci} + C_o) \cdot Y_{bi} = 0 \qquad (5.4.7.b)$$

$$x_c = C \cdot X_o; \; y_c = C \cdot Y_o \qquad (5.4.7.c)$$

The variable z_c is usually given by the motion planner, however improper selection of this value can result to invalid solution. In this section, an algorithm is explained that seeks the minimum height of platform center C_o, z_c, if an eligible solution exists. This algorithm avoids missing valid solutions while keeping minimum solar panel height to mitigate the wind loads bending effects at structure root.

The minimum height algorithm starts by setting the initial value z_{co}.

$$C_o{}^* = [x_c \quad y_c \quad z_{co}]^T \text{ , where } z_{co} = 0 \qquad (5.4.8.a)$$

$$C_i{}^* = RR_{ci} + C_o{}^*; \; P_o{}^* = h_p RZ_o + C_o{}^*; \; P_j{}^* = RR_{pj} + P_o{}^* \qquad (5.4.8.b)$$

In figure 5.4.4, possible candidates of z_c are calculated by determining an offset as a supplement to z_{co}. The offsets are determined considering some criteria. Offset 1: none of $\boldsymbol{P_j}$ point should stay below plane B; Offset 2: an angular constraint γ_{cm} is met which is the minimum angle the leg can form to platform plane $(C_o - C_1C_2C_3)$ under this platform; Offset 3: none of q_i should be less than q_{min}.

Offset 1, d_{o1}:

$$d_{o1} = h_b - z_{pi-min}, \text{ where } z_{pi-min} = min\ (\boldsymbol{P_i} \cdot \boldsymbol{Z_o}) \qquad (5.4.9.\text{a})$$

$$z_{c-can1} = z_{co} + d_{o1} \qquad (5.4.9.\text{b})$$

Offset2, d_{o2}:

A unit vector $\boldsymbol{X_{ci}}$ is along the intersection line of planes $C_o - C_1C_2C_3$ and $X_{bi} - B_i - Z_o$.

$$\boldsymbol{X_{ci}} = \frac{\boldsymbol{Y_{bi}} \times \boldsymbol{N_c}}{|\boldsymbol{Y_{bi}} \times \boldsymbol{N_c}|}, \text{ where } \boldsymbol{N_c} = \boldsymbol{RZ_o} \qquad (5.4.10.\text{a})$$

θ_{ci} is an acute angle between planes $C_o - C_1C_2C_3$ and $X_{bi} - B_i - Z_o$.

$$\theta_{ci} = \cos^{-1}|\boldsymbol{N_c} \cdot \boldsymbol{Y_{bi}}| \qquad (5.4.10.\text{b})$$

It is imagined that $\boldsymbol{X_{ci}}$ is rotated at $\boldsymbol{C_i}$ with an acute angle γ_{ci} about $\boldsymbol{Y_{bi}}$ to be altered to a new unit vector $\boldsymbol{X_{\gamma i}}$ which forms an angle γ_{cm} to the platform plane $C_o - C_1C_2C_3$ or to its projection on the platform in $\boldsymbol{N_c}$ direction. The arrowhead of $\boldsymbol{X_{\gamma i}}$ falls on a plane $(C_o - C_1C_2C_3)'$ that is parallel to platform plane and $\boldsymbol{X_{\gamma i}}$ is in plane $X_{bi} - B_i - Z_o$. The gap between planes $(C_o - C_1C_2C_3)'$ and

$C_o - C_1 C_2 C_3$ is certain, and the intersection lines they make on plane $X_{bi} - B_i - Z_o$ are parallel and the gap between which can be determined with θ_{ci}.

$$X_{\gamma i} = Q_i \begin{bmatrix} \cos \gamma_{ci} & 0 & \sin \gamma_{ci} \\ 0 & 1 & 0 \\ -\sin \gamma_{ci} & 0 & \cos \gamma_{ci} \end{bmatrix} Q_i^{-1} X_{ci}, \text{ where } \gamma_{ci} = \sin^{-1} \frac{\sin \gamma_{cm}}{\sin \theta_{ci}} \qquad (5.4.10.\text{c})$$

If $C_i B_i$ is along $X_{\gamma i}$, the length of $C_i B_i$ for it to reach B_i is $q_{i-\gamma cm}$.

With $X_{\gamma i}$, $q_{i-\gamma cm}$ and C_i^*, one can find an imagined point $B_{\gamma i}$ whose global coordinate in Z_o is z_{bi-c}.

$$z_{bi-c} = \left(q_{i-\gamma cm} X_{qi} + C_i^* \right) \cdot Z_o, \text{ where } q_{i-\gamma cm} = \frac{(B_i - C_i^*) \cdot X_{bi}}{X_{\gamma i} \cdot X_{bi}} \qquad (5.4.10.\text{d})$$

Three legs each has its $B_{\gamma i}$ height, z_{bi-c}, and the minimum among them is selected so that an offset is calculated based on the lowest $B_{\gamma i}$, thus the other two legs will be satisfied with the offset lift.

$$d_{o2} = h_b - z_{bi-c-min}, \text{ where } z_{bi-c-min} = \min(z_{bi-c}) \qquad (5.4.10.\text{e})$$

$$z_{c-can2} = z_{co} + d_{o2} \qquad (5.4.10.\text{f})$$

Offset 3, d_{o3}:

With C_i^* and q_{min}, one can find an imagined B_{qi} under B_i which ensures the minimum length of linear actuators be met in all legs. The global coordinate of B_{qi} in Z_o is z_{bi-q}.

$$z_{bi-q} = C_i^* \cdot Z_o - \sqrt{q_{min}^2 - \left((B_i - C_i^*) \cdot X_{bi} \right)^2} \qquad (5.4.11.\text{a})$$

Three legs each has its $\boldsymbol{B_{qi}}$ height, z_{bi-q}, and the minimum among them is selected so that an offset is calculated based on the lowest $\boldsymbol{B_{qi}}$ and the other two legs will be satisfied with the offset lift.

$$d_{o3} = h_b - z_{bi-q-min}, \text{ where } z_{bi-q-min} = \min(z_{bi-q}) \tag{5.4.11.b}$$

$$z_{c-can3} = z_{co} + d_{o3} \tag{5.4.11.c}$$

There are three z_c candidates, each is the minimum height requirement in its offset calculation that means it may have room to be enlarged. The maximum of the candidates is selected so that the other two offset requirements are included under it.

$$z_c = \max(z_{c-can\text{k}}), \text{k} = 1,23 \tag{5.4.12}$$

Once z_c is determined, the posture needs to be calculated again with updated values.

$$\boldsymbol{C_o} = [x_c \quad y_c \quad z_c]^T \tag{5.4.13.a}$$

$$\boldsymbol{C_i} = \boldsymbol{RR_{ci}} + \boldsymbol{C_o}; \boldsymbol{P_o} = h_p\boldsymbol{RZ_o} + \boldsymbol{C_o}; \boldsymbol{P_j} = \boldsymbol{RR_{pj}} + \boldsymbol{P_o} \tag{5.4.13.b}$$

The motion of linear actuations are calculated based on the above platform position.

$$\boldsymbol{q_i} = |\boldsymbol{B_i} - \boldsymbol{C_i}| \text{ and } \theta_{bi} = \tan^{-1}\frac{(\boldsymbol{C_i}-\boldsymbol{B_i})\cdot\boldsymbol{Z_o}}{(\boldsymbol{B_i}-\boldsymbol{C_i})\cdot\boldsymbol{X_{bi}}} \tag{5.4.14}$$

The updated value of z_c will need to be verified. The posture with updated z_c need to meet a criteria that none of the linear actuators q_i extends q_{max}, fully extended size.

Within n_r pairs of (θ_x, θ_y), program loops calculate z_c at each (θ_x, θ_y) and then verify. The number of eligible solutions n_e is an index to evaluate the workspace.
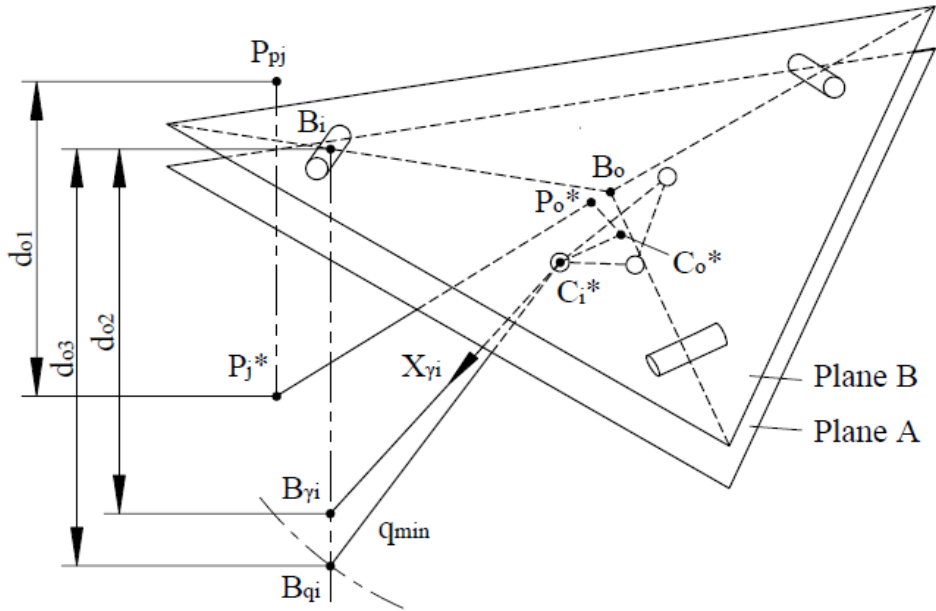
Figure 5.4.4 Minimum platform height z_c.

The 3-R$\underline{P}$S manipulator has 3 DOF, that means it has three independent motions, while the other motions in space are compliant to the independent motions.

In the global coordinate, the linear and angular velocities system of the end effector, center of the platform C_o, is given below.

$$V_{co} = [\partial x_c \quad \partial y_c \quad \partial z_c]^T \text{ and } \boldsymbol{\omega}_{co} = [\partial \theta_{cx} \quad \partial \theta_{cy} \quad \partial \theta_{cz}]^T \qquad (5.4.15)$$

Only three of six space motion variables are independent. The variables have a relationship as below.

105

$$Y_{bi} \cdot V_{ci} = 0, \text{ where } V_{ci} = V_{co} + \omega_{co} \times RR_{ci} \qquad (5.4.16.a)$$

$$C_v V_{co} + C_w \omega_{co} = 0, \text{ where } C_v = [Y_{b1} \quad Y_{b2} \quad Y_{b3}]^T \text{ and } C_w = \begin{bmatrix} [RR_{c1} \times Y_{b1}]^T \\ [RR_{c2} \times Y_{b2}]^T \\ [RR_{c3} \times Y_{b3}]^T \end{bmatrix} \qquad (5.4.16.b)$$

$$\omega_{co} = -C_w^{-1} C_v V_{co} \qquad (5.4.16.c)$$

And the methods in [91] and [92] suggests to eliminate the compliant motion by dot multiplying a vector perpendicular to the compliant motions on both sides of the equation.

$$V_{qi} + \omega_{qi} Y_{bi} \times (C_i - B_i) = V_{ci} \qquad (5.4.17.a)$$

$$(C_i - B_i) \cdot V_{qi} + 0 = (C_i - B_i) \cdot V_{ci} \qquad (5.4.17.b)$$

where,

$$V_{qi} = \frac{(C_i - B_i)}{|C_i - B_i|} \partial q_i = X_{qi} \partial q_i \qquad (5.4.17.c)$$

Rearrange the above, one has the following.

$$(C_i - B_i) \cdot \frac{(C_i - B_i)}{|C_i - B_i|} \partial q_i = (C_i - B_i) \cdot (V_{co} + \omega_{co} \times RR_{ci}) \qquad (5.4.18.a)$$

$$q_i X_{qi}{}^2 \partial q_i = q_i X_{qi} \cdot (V_{co} + \omega_{co} \times RR_{ci}) \qquad (5.4.18.b)$$

$$X_{qi}{}^2 = 1 \qquad (5.4.18.c)$$

$$q_i \partial q_i = q_i X_{qi} \cdot (V_{co} - C_w^{-1} C_v V_{co} \times RR_{ci}) \qquad (5.4.18.d)$$

$$\partial q_i = X_{qi} \cdot (V_{co} - C_w^{-1} C_v V_{co} \times RR_{ci}) \qquad (15.4.18.e)$$

$$\partial q_i = X_{qi} \cdot V_{co} - X_{qi} \cdot (C_w^{-1} C_v V_{co}) \times (RR_{ci}) \qquad (5.4.18.f)$$

106

$$\partial q_i = \boldsymbol{X_{qi}} \cdot \boldsymbol{V_{co}} + \boldsymbol{X_{qi}} \cdot (\boldsymbol{RR_{ci}}) \times \left(\boldsymbol{C_w}^{-1}\, \boldsymbol{C_v V_{co}}\right) \tag{5.4.18.g}$$

$$\partial q_i = \boldsymbol{X_{qi}} \cdot \boldsymbol{V_{co}} + \boldsymbol{X_{qi}} \times \boldsymbol{RR_{ci}} \cdot \boldsymbol{C_w}^{-1} \boldsymbol{C_v V_{co}} \tag{5.4.18.h}$$

$$\partial q_i = \boldsymbol{X_{qi}}^T \cdot \boldsymbol{V_{co}} + \left(\boldsymbol{X_{qi}} \times \boldsymbol{RR_{ci}}\right)^T \cdot \left(\boldsymbol{C_w}^{-1}\, \boldsymbol{C_v}\right) \cdot \boldsymbol{V_{co}} \tag{5.4.18.i}$$

$$\partial q_i = \left(\boldsymbol{X_{qi}}^T + \left(\boldsymbol{X_{qi}} \times \boldsymbol{RR_{ci}}\right)^T \cdot \left(\boldsymbol{C_w}^{-1}\, \boldsymbol{C_v}\right)\right) \cdot \boldsymbol{V_{co}} \tag{5.4.18.j}$$

$$\boldsymbol{J_{ri}} = \left(\boldsymbol{X_{qi}} + \boldsymbol{X_{qi}} \times \boldsymbol{RR_{ci}}\right)^T \cdot \left(\boldsymbol{C_w}^{-1}\, \boldsymbol{C_v}\right) \tag{5.4.18.k}$$

$$\partial q_i = \boldsymbol{J_{ri}} \cdot \boldsymbol{V_{co}} \tag{5.4.18.l}$$

The Jacobian matrix is obtained as below.

$$\boldsymbol{J} = [\boldsymbol{J_{r1}} \quad \boldsymbol{J_{r2}} \quad \boldsymbol{J_{r3}}]^T \tag{5.4.19.a}$$

This reflects the relationship between actuation velocities and the end effector velocities.

$$[\partial q_1 \quad \partial q_2 \quad \partial q_3]^T = \boldsymbol{J}[\partial x_c \quad \partial y_c \quad \partial z_c]^T \tag{5.4.19.b}$$

Stiffness of end effector $\boldsymbol{K_c}$ is expressed as below, where $\boldsymbol{K_q}$ is the actuation stiffness.

$$\boldsymbol{K_c} = \boldsymbol{J}^T \boldsymbol{K_q} \boldsymbol{J} \text{ , where } \boldsymbol{K_q} = \begin{bmatrix} k_{q1} & 0 & 0 \\ 0 & k_{q2} & 0 \\ 0 & 0 & k_{q3} \end{bmatrix} \tag{5.4.20}$$

The stiffness along $\boldsymbol{X_o}$, $\boldsymbol{Y_o}$ and $\boldsymbol{Z_o}$ are given.

$$k_x = (\boldsymbol{K_c X_o})^T \cdot \boldsymbol{X_o}; \; k_y = (\boldsymbol{K_c Y_o})^T \cdot \boldsymbol{Y_o}; \; k_z = (\boldsymbol{K_c Z_o})^T \cdot \boldsymbol{Z_o} \tag{5.4.21}$$

When $\boldsymbol{X_o}$ rotates around $\boldsymbol{Z_o}$ by φ_z, it forms a new vector $\boldsymbol{X_\varphi}$. The vector $\boldsymbol{X_o}$ expressed in coordinate

with $\boldsymbol{X_\varphi}$ is given below.

$$(X_o)_\varphi = R_z X_o \text{ , where } R_z = \begin{bmatrix} \cos(-\varphi_z) & -\sin(-\varphi_z) & 0 \\ \sin(-\varphi_z) & \cos(-\varphi_z) & 0 \\ 0 & 0 & 1 \end{bmatrix} \qquad (5.4.22.a)$$

The velocity vector $(V_{co})_\varphi$ represents the end effector velocity in coordinate with X_φ. It replaces velocity V_{co} with transformation matrix R_z^{-1}.

$$\text{As } V_{co} = R_z^{-1}(V_{co})_\varphi, \ \partial q_i = J_{ri} \cdot R_z^{-1}(V_{co})_\varphi \qquad (5.4.22.b)$$

where,

$$R_z^{-1} = \begin{bmatrix} \cos\varphi_z & -\sin\varphi_z & 0 \\ \sin\varphi_z & \cos\varphi_z & 0 \\ 0 & 0 & 1 \end{bmatrix} \qquad (5.4.22.c)$$

This provides a new Jacobian matrix with a rotation angle index of φ_z.

$$J_{\varphi i} = J_{ri} R_z^{-1}, \text{ so that } J_\varphi = [J_{\varphi 1} \quad J_{\varphi 2} \quad J_{\varphi 3}]^T \qquad (5.4.22.d)$$

The stiffness $k_{x\varphi}$ along X_φ could be calculated.

$$K_\varphi = J_\varphi{}^T K_q J_\varphi \qquad (5.4.22.e)$$

$$k_{x\varphi} = (K_\varphi X_o)^T \cdot X_o \qquad (5.4.22.f)$$

The leg $B_i C_i$ has the longitudinal stiffness k_q which has two components in series, linear actuator stiffness k_a and eight parallel piezo chips stiffness each with k_p.

$$\frac{1}{k_q} = \frac{1}{8 \cdot k_p} + \frac{1}{k_a}, i = 1,2,3 \qquad (5.4.23)$$

The force exerted along the linear actuator is F_{qi}, and the reaction force at each revolute joint side is R_{qi}.

$$F_{qi} = 2R_{qi}, i = 1,2,3 \qquad (5.4.24.a)$$

Each piece of the chip takes a share of the load. Eight chips of each leg are connected in parallel, and each piece of the chip is seen as a cantilever [159]. Its stiffness is the ratio of load to deflection.

$$F = \frac{F_{qi}}{8} \qquad (5.4.24.b)$$

$$k_p = \frac{F}{d_{max}} \qquad (5.4.24.c)$$

The maximum deflection is expressed as below.

$$d_{max} = \frac{Fw^3}{3E_{pzt}I} \qquad (5.4.24.d)$$

where,

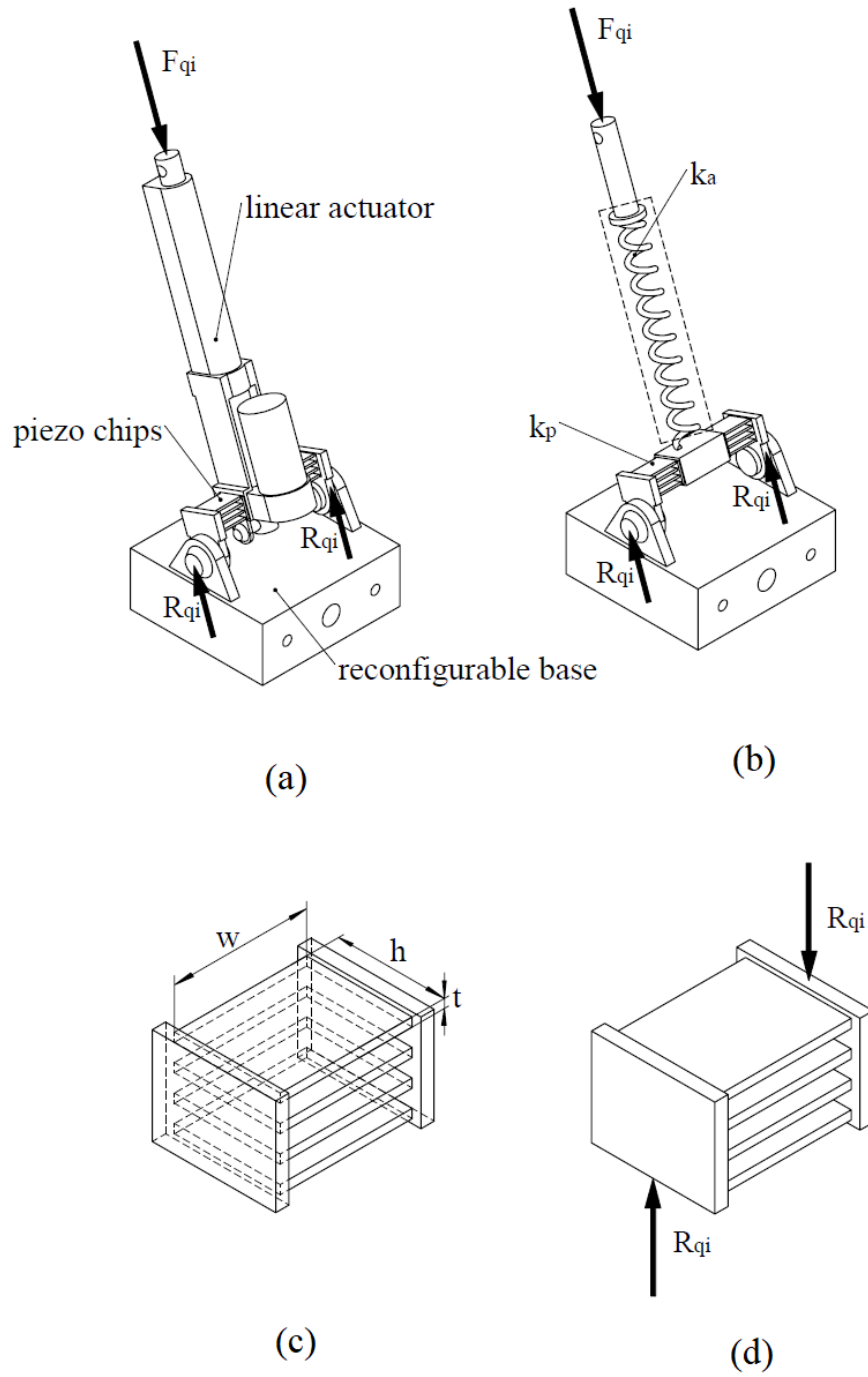$$I = \frac{t^3 h}{12} \qquad (5.4.24.e)$$

Figure 5.4.5 Leg stiffness. (a) loading and reaction forces; (b) elastic model; (c) Piezo chip size;

(d) loads on piezo chips.

5.4.3 Adaption and Operation Optimization

Based on real values of linear actuators and linear tables as selected from manufacturers, so that numerical analysis can be performed. The design parameters are shown in table 5.4.1.

Table 5.4.1 Design parameters.

Parameters	Units	Values
h_b	m	0.092
r_p	m	0.5
r_c	m	0.1
h_p	m	0.05
$[q_{min}, q_{max}]$	m	$[0.35, 0.55]$
$\beta_{i, \ (i=1,2,3)}$	rad	$\left[\frac{\pi}{2} \quad -\frac{\pi}{6} \quad \frac{7\pi}{6}\right]$
$\beta_{pj, \ (j=1,2,3,4)}$	rad	$\left[\frac{\pi}{4} \quad -\frac{\pi}{4} \quad -\frac{3\pi}{4} \quad \frac{3\pi}{4}\right]$
γ_{cm}	rad	0.1745

The original $\boldsymbol{B_i}$ locations allows the lie-flat configuration but provides a limited workspace. Genetic algorithm is implemented to find another configuration that enlarges workspace, known as working configuration. The adjustable design enables the switch between the two configurations.

The adjustments b_{i-adj} are the variables for the MATLAB optimization algorithm that seeks global minimum of fitness function f, while the ultimate aim is to enlarge the workspace index n_e. The optimization process and results are displayed in figure 5.4.6, figure 5.4.7, table 5.4.2 and table 5.4.3.

$$\mathbf{X} = [b_{1-adj} \ b_{2-adj} \ b_{3-adj}] \qquad (5.4.25.a)$$

$$f = -n_e \tag{5.4.25.b}$$
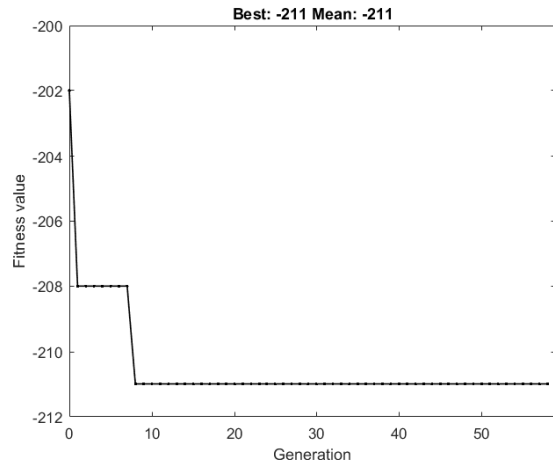
(a)
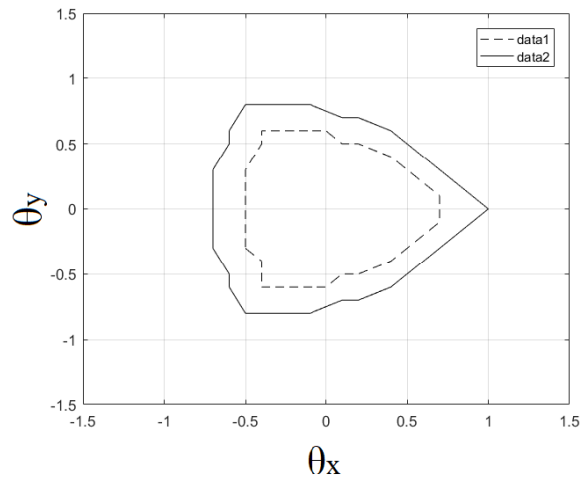
(b)

Figure 5.4.6 Optimization. (a) genetic algorithm for larger workspace; (b) workspace boundary,

dash: original; solid: optimized.
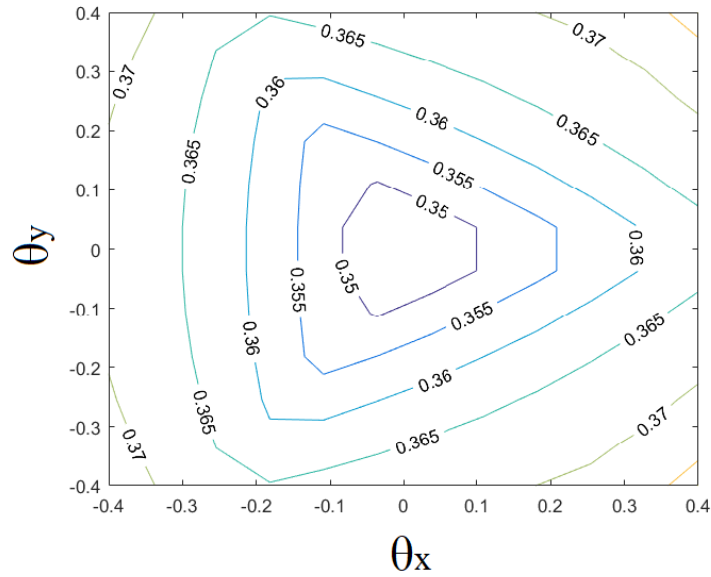
Figure 5.4.7 the z_c position mapping with optimized working configuration.

Table 5.4.2 Optimization parameters.

	Parameters	Units	Values
lower	X_{low}	m	$[-0.1 \quad -0.1 \quad -0.1]$
upper	X_{up}	m	$[0 \quad 0 \quad 0]$
search area	θ_x	rad	$-1.5: 0.1: 1.5$
search area	θ_y	rad	$-1.5: 0.1: 1.5$

Table 5.4.3 Optimization results.

	Variable **X**	$f = -n_e$
original	$[0\ 0\ 0]$	-126
optimized	$[-0.098 - 0.098 - 0.097]$	-211
rounded	$[-0.1 - 0.1 - 0.1]$	-211

113

The material Lead Zirconate Titanate (PZT) takes its Young's module E_{pzt} from [160]. The values are needed for stiffness calculation and plotting. Based on table 5.4.4, the value $k_{qi} = 4.9568 \times 10^5 \, N/m$.

Table 5.4.4 Stiffness parameters.

Parameters	Units	Values
k_a	N/m	5×10^5
E_{pzt}	Gpa	63
t	m	0.008
h	m	0.024
w	m	0.03

Figure 5.4.8. (a), (b) and (c) show the stiffness in directions along X_o, Y_o and Z_o. However the wind loads could be in any direction. As in figure 5.4.8. (d), for a certain configuration and posture of the manipulator, when φ_z varies within $0°\sim360°$, the stiffness $k_{x\varphi}$ with respect to φ_z could be visualized with a polar plot, which helps to evaluate the manipulator loading capacity to horizontal winds in specific horizontal directions.
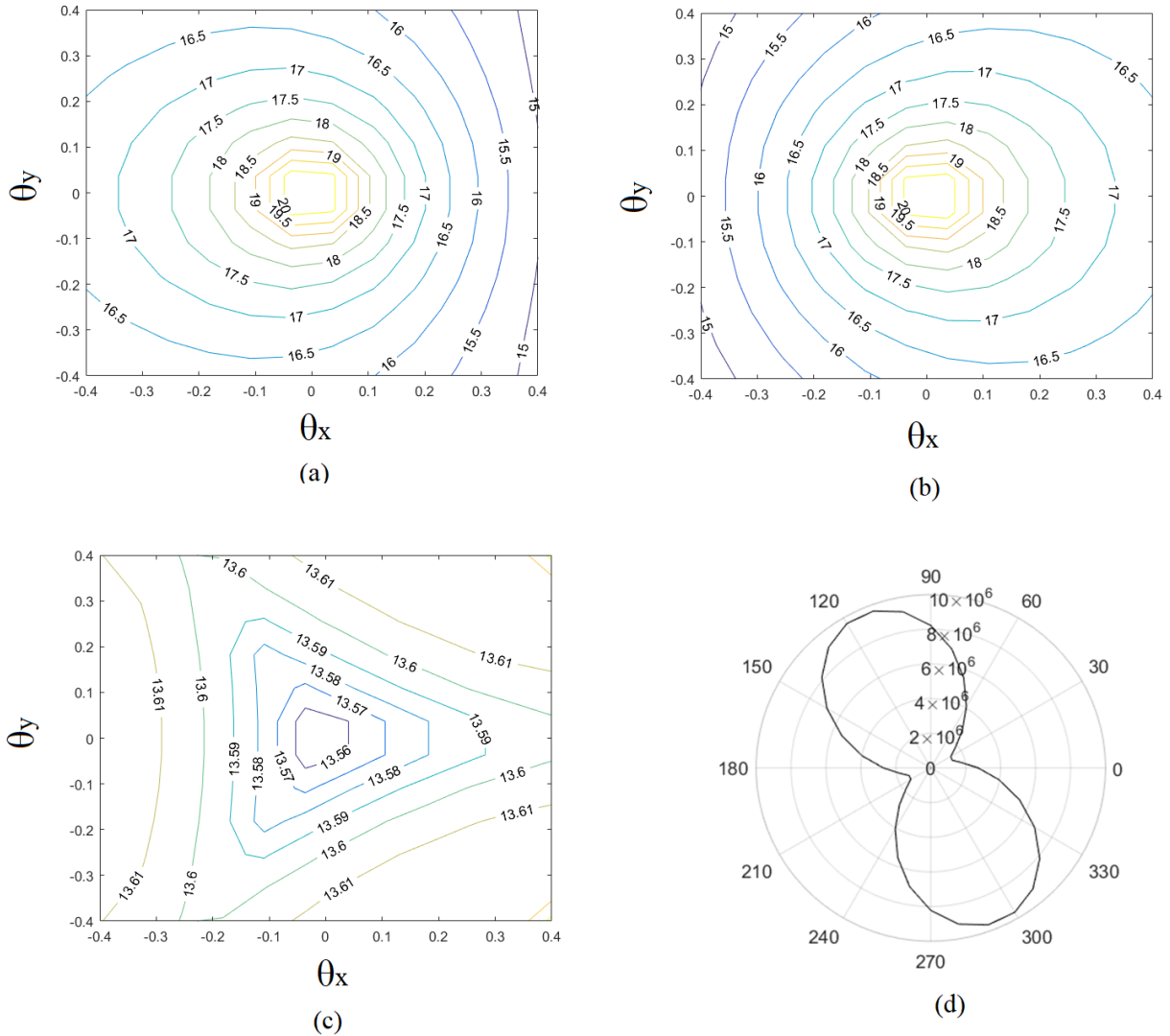
Figure 5.4.8 Stiffness mappings in prescribed motion range. (a) $\log(k_x)$ N/m; (b) $\log(k_y)$ N/m; (c) $\log(k_z)$ N/m; (d) stiffness $k_{x\varphi}$ polar plot about φ_z $\theta_x = 0.4$ and $\theta_y = -0.5$ at working configuration $X = [-0.1 - 0.1 - 0.1]$.

5.4.4 Section Conclusion

The design of a structural adaptive hybrid harvester enables 3-R$\underline{P}$S parallel solar tracker to collect solar and wind energy at the same time. This design has a lie-flat feature that protects the

manipulator from storms, and an enlarged workspace achieved by base joints relocation. This enables the manipulator to switch between the lie-flat configuration and the working configuration. Minimum platform height algorithm has been developed and demonstrated to find all eligible orientations of the platform. Stiffness mappings of the manipulator are plotted, after being converted to a polar plot, it assists to evaluate its capability to take wind loads in specific horizontal directions that is significant for lie-flat protection strategy against storms. The design adds favorable features to solar trackers that improves the energy collection efficiency and operational safety of the green industry.

5.5 Chapter Conclusion

This chapter discusses the re-design of 2R1T parallel mechanisms to be deployable structures in applications of the solar tracking. Two adaptive manipulators are designed.

The first 3-P̱RS parallel manipulator gives a concept of the deployable re-design, while the second 3-RP̱S parallel manipulator considers more practical requirements such as dust-proof requirements, rail loading condition and actuator installation sizes. The deformation of piezo chips in 3-RP̱S occurs as a kinematic redundancy which doesn't affect the end effector degree of freedom.

On the design and analysis, this chapter introduces the vector diagram method to determine the folded pose of the structure. It then develops minimum platform height algorithm and Jacobian matrix transformation to assist the design evaluation.

The optimization of the 3-PRS is multi-objective for purpose of specific operation, where both workspace and general stiffness in selected area are cost functions. (There is another pre-optimization that determines its basic design parameters for larger workspace).

The optimization of the 3-RPS is single-objective where only workspace is cost function. The adaption is involved in the operation optimization for large workspace at working configuration.

With the Jacobian transformation matrix developed in 3-RPS model, the 3-PRS model could also adopt this matrix as cost function to optimize the overall stiffness horizontally or in a specific direction seasonally.

The designs could also be considered for applications in radar signal receiver/tracker.

Chapter 6 Deployable Higher DOF Parallel Manipulators

6.1 Chapter Introduction

This chapter expands the deployable design to higher DOF mechanisms. A 6-DOF and a 5-DOF parallel manipulator with deployable function are designed and analyzed. The link interference problems are discussed in this chapter.

6.2 Theories and Methodologies

The manipulators are designed with the required DOF. According to the motion sets intersection, the motion of the end effector is the intersection of the limb motions. The limbs are in mobile vertical planes to be deployable, interference free and convenient for kinematic calculation. To avoid the motion limitation of spherical joints and to actuate the vertical planes with parallel actuation, an (2-$\underline{R}$R)UU 6-DOF limb is designed which is different from the (2-$\underline{R}$R)UU limb in [66] as the (2-$\underline{R}$R)UU limb hereby is in vertical planes perpendicular to the base, while the other (2-$\underline{R}$R)UU limb is equivalent to an (2-$\underline{R}$R)SR which is perpendicular to the moving platform.

The 6-DOF (2-$\underline{R}$R)UU hybrid limbs are in mobile vertical planes actuated on horizontal planes with parallel actuation instead of serial actuation. Parallel actuation evenly distributes loads and also reduces bending deformation by vertical loads. A 6-DOF limb doesn't constraint the end effector degrees of freedom. The 6-DOF manipulator has three identical 6-DOF (2-$\underline{R}$R)UU limbs, while the 5-DOF manipulator has two 6-DOF (2-$\underline{R}$R)UU limbs and a third limb of 5-DOF which reflect the DOF of the manipulator.

The limbs are arranged in vertical planes to avoid interference while the actuation links on horizontal plane need to be checked to be interference free. The links on horizontal plane are distributed to parallel layers to avoid interference, but in the same layer the links need to be checked for interference. Pentagon identification, point-line criteria and link boundary method have been developed to detect link to link interference.

Jacobian matrix is modified to reflect the stiffness in directions other than the global coordinate axes. It is also taken to verify the DOF of the novel structures developed in this chapter.

Multi objective optimization of workspace in different orientation of the platform are conducted where the folded height is among the objectives of the optimization.

6.3 Novel Design of 6-DOF 3T3R Parallel Mechanism

A novel 3-[(2-RR)UU] 6-DOF parallel manipulator is designed with limbs in mobile vertical planes, that provides larger workspace, less chance of link interference and simplified kinematic analysis. The link interference detection by pentagon identification and point-line criteria is demonstrated. Workspace is optimized by different orientations. The Jacobian matrix by global cartesian coordinate system is developed. A transformation matrix could convert that to Jacobian matrix of a new coordinate system.

6.3.1 The 3-[(2-RR)UU] Mechanism Design

The 3-RRUU parallel manipulator has 6 DOFs. Figure 6.3.1 shows (a) structure and (b) the kinematic chains represented by topology diagram [44] [45] with serial actuation. Figure 6.3.2

shows an equivalent structure but adopts parallel actuation which provides an even load distribution of the two actuators on one limb. Besides, the parallel actuation on horizontal plane forms a stronger cantilever than serial actuation. The latter is selected for the design.

A structure could also be expressed by a notation [48]. Therefore the structure is denoted as 3-[(2-$\underline{RR}$)UU], where underlined joints are actuated. Each limb has two motors $A_{[Api]}$ and $A_{[Aqi]}$ in hybrid chain. This increases the precision and reduces the bending of links $B_{[Bpi]}$, $B_{[Bqi]}$, $B_{[Cpi]}$ and $B_{[Cqi]}$. The revolute joints $\underline{R}_{[Api]}$ and $\underline{R}_{[Aqi]}$ are driven. The revolute joint $R_{[Ci]}$ connects to the universal joint $U_{[Di]}$ which consists two revolute joints and one of these is colinear to $R_{[Ci]}$.

The five bar planar mechanisms [161] are serving as the parallel actuation on horizontal plane for the mobile vertical planes.
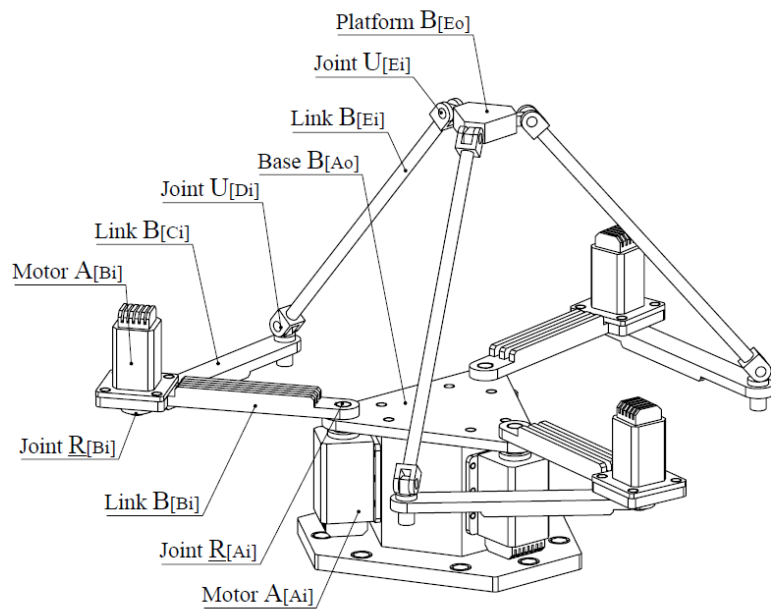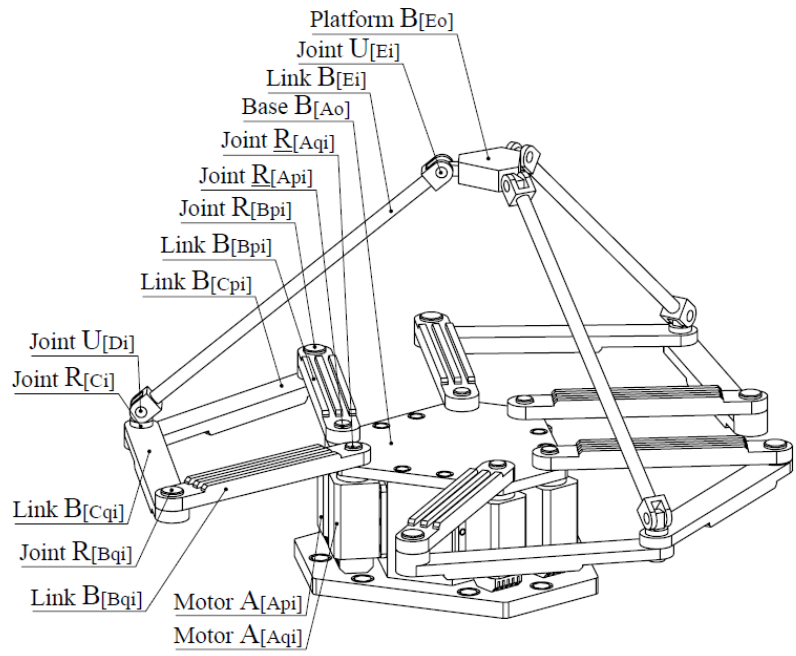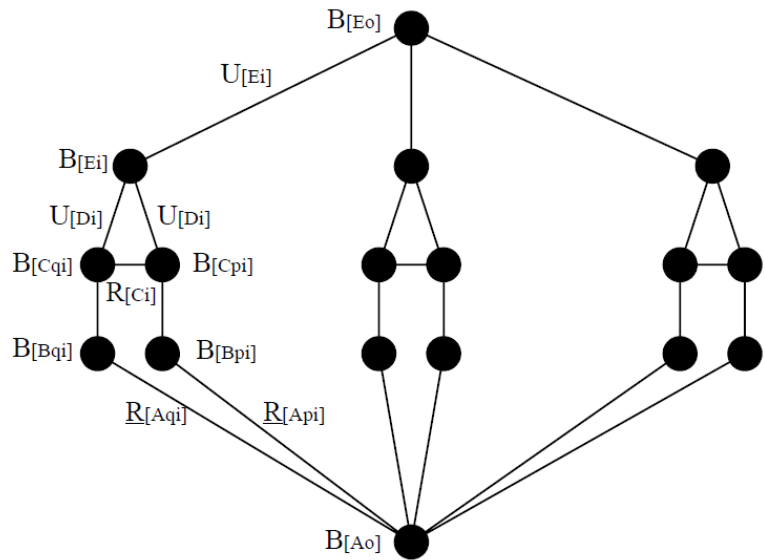
(a)
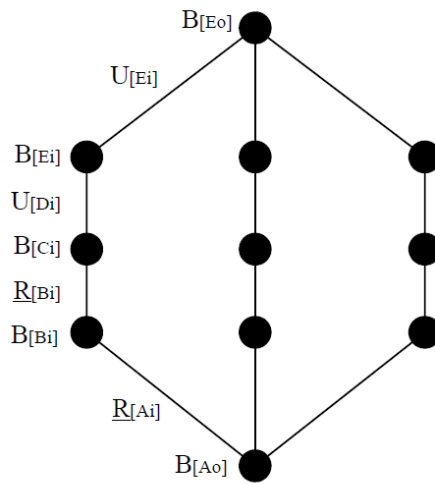
(b)

Figure 6.3.1 Serial actuation.

(a)

(b)

Figure 6.3.2 Parallel actuation.

6.3.2 Inverse Kinematics and Stiffness

Here gives the calculation of link positions, and detection of link interference.

The global cartesian coordinate is at base center A_o: $[0\ 0\ 0]^T$ (figure 6.3.3. (a)).

$$X_o = [1\ 0\ 0]^T, Y_o = [0\ 1\ 0]^T, Z_o = [0\ 0\ 1]^T \tag{6.3.1}$$

$$A_{pi} = r_b[\cos(\alpha_i - \beta)\ \ \sin(\alpha_i - \beta)\ \ 0]^T \tag{6.3.2.a}$$

$$A_{qi} = r_b[\cos(\alpha_i + \beta)\ \ \sin(\alpha_i + \beta)\ \ 0]^T \tag{6.3.2.b}$$

The pose of the moving platform (an equilateral triangle) is defined by its orientation $\boldsymbol{\theta_e}$ and position $\boldsymbol{E_o}$ from global coordinate.

$$\boldsymbol{\theta_e} = [\theta_x\ \ \theta_y\ \ \theta_z]^T \text{ and } \boldsymbol{E_o} = [x_e\ \ y_e\ \ z_e]^T \tag{6.3.3}$$

Let $\theta_e = \sqrt{\theta_x{}^2 + \theta_y{}^2 + \theta_z{}^2}$, so that $u_x = \theta_x/\theta_e$, $u_y = \theta_y/\theta_e$, $u_z = \theta_z/\theta_e$.

With orientation matrix R, the positions $\boldsymbol{E_i}$ are calculated, where the universal joints are located with one rotational axis along symmetry lines $\boldsymbol{E_i E_o}$ and the other rotational axis along $\boldsymbol{Y_{di}}$. The platform has a normal vector $\boldsymbol{N_e}$ that points upward.

$$R = \begin{bmatrix} c\,\theta_e + u_x{}^2(1 - c\,\theta_e) & u_x u_y(1 - c\,\theta_e) - u_z\,s\,\theta_e & u_x u_z(1 - c\,\theta_e) + u_y\,s\,\theta_e \\ u_x u_y(1 - c\,\theta_e) + u_z\,s\,\theta_e & c\,\theta_e + u_y{}^2(1 - c\,\theta_e) & u_y u_z(1 - c\,\theta_e) - u_x\,s\,\theta_e \\ u_x u_z(1 - c\,\theta_e) - u_y\,s\,\theta_e & u_y u_z(1 - c\,\theta_e) + u_x\,s\,\theta_e & c\,\theta_e + u_z{}^2(1 - c\,\theta_e) \end{bmatrix} \tag{6.3.4}$$

$$\boldsymbol{E_i} = R r_e[\cos(\alpha_i)\ \ \sin(\alpha_i)\ \ 0]^T + \boldsymbol{E_o} \tag{6.3.5}$$

$$\boldsymbol{N_e} = \frac{E_o E_1 \times E_o E_2}{|E_o E_1 \times E_o E_2|} \tag{6.3.6}$$

$$Y_{di} = \frac{Z_o \times E_o E_i}{|Z_o \times E_o E_i|} \quad \text{and} \quad X_{di} = Y_{di} \times Z_o \tag{6.3.7}$$
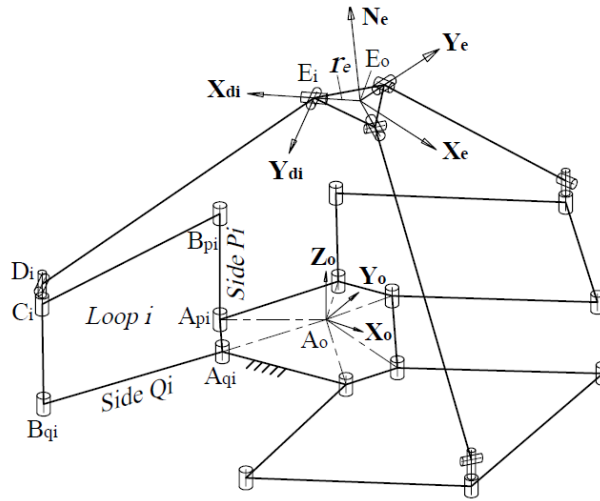
(a)
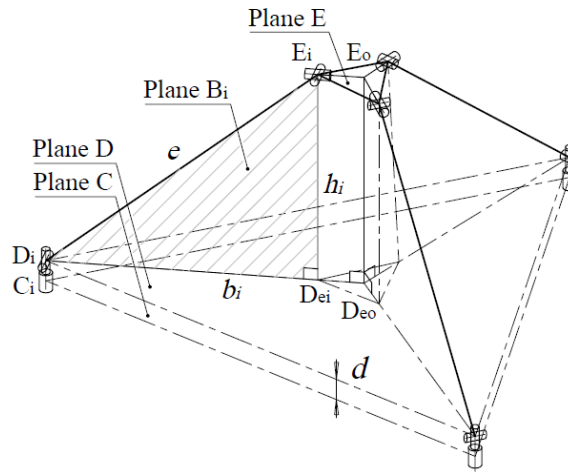
(b)

Figure 6.3.3 Kinematics analysis.

(a)

(b)

Figure 6.3.4 Horizontal plane.

As in figure 6.3.3. (b), the universal joints located at E_i and D_i each has a rotational axis along

Y_{di}. Links $E_i D_i$ and lines $E_i E_o$ lie in plane B_i which is perpendicular to horizontal plane C and

horizontal plane D. Let E_i be projected along $-Z_o$ on plane D at D_{ei}, where E_oD_{eo} is the intersecting line of plane B_1, plane B_2 and plane B_3. One obtains h_i and b_i in plane B_i.

$$h_i = E_i \cdot Z_o - d \tag{6.3.8.a}$$

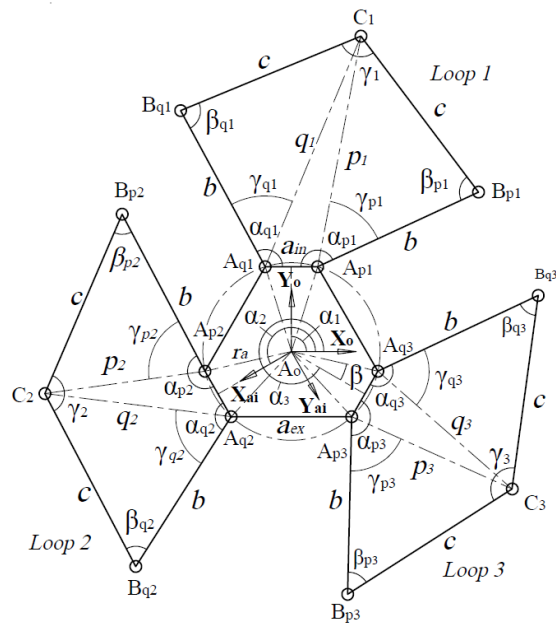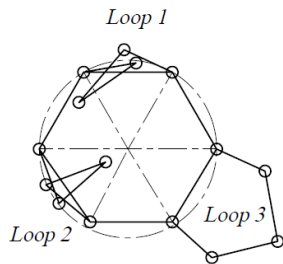$$b_i = \sqrt{e^2 - h_i{}^2} \tag{6.3.8.b}$$

Position D_i indicates where the universal joint is located. The universal joint has one rotational axis along Z_o and the other rotational axis along Y_{di}. As in figure 6.3.4. (a), let the five-bar mechanisms be in the plane C where the limbs are actuated. The position C_i indicates the location of revolute joint. The revolute joints rotate around Z_o, and colinear with the universal joints at D_i.

$$D_i = E_i + b_i X_{di} - h_i Z_o \tag{6.3.9}$$

$$C_i = D_i - dZ_o \tag{6.3.10}$$

The B_{pi} and B_{qi} represent the locations of two revolute joints, rotational axis along Z_o.

$$p_i = |A_{pi}C_i| \text{ and } q_i = |A_{qi}C_i| \tag{6.3.11.a}$$

$$\gamma_{pi} = \cos^{-1}\left(\frac{b^2+p_i{}^2-c^2}{2bp_i}\right) \text{ and } \gamma_{qi} = \cos^{-1}\left(\frac{b^2+q_i{}^2-c^2}{2bq_i}\right) \tag{6.3.11.b}$$

$$R_{pi} = \begin{bmatrix} \cos\gamma_{pi} & \sin\gamma_{pi} & 0 \\ -\sin\gamma_{pi} & \cos\gamma_{pi} & 0 \\ 0 & 0 & 1 \end{bmatrix} \text{ and } R_{qi} = \begin{bmatrix} \cos\gamma_{qi} & -\sin\gamma_{qi} & 0 \\ \sin\gamma_{qi} & \cos\gamma_{qi} & 0 \\ 0 & 0 & 1 \end{bmatrix} \tag{6.3.11.c}$$

$$B_{pi} = R_{pi}(A_{pi}C_i)\frac{b}{p_i} + A_{pi} \text{ and } B_{qi} = R_{qi}(A_{qi}C_i)\frac{b}{q_i} + A_{qi} \tag{6.3.11.d}$$

One could calculate actuation angles α_{pi} and α_{qi} by $A_{pi}B_{pi}$ or $A_{qi}B_{qi}$.

There are some literatures [68] [48] [126] [130] [162] discussing the link interference detection, where the main algorithm is to keep safe distance between links. One needs to check that three five-bar mechanisms have no link interference. The interference detection in this analysis has three sections.

Section 1 is to limit α_{pi} and α_{qi} ranges so that the moving sides of the link will not collide with the base arc of a neighboring link. Such as in figure 6.3.5. (a), the side of $\boldsymbol{A_{q1}B_{q1}}$ interferes with the arc of $\boldsymbol{A_{p1}}$. Let $a_{in} = 2r_a \sin\beta$ and $a_{ex} = 2r_a \sin\left(\frac{\pi}{3} - \beta\right)$ that are the lengths of hexagon sides. One needs to verify that $a_{in} > 2r_m$ and $a_{ex} > 2r_m$ so that it has enough distance for two motors with radius r_m.

$$a_{min} = \sqrt{b^2 + 4r_b{}^2} \text{ and } a_{max} = b + 2r_b \qquad (6.3.12.a)$$

$$\gamma_{in} = g(a_{in}) \text{ and } \gamma_{ex} = g(a_{ex}) \qquad (6.3.12.b)$$

Table 6.3.1 gives γ_{in} and γ_{ex} as offsets on α_{pi} and α_{qi}, to be interference free for section 1.

$$\alpha_{pi} \text{ and } \alpha_{qi} \in \left[\gamma_{in}, \frac{240}{180}\pi - \gamma_{ex} \right] \qquad (6.3.12.c)$$

Table 6.3.1 Angles offsets.

| Conditions	$g(a_x)$
$a_x \in (0, a_{min}]$	$\sin^{-1}\left(\dfrac{2r_b}{a_x}\right)$
$a_x \in [a_{min}, a_{max}]$	$\cos^{-1}\left(\dfrac{b^2 + a_x{}^2 - 4r_b{}^2}{2 \cdot a_x \cdot b}\right)$
$a_x \in [a_{max}, \infty)$	0

127

Section 2 is to wipe out the conditions where α_{pi} and α_{qi} are within ranges but there exists intersection of links in a loop (see loop 1 and loop 2 in figure 6.3.4. (b)). An algorithm of pentagon identification could easily find intersection. For concave or convex pentagons, the sum θ_i should be 3π to be interference free for section 2.

$$\theta_i = \alpha_{pi} + \beta_{qi} + \alpha_{pi} + \beta_{qi} + \gamma_i \tag{6.3.13}$$

Section 3 is to avoid the moving arc of a link interfering with the moving side of a link in another loop. Such as in figure 6.3.5. (b), the arc of $\boldsymbol{B_{p1}}$ interferes with the side of $\boldsymbol{A_{q3}B_{q3}}$. For when $\alpha_{pi} + \alpha_{qk} > 5\pi/3$ (i and k index two loops in clockwise order), the point-line criteria could conveniently check the distance between the two. The link $\boldsymbol{B_{pi}C_i}$ or $\boldsymbol{B_{qi}C_i}$ are in different horizontal layers, thus are exempted form examination. The point-line criteria in table 6.3.2 need to be met to be interference free for section 3. For example, a point $\boldsymbol{B_{pi}}$ should be a distance r_b away from line $\boldsymbol{A_{qk}B_{qk}}$, when $\alpha_{pi} > \alpha_{qk}$.

Table 6.3.2 Point-line criteria.

Conditions	Criteria
$\alpha_{pi} > \alpha_{qk}$	$\boldsymbol{Z_o} \cdot \left(\boldsymbol{B_{pi}A_{qk}} \times \boldsymbol{B_{pi}B_{qk}}\right) - 2r_b b > 0$
$\alpha_{pi} < \alpha_{qk}$	$\boldsymbol{Z_o} \cdot \left(\boldsymbol{B_{qk}B_{pi}} \times \boldsymbol{B_{qk}A_{pi}}\right) - 2r_b b > 0$
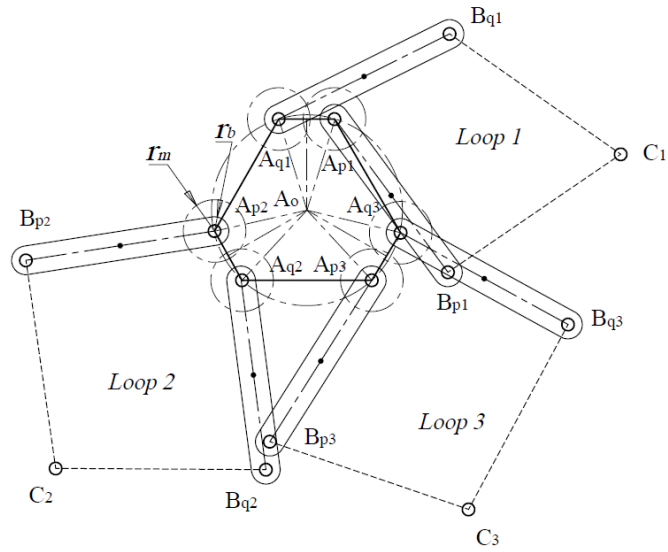
(a)
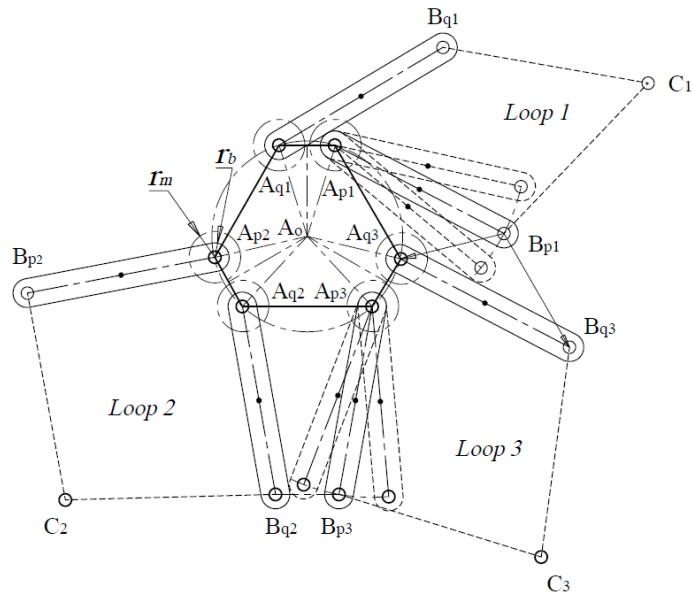
(b)

Figure 6.3.5 Interference detection.

129

In figure 6.3.6. (a), from the global cartesian coordinate at A_o, the moving platform center E_o has a linear velocity v_{eo} and an angular velocity ω_{eo}, that contribute to the linear velocity at E_i. The linear velocity at D_i could be divided to v_{xdi} and v_{ydi}, which are along X_{di} and Y_{di} respectively.

A method of dot multiplication [91] [92] can be used since v_{xdi} is not perpendicular to E_iD_i.

$$E_iD_i \cdot (v_{eo} + \omega_{eo} \times E_oE_i) = E_iD_i \cdot v_{xdi} \qquad (6.3.14.a)$$

So that

$$v_{xdi} = \frac{E_iD_i \cdot (v_{eo} + \omega_{eo} \times E_oE_i)}{E_iD_i \cdot X_{di}} \cdot X_{di} \qquad (6.3.14.b)$$

The angular velocity ω_{eo} could be divided to ω_{ei}, ω_{yi} and ω_{zi}, that are along E_oE_i, Y_{di} and Z_o respectively. Components ω_{ei} and ω_{yi} have no contribution to v_{ydi}, except ω_{zi}.

$$v_{eo} \cdot Y_{di} \cdot Y_{di} + \omega_{zi} \times E_oD_i = v_{ydi} \qquad (6.3.15.a)$$

where

$$\omega_{zi} = \left(\omega_{eo} \cdot Z_o - \frac{E_oE_i \cdot Z_o}{E_oE_i \cdot X_{di}} \cdot \omega_{eo} \cdot X_{di}\right) \cdot Z_o \qquad (6.3.15.b)$$

So that

$$v_{ydi} = v_{eo} \cdot Y_{di} \cdot Y_{di} + \left(\omega_{eo} \cdot Z_o - \frac{E_oE_i \cdot Z_o}{E_oE_i \cdot X_{di}} \cdot \omega_{eo} \cdot X_{di}\right) \cdot Z_o \times E_oD_i \quad (6.3.15.c)$$

The angular velocity $\omega_{pi} \cdot Z_o$ and $\omega_{qi} \cdot Z_o$ are the actuation angular velocities at A_{pi} and A_{qi}.

$$B_{pi}C_i \cdot (v_{xdi} + v_{ydi}) = B_{pi}C_i \cdot (Z_o \times A_{pi}B_{pi}) \cdot \omega_{pi} \qquad (6.3.16)$$

So that,

$$\omega_{pi} = \boldsymbol{J}_{pvi}^{T} \cdot \boldsymbol{v}_{eo} + \boldsymbol{J}_{pwi}^{T} \cdot \boldsymbol{\omega}_{eo} \qquad (6.3.17.a)$$

where,

$$\boldsymbol{J}_{pvi} = \frac{B_{pi}C_i \cdot X_{di}}{B_{pi}C_i \cdot (Z_o \times A_{pi}B_{pi})} \cdot \frac{E_i D_i}{E_i D_i \cdot X_{di}} + \frac{B_{pi}C_i \cdot Y_{di} \cdot Y_{di}}{B_{pi}C_i \cdot (Z_o \times A_{pi}B_{pi})} \qquad (6.3.17.b)$$

$$\boldsymbol{J}_{pwi} = \frac{B_{pi}C_i \cdot X_{di}}{B_{pi}C_i \cdot (Z_o \times A_{pi}B_{pi})} \cdot \frac{E_i D_i \times E_i E_o}{E_i D_i \cdot X_{di}} + \frac{B_{pi}C_i \cdot (Z_o \times E_o D_i) \cdot Z_o}{B_{pi}C_i \cdot (Z_o \times A_{pi}B_{pi})} - \frac{E_o E_i \cdot Z_o}{E_o E_i \cdot X_{di}} \cdot \frac{B_{pi}C_i \cdot (Z_o \times E_o D_i) \cdot X_{di}}{B_{pi}C_i \cdot (Z_o \times A_{pi}B_{pi})} \qquad (6.3.17.c)$$
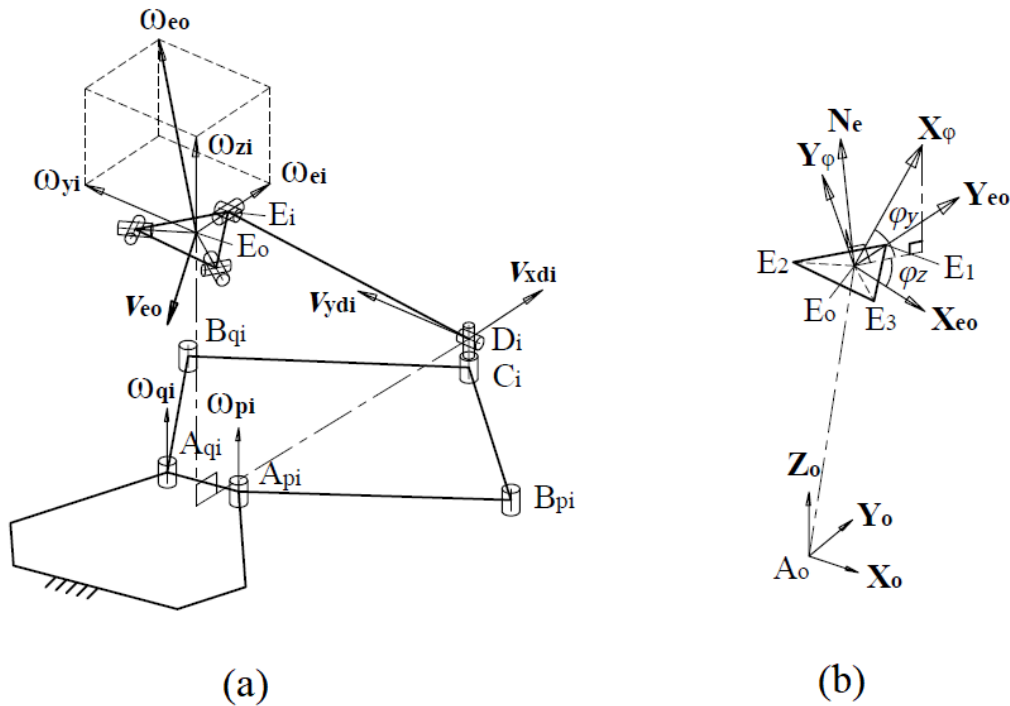
Figure 6.3.6 Jacobian matrix analysis.

One could have the similar for ω_{qi}, $\boldsymbol{J}_{qvi}$ and $\boldsymbol{J}_{qwi}$. The Jacobian matrix is obtained as below.

$$J = \begin{bmatrix} J_{pv1} & J_{pv2} & J_{pv3} & J_{qv1} & J_{qv2} & J_{qv3} \\ J_{pw1} & J_{pw2} & J_{pw3} & J_{qw1} & J_{qw2} & J_{qw3} \end{bmatrix}^T \qquad (6.3.18.a)$$

So that,

$$\begin{bmatrix} \omega_p \\ \omega_q \end{bmatrix} = J \begin{bmatrix} v_{eo} \\ \omega_{eo} \end{bmatrix} \qquad (6.3.18.b)$$

The stiffness of manipulator at E_o by the global cartesian coordinate at A_o is given as K_a which is related to the stiffness of actuator $K_q = k_q \cdot I_6$ through Jacobian matrix J [41].

$$K_a = J^T K_q J \qquad (6.3.18.c)$$

A transformation matrix is needed to convert to another coordinate system. In figure 6.3.6. (b), the coordinate system is established at E_o with unit vectors X_{eo}, Y_{eo} and N_e. Vector X_o from global coordinate A_o equals the X_{eo} from the platform coordinate at E_o. One could transform J to J_e.

$$(X_o)_{Ao} = (X_{eo})_{Eo} \qquad (6.3.19.a)$$

$$(X_{eo})_{Ao} = R(X_o)_{Ao} = R(X_{eo})_{Eo} \qquad (6.3.19.b)$$

$$J_e = J \begin{bmatrix} R & 0_{3,3} \\ 0_{3,3} & R \end{bmatrix} \qquad (6.3.19.c)$$

Similarly, In figure 6.3.6. (b) a coordinate of Φ has a vector X_φ that rotates from X_{eo} by φ_y and φ_z.

$$(X_o)_{Ao} = (X_\varphi)_\Phi \qquad (6.3.20.a)$$

$$(X_\varphi)_{Ao} = R(X_\varphi)_{Eo} = R R_z R_y (X_\varphi)_\Phi \qquad (6.3.20.b)$$

$$R_z = \begin{bmatrix} \cos\varphi_z & -\sin\varphi_z & 0 \\ \sin\varphi_z & \cos\varphi_z & 0 \\ 0 & 0 & 1 \end{bmatrix} \text{ and } R_y = \begin{bmatrix} \cos\varphi_y & 0 & \sin\varphi_y \\ 0 & 1 & 0 \\ -\sin\varphi_y & 0 & \cos\varphi_y \end{bmatrix} \qquad (6.3.20.\text{c})$$

A vector in coordinate A_o could be converted to that in coordinate Φ. One could transform J to J_φ.

$$J_\varphi = J \begin{bmatrix} RR_zR_y & 0_{3,3} \\ 0_{3,3} & RR_zR_y \end{bmatrix} \qquad (6.3.20.\text{d})$$

$$K_\varphi = J_\varphi{}^T K_q J_\varphi \qquad (6.3.20.\text{e})$$

6.3.3 Multi-objective Design Optimization

The workspace is evaluated by setting three orientations θ_{ej} ($j = 1,2,3$) of the platform, and then searching for all eligible positions of the E_o within the searching ranges. The number n_{ej} of the eligible positions indicate the volume of the workspace by orientation θ_{ej}.

Considering the efficiency of workspace (largest workspace made by minimum limb sizes), cost function f_j is taken. Pareto method [104] is used to search for the best result of each cost function with non-sacrifice to another cost function.

$$f_j = -\frac{n_{ej}}{\left(\sum_{i=1}^{5} x_i\right)^3} \qquad (6.3.21)$$

The basic modeling parameters are given in table 6.3.3. Table 6.3.4 gives the ranges of the optimization variables $x_1 \sim x_6$, considering that each revolute or universal joint is at least 0.05 m from the center of a body it connects to. Table 6.3.5 gives the three orientations, and the E_o search ranges by each orientation.

Table 6.3.6 shows the results of the optimization and the cost function value, where $F = f_1 + f_2 + f_3$. The four results are selected from the final optimization solutions, with result 1 for the best of f_1; result 2 for the best of f_2; result 3 for the best of f_3; and result 4 for the best of F overall. The result 4 is chosen for the full workspace plotting in $\boldsymbol{\theta_{e1}}$, $\boldsymbol{\theta_{e2}}$ and $\boldsymbol{\theta_{e3}}$ in figure 6.3.7.

Table 6.3.3 Modeling parameters.

Parameters	Values	Units
d	0	m
r_b	0.015	m
r_c	0.010	m
r_m	0.025	m
α_i	$(4i-1)\pi/6$	rad

Table 6.3.4 Optimization variables.

	x_1	x_2	x_3	x_4	x_5	x_6
Variables	e	r_e	r_a	b	c	β
Ranges	[0.1, 0.7]	[0.05,0.7]	[0.05,0.7]	[0.1, 0.7]	[0.1,0.7]	$[\pi/18, 5\pi/18]$
Units	m	m	m	m	m	rad

Table 6.3.5 Motion and search ranges.

Orientations and positions	Values	Units
$\boldsymbol{\theta_{e1}}$	[0 0 0]	rad
$\boldsymbol{\theta_{e2}}$	[$\pi/6$ 0 0]	rad
$\boldsymbol{\theta_{e3}}$	[0 0 $\pi/6$]	rad
x_e	-0.1: 0.05: 0.1	m
y_e	-0.1: 0.05: 0.1	m
z_e	0.1: 0.05: 0.3	m

Table 6.3.6 Optimization results.

	x_1	x_2	x_3	x_4	x_5	x_6	f_1	f_2	f_3	F
Result 1	0.361	0.051	0.102	0.207	0.218	0.296	-126.574	-89.204	-94.026	-309.804
Result 2	0.345	0.051	0.102	0.208	0.219	0.303	-119.825	-119.825	-99.644	-339.294
Result 3	0.386	0.051	0.079	0.245	0.232	0.344	-120.724	-85.939	-111.52	-318.179
Result 4	0.348	0.051	0.102	0.205	0.219	0.300	-121.277	-117.488	-101.07	-339.829
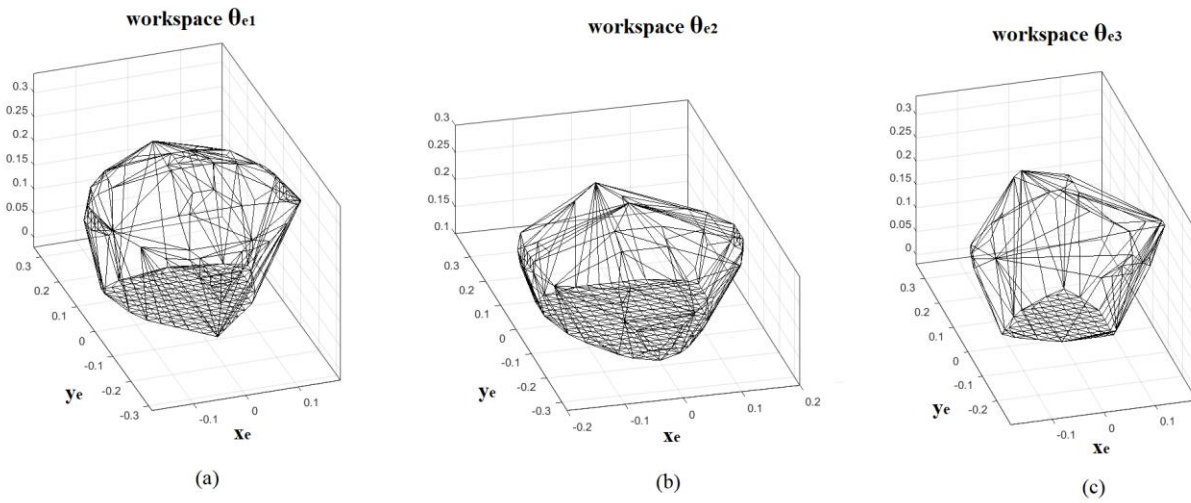
Figure 6.3.7 Full workspace in $\boldsymbol{\theta_{e1}}, \boldsymbol{\theta_{e2}}, \boldsymbol{\theta_{e3}}$ of result 4.
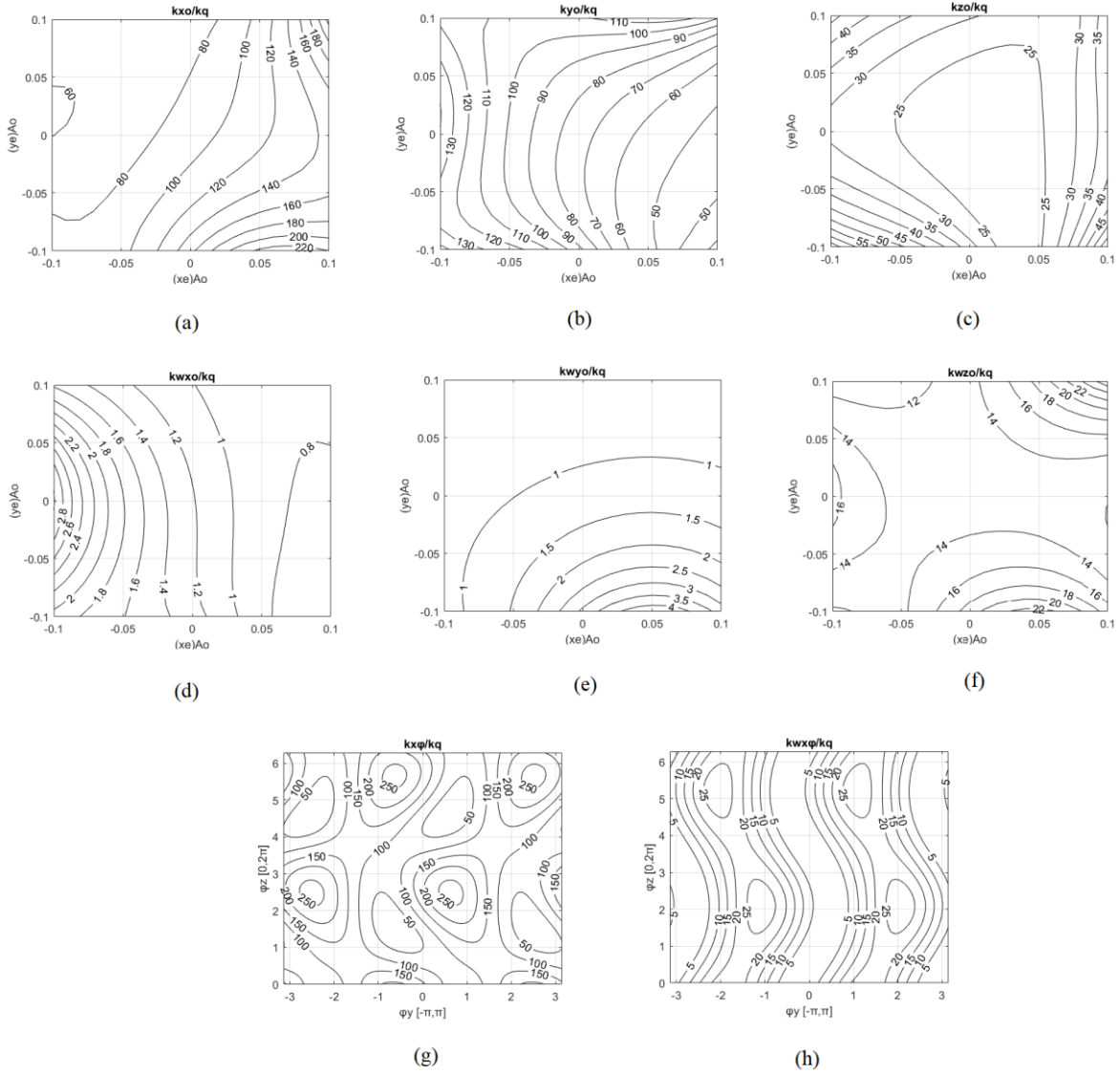
Figure 6.3.8 Stiffness mapping $\boldsymbol{\theta_e} = \left[15 \cdot \dfrac{\pi}{180} \quad 20 \cdot \dfrac{\pi}{180} \quad 10 \cdot \dfrac{\pi}{180}\right]^T$.

As one could calculate the stiffness in or around $\boldsymbol{X_\varphi}$. The polar stiffness of the end effector center $\boldsymbol{E_o}$ at any pose could be plotted about rotation angle φ_y and φ_z. The unit stiffness in and around vectors $\boldsymbol{X_o}, \boldsymbol{Y_o}, \boldsymbol{Z_o}$ from global coordinate at $\boldsymbol{A_o}$ are mapped over an area of $\boldsymbol{E_o} = [x_e \quad y_e \quad 0.2]^T$

in figure 6.3.8. (a)~(f). The unit stiffness in and around X_φ from given coordinate of Φ is mapped about angle $[\varphi_y \quad \varphi_z]$ when $E_o = [0.1 \quad 0.1 \quad 0.2]^T$ in figure 6.3.8. (g) and (h).

6.3.4 Section Conclusion

A 3-[(2-$\underline{RR}$)UU] 6-DOF parallel manipulator is designed with limbs in mobile vertical planes. The pentagon identification and point-line criteria are developed for link interference detection. The workspace boundaries of different orientation angles are plotted. The unit stiffness in and around the global coordinate vectors are mapped. With a transformation matrix this stiffness could be converted to indicate stiffness in or around any vector that is a rotation angle from the global coordinate system.

6.4 Novel Design of 5-DOF 3T2R Parallel Mechanism

There are 5-DOF serial manipulators such as [163] [164], but none has been designed with 3T2R motion. There is a 3T2R manipulator [165] [166] fully parallel with 5 limbs. Hybrid limbs could offer larger workspace than fully parallel manipulators.

A novel 5-DOF 3T2R parallel manipulator is designed with chains set in perpendicular planes. The synthesis design is based on motion sets intersection and disseminated Chebychev-Grübler-Kutzbach formula. A boundary offset method is developed to detect link interference between links in a same plane. A multi-objective optimization is practiced on the design for multiple performance improvements. The Jacobian stiffness based on oriented platform coordinate is developed. This section also discusses the potential applications of the design.

6.4.1 The PRPU Equivalent Mechanism Design

Classical Chebychev-Grübler-Kutzbach formula could determine the degree of freedom (DOF) of a mechanism.

$$M = 6(B - J - 1) + \sum_{i=1}^{n} d_i \qquad (6.4.1.\text{a})$$

The classical formula can be disseminated to represent the DOF of platform and limbs separately, where the platform and base has the initial DOF denoted as M_{eo}, and the limb chain i has its individual DOF denoted as M_{ei} with d_i for joints. The total DOF of a parallel manipulator is M.

$$M = M_{eo} + \sum_{i=1}^{n} M_{ei} \qquad (6.4.1.\text{b})$$

$$M_{eo} = 6(2 - 1) = 6 \qquad (6.4.1.\text{c})$$

$$M_{ei} = 6(-1) + d_i \qquad (6.4.1.\text{d})$$

Based on the motion sets intersection of a parallel manipulator, M is restricted by $\min(M_{eo} + M_{ei})$.

$$M = \min(M_{eo} + M_{ei}) = d_i \qquad (6.4.1.\text{e})$$

In figure 6.4.1. (a), the motion of a serial limb is the addition from three parts. These are the motions of the links on horizontal plane Z, the motions of the links on vertical plane X and the motions of the connection joint which connects plane X and platform. A coordinate system with x, y and z axes is set at a point on the intersecting line of plane Z and plane X where they are jointed. The axis z is normal to plane Z, while the axis y is along the intersecting line of Plane Z and plane X.

The R_x, R_y and R_z represent the rotational motions around x, y and z axes. The T_x, T_y and T_z represent translational motions along x, y and z axes. A series of these symbols in sequence define the motions of a chain from the base to the end effector (from left to right). There are some properties of the symbols as to whether they are commutative.

$$R_y R_x \neq R_x R_y \text{ and } T_x T_y = T_y T_x \tag{6.4.2.a}$$

$$T_y R_x \neq R_x T_y \text{ and } T_x R_x = R_x T_x \tag{6.4.2.b}$$

In plane X, normal to x axis, R_x^3 can be any member of the four members of a set, where each member includes three motions. The three motions shall be enough to reach any position or rotaion in plane X. The motions under one bar can change their orders. R_y^3 and R_z^3 are similar as R_x^3.

$$R_x^3 \in \{\overline{T_y T_z R_x}, \overline{T_y R_x R_x}, \overline{T_z R_x R_x}, R_x R_x R_x\} \tag{6.4.2.c}$$

$$T_x R_x^3 = R_x^3 T_x \tag{6.4.2.d}$$

R_x^2 can be any member of the five members of a set, where each member includes two motions. One could find the properties of the motion groups as below.

$$R_x^2 \in \{T_y R_x, R_x T_y, T_z R_x, R_x T_z, R_x R_x\} \tag{6.4.2.e}$$

$$R_x^2 R_y^3 = R_x^3 R_y^2 \tag{6.4.2.f}$$

The rotational motion group $\overline{R_x R_y R_z}$ exists when the three rotational axes join at one single point like a spherical joint. The following condition is equivalent to a spherical joint.

$$R_x^3 R_y R_z = R_x^2 \overline{R_x R_y R_z} = \overline{T_y T_z} \; \overline{R_x R_y R_z} \tag{6.4.2.g}$$

To organize a given motion group such as $T_x T_y T_z R_x R_y$ to two perpendicular planes and the connection point, one needs to define the first plane, the second plane, and the point where second plane connects to end effector.

Here, motions in first plane (plane Z) could be defined as $\widehat{P_z}$; motions in second plane (plane X) as $\widehat{P_x}$; and the motions at the connection point as $\widehat{D_x}$ which can be any of the six members below.

$$\widehat{D_x} \in \{R_y, R_z, R_y R_x, R_y R_z, R_z R_x, R_z R_y \} \tag{6.4.2.h}$$

In table 6.4.1. the 5-DOF chain is the main limb of the manipulator. Its structure is selected as $T_x \overline{T_y R_x R_x} R_y$, or known as PRPU as to name the joints.

Table 6.4.1 Motions $T_x T_y T_z R_x R_y$ in $\widehat{P_z}\ \widehat{P_x}\ \widehat{D_x}$.

$\widehat{P_z}$	$\widehat{P_x}$	$\widehat{D_x}$	Options
T_x	$\overline{T_y T_z R_x}$	R_y	5
T_x	$\overline{T_y R_x R_x}$	R_y	3
T_x	$R_x R_x R_x$	R_y	1

For options of the other two limbs, the (2-<u>R</u>R)UU ($R_z R_z R_z\ R_x R_x\ R_y$) chain of 6-DOF is selected. Figure 6.4.1. (b) shows the topology diagram that represents the whole structure with nodes for bodies and lines for joints. Figure 6.4.1. (c) and (d) show the manipulator in working and lie-flat postures. The structure is denoted as PR<u>P</u>U/2-[(2-<u>R</u>R)UU] according to [48]. The linear actuator (model: DLA-12-40-311-200-IP65) [158] actuates prismatic joint <u>P</u>. The five-bar mechanism [161] is actuated by worm gear motors (model: 9DCW□-120-30) [167] on revolute joint <u>R</u>.

The parallel five-bar mechanism takes weight at joint R[II] as the parallel arms could take more load than a serial arm. For heavy load applications, it can be considered to attach an elastic support (such as a spring and a ball) under the joint R[II] where the support rests on the floor.
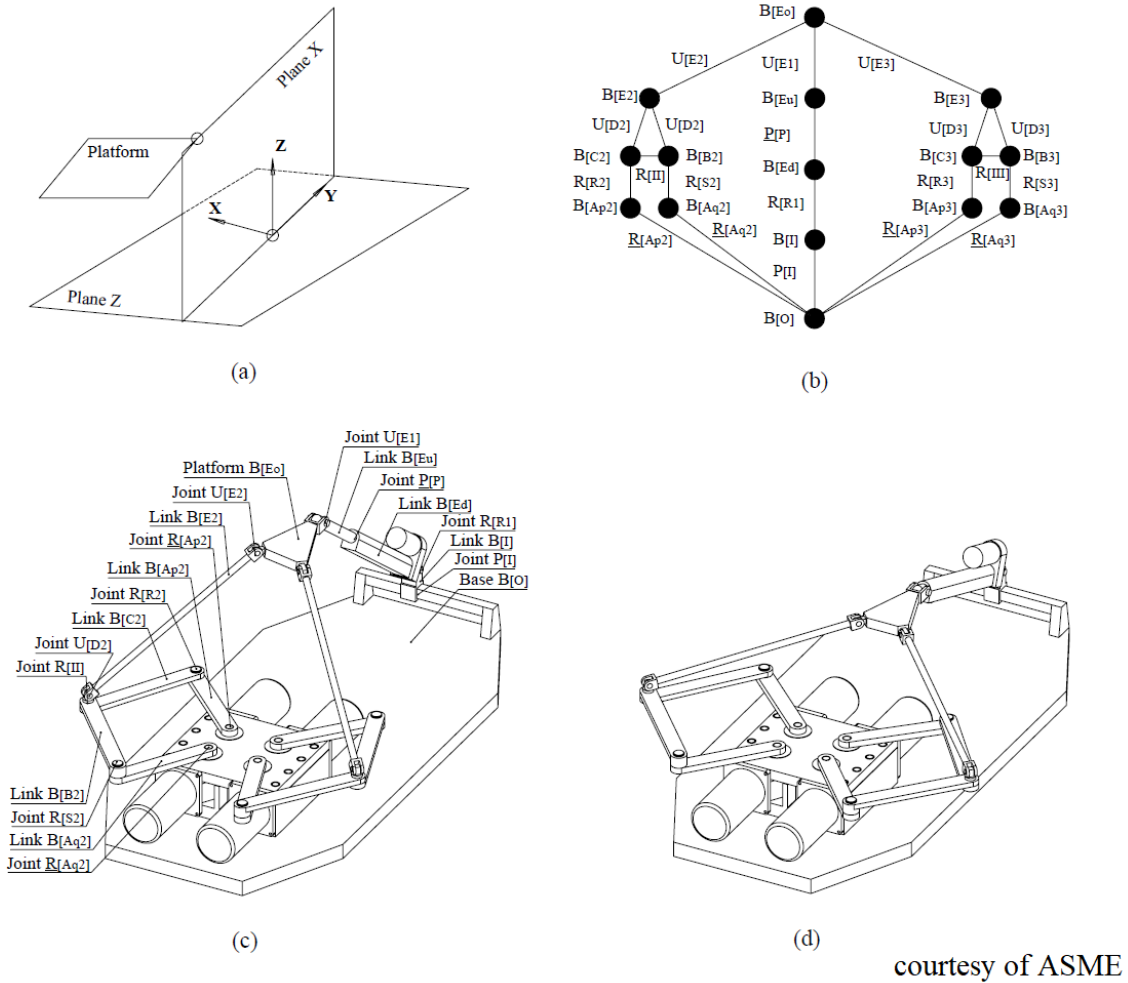

Figure 6.4.1 Mechanical design. (a) perpendicular planes form the pattern of a limb; (b) 3T2R parallel manipulator topology diagram; (c) the 3T2R parallel manipulator in working posture; (d) lie-flat posture.

6.4.2 Inverse Kinematics and Stiffness

Link positions calculation and link interference detection are performed to evaluate the workspace.

(a)

(b)

(c)

(d)
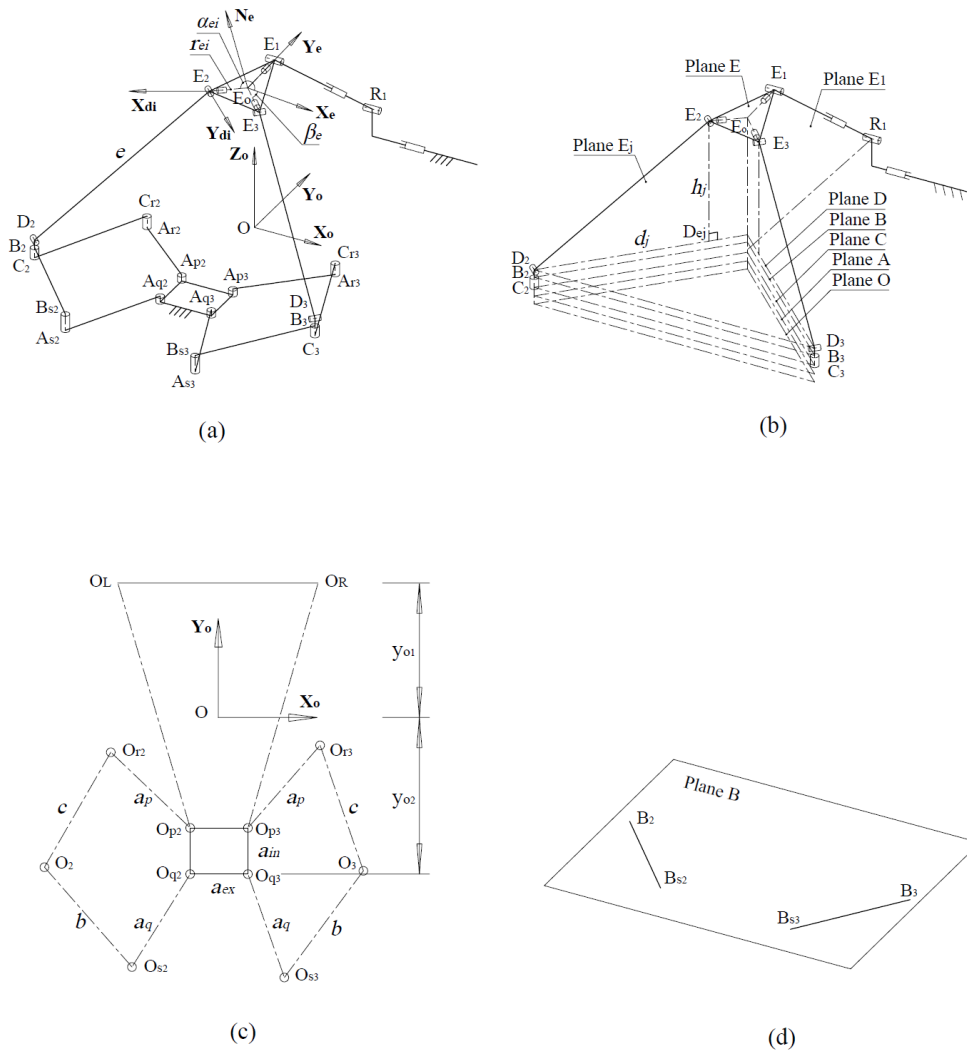
courtesy of ASME

Figure 6.4.2 Kinematics analysis. (a) the kinematic analysis; (b) the limbs in vertical planes and horizontal planes; (c) links on horizontal planes projected on plane O; (d) links on plane B.

In figure 6.4.2. (a), the base center is at $\boldsymbol{O}$: $[0\ 0\ 0]^T$. The $\boldsymbol{X_o}$, $\boldsymbol{Y_o}$ and $\boldsymbol{Z_o}$ are three orthogonal unit vectors of the global coordinate.

$$\boldsymbol{X_o} = [1\ 0\ 0]^T, \boldsymbol{Y_o} = [0\ 1\ 0]^T, \boldsymbol{Z_o} = [0\ 0\ 1]^T \tag{6.4.3}$$

The three limbs are in three mobile vertical planes E_1, E_j ($j = 2,3$) in figure 6.4.2. (b).

The platform has 5 DOFs. These are three translational motions $x_e\boldsymbol{X_o}$, $y_e\boldsymbol{Y_o}$, $z_e\boldsymbol{Z_o}$ and two orientation motions $\theta_{ex}\boldsymbol{X_o}$, $\theta_{ey}\boldsymbol{Y_e}$, so that $\boldsymbol{E_i}$ ($i = 1,2,3$) are obtained.

$$\boldsymbol{E_o} = [x_e \quad y_e \quad z_e]^T \tag{6.4.4}$$

$$\boldsymbol{E_i} = \boldsymbol{E_o} + \boldsymbol{R_{ex}}\boldsymbol{R_{ey}}r_{ei}[\cos\alpha_{ei} \ \text{sos}\ \alpha_{ei} \ 0]^T \tag{6.4.5.a}$$

Where

$$\boldsymbol{R_{ex}} = \begin{bmatrix} 1 & 0 & 0 \\ 0 & \cos\theta_{ex} & -\sin\theta_{ex} \\ 0 & \sin\theta_{ex} & \cos\theta_{ex} \end{bmatrix} \tag{6.4.5.b}$$

$$\boldsymbol{R_{ey}} = \begin{bmatrix} \cos\theta_{ey} & 0 & \sin\theta_{ey} \\ 0 & 1 & 0 \\ -\sin\theta_{ey} & 0 & \cos\theta_{ey} \end{bmatrix} \tag{6.4.5.c}$$

The oriented coordinate is at $\boldsymbol{E_o}$ with orthogonal unit vectors $\boldsymbol{X_e}$, $\boldsymbol{Y_e}$ and $\boldsymbol{N_e}$.

$$\boldsymbol{Y_e} = \frac{1}{r_{e1}}(\boldsymbol{E_o E_1}), \ \boldsymbol{X_e} = \boldsymbol{Y_e} \times \boldsymbol{N_e}, \ \boldsymbol{N_e} = \frac{\boldsymbol{E_o E_1} \times \boldsymbol{E_o E_2}}{|\boldsymbol{E_o E_1} \times \boldsymbol{E_o E_2}|} \tag{6.4.6}$$

Another coordinate is at $\boldsymbol{E_i}$ with unit vectors $\boldsymbol{X_{di}}$ and $\boldsymbol{Y_{di}}$ about vertical planes.

$$\boldsymbol{Y_{di}} = \frac{\boldsymbol{Z_o} \times \boldsymbol{E_o E_i}}{|\boldsymbol{Z_o} \times \boldsymbol{E_o E_i}|} \ \text{and}\ \boldsymbol{X_{di}} = \boldsymbol{Y_{di}} \times \boldsymbol{Z_o} \tag{6.4.7}$$

Since limb 2 and limb 3 are in mobile vertical planes, the $\boldsymbol{D_j}$ positions could be obtained.

$$h_j = \boldsymbol{E_j} \cdot \boldsymbol{Z_o} - h_d \text{ and } d_j = \sqrt{e^2 - h_j{}^2} \tag{6.4.8}$$

$$\boldsymbol{D_j} = \boldsymbol{E_j} + d_j\boldsymbol{X_{dj}} - h_j\boldsymbol{Z_o} \tag{6.4.9}$$

The links of the five-bar mechanism are on different horizontal planes. These can be projected on plane O for ease of kinematics, as shown in figure 6.4.2. (c).

$$\boldsymbol{O_{q2}} = \boldsymbol{O} + y_{o2}\boldsymbol{Y_o} - 0.5a_{ex}\boldsymbol{X_o} \tag{6.4.10.a}$$

$$\boldsymbol{O_{q3}} = \boldsymbol{O} + y_{o2}\boldsymbol{Y_o} + 0.5a_{ex}\boldsymbol{X_o} \tag{6.4.10.b}$$

$$\boldsymbol{O_{pj}} = \boldsymbol{O_{qj}} + a_{in}\boldsymbol{Y_o} \tag{6.4.10.c}$$

$$p_j = \left|\boldsymbol{O_{pj}O_j}\right| \text{ and } q_j = \left|\boldsymbol{O_{qj}O_j}\right| \tag{6.4.11.a}$$

$$\gamma_{pj} = \cos^{-1}\left(\frac{a_p{}^2 + p_j{}^2 - c^2}{2a_p p_j}\right) \tag{6.4.11.b}$$

$$\gamma_{qj} = \cos^{-1}\left(\frac{a_q{}^2 + q_j{}^2 - b^2}{2a_q q_j}\right) \tag{6.4.11.c}$$

$$\boldsymbol{R_{pj}} = \begin{bmatrix} \cos\gamma_{pj} & \sin\gamma_{pj} & 0 \\ -\sin\gamma_{pj} & \cos\gamma_{pj} & 0 \\ 0 & 0 & 1 \end{bmatrix} \tag{6.4.11.d}$$

$$\boldsymbol{R_{qj}} = \begin{bmatrix} \cos\gamma_{qj} & -\sin\gamma_{qj} & 0 \\ \sin\gamma_{qj} & \cos\gamma_{qj} & 0 \\ 0 & 0 & 1 \end{bmatrix} \tag{6.4.11.e}$$

$$\boldsymbol{O_{rj}} = \boldsymbol{R_{pj}}\left(\boldsymbol{O_{pj}O_j}\right)\frac{a_p}{p_j} + \boldsymbol{O_{pj}} \tag{6.4.11.f}$$

$$\boldsymbol{O_{sj}} = \boldsymbol{R_{qj}}\left(\boldsymbol{O_{qj}O_j}\right)\frac{a_q}{q_j} + \boldsymbol{O_{qj}} \tag{6.4.11.g}$$

The h_a, h_b, h_c and h_d need to be considered to calculate the actual height of links.

In figure 6.4.2. (d), links $B_{s2}B_2$ and $B_{s3}B_3$ are in plane B. The links of the five-bar mechanism are in different planes. Link interference needs to be checked for links in each plane.

In figure 6.4.3. (a), let's suppose two links P_1P_2 and Q_1Q_2 with boundary of r_p and r_q respectively are in one plane. When boundaries offset is taken, this problem is changed to link P_1P_2 with boundary $r_p + r_q$ and a line segment Q_1Q_2. The two shall not interfere with each other. The link P_1P_2 with offset boundary will be divided to three areas I, II and III as shown in figure 6.4.3. (c).

Criteria 1, line segment Q_1Q_2 could not touch line segments S_1S_2 or U_1U_2. Let's take Q_1Q_2 and S_1S_2 for example as shown in figure 6.4.3. (d). The same should be checked for U_1U_2.

$$(S_1Q_1 \times S_1Q_2) \cdot (S_2Q_1 \times S_2Q_2) > 0 \qquad\qquad (6.4.12.a)$$

And

$$(S_1Q_1 \times S_2Q_1) \cdot (S_1Q_2 \times S_2Q_2) > 0 \qquad\qquad (6.4.12.b)$$

Criteria 2, line segment Q_1Q_2 could not touch area I or area III. Let's take Q_1Q_2 and area I for example as shown in figure 6.4.3. (e). The same should be checked for area III.

When $(Q_1Q_2 \cdot Q_1P_1) \cdot (Q_1Q_2 \cdot Q_2P_1) > 0$

$$|Q_1P_1| > r_p + r_q \; ; |Q_2P_1| > r_p + r_q \qquad\qquad (6.4.13.a)$$

When $(Q_1Q_2 \cdot Q_1P_1) \cdot (Q_1Q_2 \cdot Q_2P_1) \leq 0$

$$|P_1Q_1 \times P_1Q_2| > |Q_1Q_2| \cdot (r_p + r_q) \qquad\qquad (6.4.13.b)$$

Criteria 3, line segment Q_1Q_2 could not touch area II. (figure 6.4.3. (f)). As criteria 1 and 2 have already been checked, criteria 3 only needs to check that Q_1 is not inside the $U_1S_1S_2U_2$ rectangle.

$$(Q_1U_1 \times Q_1U_2) \cdot (Q_1S_1 \times Q_1S_2) \geq 0 \qquad (6.4.14.a)$$
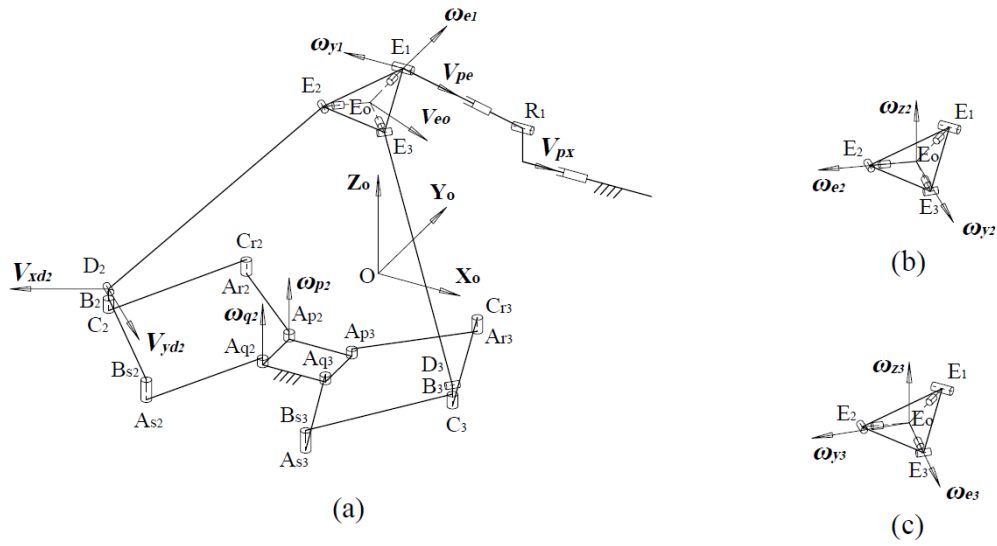
Or

$$(Q_1U_1 \times Q_1S_1) \cdot (Q_1U_2 \times Q_1S_2) \geq 0 \qquad (6.4.14.b)$$

All of criteria 1,2 and 3 need to be satisfied to be interference free for link P_1P_2 and Q_1Q_2. All links on a same plane are checked by this method and unqualified postures will not be considered for workspace/stiffness evaluation.
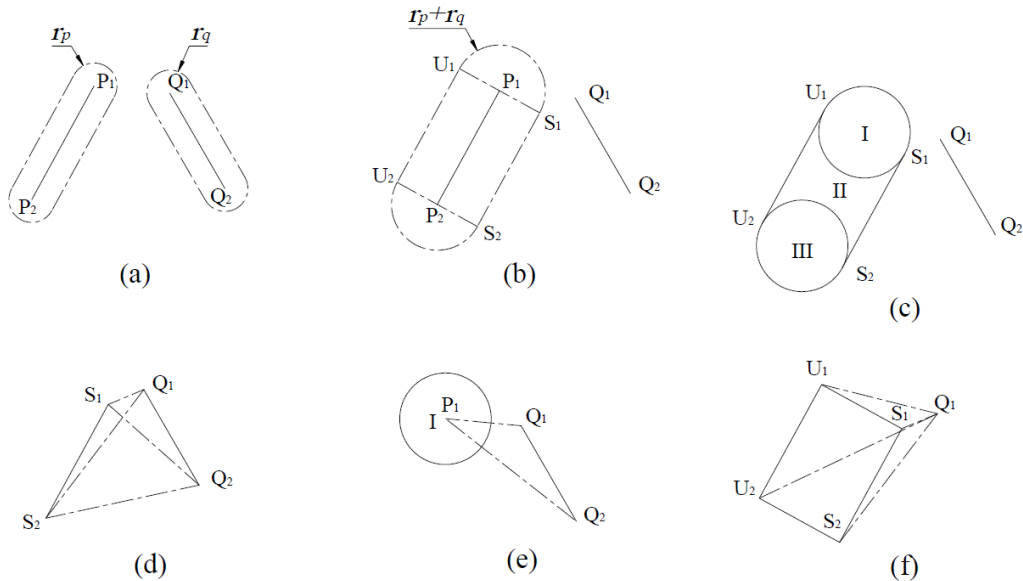
courtesy of ASME

Figure 6.4.3 Interference detection.

Figure 6.4.4 Jacobian matrix analysis.

In figure 6.4.4. (a), from the global cartesian coordinate at $\boldsymbol{O}$, the moving platform center $\boldsymbol{E_o}$ has

a linear velocity $\boldsymbol{v_{eo}}$ and an angular velocity $\boldsymbol{\omega_{eo}}$, that contribute to the linear velocity at $\boldsymbol{E_i}$.

$$\boldsymbol{v_{eo}} = v_{xo}\boldsymbol{X_o} + v_{yo}\boldsymbol{Y_o} + v_{zo}\boldsymbol{Z_o} \tag{6.4.15.a}$$

$$\boldsymbol{v_{eo}} = v_{xe}\boldsymbol{X_e} + v_{ye}\boldsymbol{Y_e} + v_{ze}\boldsymbol{N_e} \tag{6.4.15.b}$$

$$\boldsymbol{\omega_{eo}} = \omega_{e1}\boldsymbol{Y_e} + \omega_{y1}\boldsymbol{Y_{d1}} \tag{6.4.16}$$

Limb 1 has linear actuation velocity $\boldsymbol{v_{pe}}$; limb 2 or limb 3 have rotation actuation velocities $\boldsymbol{\omega_{pj}}$

and $\boldsymbol{\omega_{qj}}$.

$$\boldsymbol{v_{pe}} = v_{pe}\frac{\boldsymbol{E_1 R_1}}{|\boldsymbol{E_1 R_1}|} \tag{6.4.17.a}$$

$$\boldsymbol{\omega_{pj}} = \omega_{pj}\boldsymbol{Z_o}; \boldsymbol{\omega_{qj}} = \omega_{qj}\boldsymbol{Z_o} \tag{6.4.17.b}$$

147

For limb 1, one could get v_{pe} from v_{eo} and ω_{eo}.

$$v_{pe} = \frac{E_1 R_1}{|E_1 R_1|} (v_{eo} + \omega_{eo} \times E_o E_1) \tag{6.4.18}$$

For limb 2 or limb 3, the linear velocity at D_i could be divided to v_{xdj} and v_{ydj}, which are along X_{dj} and Y_{dj}. A method of dot multiplication [91] [92] can be used since v_{xdj} is not perpendicular to $E_j D_j$.

$$E_j D_j \cdot (v_{eo} + \omega_{eo} \times E_o E_j) = E_j D_j \cdot v_{xdj} \tag{6.4.19.a}$$

$$v_{xdj} = \frac{E_j D_j \cdot (v_{eo} + \omega_{eo} \times E_o E_j)}{E_j D_j \cdot X_{dj}} X_{dj} \tag{6.4.19.b}$$

In figure 6.4.4. (b) and (c), angular velocity ω_{eo} could be divided to ω_{ej}, ω_{yj} and ω_{zj}, that are along $E_o E_j$, Y_{dj} and Z_o respectively. Components ω_{ej} and ω_{yj} have no contribution to v_{ydj}, except ω_{zj}.

$$v_{ydj} = v_{eo} \cdot Y_{dj} \cdot Y_{dj} + \omega_{zj} \times E_o D_j \tag{6.4.20.a}$$

where

$$\omega_{zj} = \left(\omega_{eo} \cdot Z_o - \frac{E_o E_j \cdot Z_o}{E_o E_j \cdot X_{dj}} \cdot \omega_{eo} \cdot X_{dj} \right) \cdot Z_o \tag{6.4.20.b}$$

The angular velocity $\omega_{pj} \cdot Z_o$ and $\omega_{qj} \cdot Z_o$ are the actuation angular velocities at O_{pj} and O_{qj}.

$$O_{rj} O_j \cdot (v_{xdj} + v_{ydj}) = O_{rj} O_j \cdot (Z_o \times O_{pj} O_{rj}) \omega_{pj} \tag{6.4.21.a}$$

$$O_{sj} O_j \cdot (v_{xdj} + v_{ydj}) = O_{sj} O_j \cdot (Z_o \times O_{qj} O_{sj}) \omega_{qj} \tag{6.4.21.b}$$

In a summary, for limb 1, one could get the following relationship.

$$v_{pe} = \frac{E_1 R_1}{|E_1 R_1|} \cdot v_{eo} + \frac{E_1 R_1}{|E_1 R_1|} \times (-E_o E_1) \cdot \omega_{eo} \qquad (6.4.22)$$

For limb 2 or limb 3, one could get the following relationship.

$$\omega_{pj} = \frac{O_{rj} O_j \cdot (v_{xdj} + v_{ydj})}{O_{rj} O_j \cdot (Z_o \times O_{pj} O_{rj})} \qquad (6.4.23.a)$$

$$\omega_{qj} = \frac{O_{sj} O_j \cdot (v_{xdj} + v_{ydj})}{O_{sj} O_j \cdot (Z_o \times O_{qj} O_{sj})} \qquad (6.4.23.b)$$

So that,

$$[v_{pe} \quad \omega_{p2} \quad \omega_{q2} \quad \omega_{p3} \quad \omega_{q3}]^T = J_o [v_{xo} \quad v_{yo} \quad v_{zo} \quad \omega_{y1} \quad \omega_{e1}]^T \qquad (6.4.24.a)$$

$$[v_{pe} \quad \omega_{p2} \quad \omega_{q2} \quad \omega_{p3} \quad \omega_{q3}]^T = J_e [v_{xe} \quad v_{ye} \quad v_{ze} \quad \omega_{y1} \quad \omega_{e1}]^T \qquad (6.4.24.b)$$

Jacobian matrix J_o considers the translational motion in X_o, Y_o and Z_o; while J_e considers the translational motion in X_e, Y_e and N_e.

$$J_o = \begin{bmatrix} J_{pv1}^T & J_{pv1}^T & J_{pv1}^T & J_{pw1}^T & J_{pw1}^T \\ J_{pv2}^T & J_{pv2}^T & J_{pv2}^T & J_{pw2}^T & J_{pw2}^T \\ J_{qv2}^T & J_{qv2}^T & J_{qv2}^T & J_{qw2}^T & J_{qw2}^T \\ J_{pv3}^T & J_{pv3}^T & J_{pv3}^T & J_{pw3}^T & J_{pw3}^T \\ J_{qv3}^T & J_{qv3}^T & J_{qv3}^T & J_{qw3}^T & J_{qw3}^T \end{bmatrix} \begin{bmatrix} X_o \\ Y_o \\ Z_o \\ Y_{d1} \\ Y_e \end{bmatrix} \qquad (6.4.24.c)$$

$$J_e = \begin{bmatrix} J_{pv1}^T & J_{pv1}^T & J_{pv1}^T & J_{pw1}^T & J_{pw1}^T \\ J_{pv2}^T & J_{pv2}^T & J_{pv2}^T & J_{pw2}^T & J_{pw2}^T \\ J_{qv2}^T & J_{qv2}^T & J_{qv2}^T & J_{qw2}^T & J_{qw2}^T \\ J_{pv3}^T & J_{pv3}^T & J_{pv3}^T & J_{pw3}^T & J_{pw3}^T \\ J_{qv3}^T & J_{qv3}^T & J_{qv3}^T & J_{qw3}^T & J_{qw3}^T \end{bmatrix} \begin{bmatrix} X_e \\ Y_e \\ N_e \\ Y_{d1} \\ Y_e \end{bmatrix} \qquad (6.4.24.d)$$

where,

$$J_{pv1} = \frac{E_1 R_1}{|E_1 R_1|} \qquad (6.4.24.e)$$

149

$$J_{pw1} = \frac{E_1 R_1}{|E_1 R_1|} \times E_1 E_o \tag{6.4.24.f}$$

$$J_{pvj} = \frac{O_{rj} O_j \cdot X_{dj}}{O_{rj} O_j \cdot (Z_o \times O_{pj} O_{rj})} \frac{E_j D_j}{E_j D_j \cdot X_{dj}} + \frac{O_{rj} O_j \cdot Y_{dj} \cdot Y_{dj}}{O_{rj} O_j \cdot (Z_o \times O_{pj} O_{rj})} \tag{6.4.24.g}$$

$$J_{pwj} = \frac{O_{rj} O_j \cdot X_{dj}}{O_{rj} O_j \cdot (Z_o \times O_{pj} O_{rj})} \frac{E_j D_j \times E_j E_o}{E_j D_j \cdot X_{dj}} + \frac{O_{rj} O_j \cdot (Z_o \times E_o D_j) \cdot Z_o}{O_{rj} O_j \cdot (Z_o \times O_{pj} O_{rj})} - \frac{E_o E_j \cdot Z_o}{E_o E_j \cdot X_{dj}} \frac{O_{rj} O_j \cdot (Z_o \times E_o D_j) \cdot X_{dj}}{O_{rj} O_j \cdot (Z_o \times O_{pj} O_{rj})} \tag{6.4.24.h}$$

$$J_{qvj} = \frac{O_{sj} O_j \cdot X_{dj}}{O_{sj} O_j \cdot (Z_o \times O_{qj} O_{sj})} \frac{E_j D_j}{E_j D_j \cdot X_{dj}} + \frac{O_{sj} O_j \cdot Y_{dj} \cdot Y_{dj}}{O_{sj} O_j \cdot (Z_o \times O_{qj} O_{sj})} \tag{6.4.24.i}$$

$$J_{qwj} = \frac{O_{sj} O_j \cdot X_{dj}}{O_{sj} O_j \cdot (Z_o \times O_{qj} O_{sj})} \frac{E_j D_j \times E_j E_o}{E_j D_j \cdot X_{dj}} + \frac{O_{sj} O_j \cdot (Z_o \times E_o D_j) \cdot Z_o}{O_{sj} O_j \cdot (Z_o \times O_{qj} O_{sj})} - \frac{E_o E_j \cdot Z_o}{E_o E_j \cdot X_{dj}} \frac{O_{sj} O_j \cdot (Z_o \times E_o D_j) \cdot X_{dj}}{O_{sj} O_j \cdot (Z_o \times O_{qj} O_{sj})} \tag{6.4.24.j}$$

The singularity needs to be avoided, thus the elements in Jacobian matrix J_o or J_e should be of finite magnitude (denominator is non-zero) and at least one of its elements in any row should be non-zero.

Based on estimation of actuation stiffness K_q ($k_a = 5 \times 10^5 \, N/m$, $k_b = 10^4 \, N \cdot m/rad$). One could get the stiffness K_o and K_e at end effector [41].

$$K_o = J_o{}^T K_q J_o \tag{6.4.25.a}$$

$$K_e = J_e{}^T K_q J_e \tag{6.4.25.b}$$

Where

$$K_q = \begin{bmatrix} k_a & 0 & 0 & 0 & 0 \\ 0 & k_b & 0 & 0 & 0 \\ 0 & 0 & k_b & 0 & 0 \\ 0 & 0 & 0 & k_b & 0 \\ 0 & 0 & 0 & 0 & k_b \end{bmatrix} \tag{6.4.25.c}$$

$$
\boldsymbol{K_o} = \begin{bmatrix} k_{xo} & \cdot & \cdot & \cdot & \cdot \\ \cdot & k_{yo} & \cdot & \cdot & \cdot \\ \cdot & \cdot & k_{zo} & \cdot & \cdot \\ \cdot & \cdot & \cdot & k_{wy1} & \cdot \\ \cdot & \cdot & \cdot & \cdot & k_{we1} \end{bmatrix} \qquad (6.4.25.d)
$$

$$
\boldsymbol{K_e} = \begin{bmatrix} k_{xe} & \cdot & \cdot & \cdot & \cdot \\ \cdot & k_{ye} & \cdot & \cdot & \cdot \\ \cdot & \cdot & k_{ne} & \cdot & \cdot \\ \cdot & \cdot & \cdot & k_{wy1} & \cdot \\ \cdot & \cdot & \cdot & \cdot & k_{we1} \end{bmatrix} \qquad (6.4.25.e)
$$

Stiffness mapping of the end effector are plotted for orientation $\boldsymbol{\theta} = [\theta_{y1} \quad \theta_{e1}] = [20 \cdot \frac{\pi}{180} \quad 10 \cdot \frac{\pi}{180}]$ and platform center height $\boldsymbol{z_e} = 0.3$.

Similar to the transformation from $\boldsymbol{J_o}$ to $\boldsymbol{J_e}$, one could replace $\boldsymbol{X_o}$ with $\boldsymbol{X_e}$ or any other vector to evaluate linear stiffness in the direction of that vector. In this way, linear stiffness in any direction at $\boldsymbol{E_o}$ could be evaluated.

One could further optimize the stiffness of the structure by changing the design parameters. Once the design parameters are changed, some points will receive higher stiffness while other points may receive lower stiffness. One may have to optimize stiffness based on a certain work task. When work task changes, another stiffness optimization may need to be practiced accordingly. With the optimized workspace, the manipulator can generally reach as much place as it could. Reconfiguration or adaption of structures may be effective for task-based stiffness optimization. Or for applications that require less than 5-DOF, the redundant motions could be used to adjust for higher stiffness.

Furthermore, Jacobian matrix could be used to check for mobilities [42]. Here the rank of $\boldsymbol{J_o}$ or $\boldsymbol{J_e}$ equals M, index of DOF.

$$rank(\boldsymbol{J_o}) = rank(\boldsymbol{J_e}) = M \qquad (6.4.26)$$

6.4.3 Multi-objective Design Optimization

Workspace is the prioritized objective to be optimized with others. The modeling parameters in table 6.4.2 are constant. Table 6.4.3 gives the variables for the optimization in a 50%~150% range around the estimated values. There is no original design in the beginning. The optimization seeks design of best fitness.

In table 6.4.4, the workspace is evaluated for three orientations $\boldsymbol{\theta_{ek}}$ ($k = 1,2,3$) of the platform. All eligible positions of the $\boldsymbol{E_o}$ within the searching ranges are counted as number n_{ek} which represent the volume of the workspace by orientation $\boldsymbol{\theta_{ek}}$.

$$f_k = -n_{ek} \qquad (6.4.27)$$

Besides f_1, f_2 and f_3, other optimization objectives are f_4 for lowest height within search ranges for lie-flat posture and $f_5 = \sum_{i=1}^{5} x_i$ for minimum manipulator size. Pareto front line is used to search for the best result of all cost functions with no sacrifice to another.

Table 6.4.2 Modeling parameters.

Parameters	Values	Units
a_{in}	0.08	m
a_{ex}	0.1	m
$[r_{e1} \quad r_{e2} \quad r_{e3}]$	$[0.1 \quad 0.07 \quad 0.07]$	m
$[r_{ap} \quad r_{aq} \quad r_b \quad r_c]$	$[0.015 \quad 0.015 \quad 0.015 \quad 0.015]$	m
$[h_a \quad h_b \quad h_c \quad h_d \quad h_r]$	$[0.015 \quad 0.045 \quad 0.03 \quad 0.055 \quad 0.035]$	m
$[\alpha_{e1} \quad \alpha_{e2} \quad \alpha_{e3}]$	$[\pi/2 \quad 5\pi/4 \quad 7\pi/4]$	rad

Table 6.4.3 Optimization variables.

	x_1	x_2	x_3	x_4	x_5
Variables	y_{o1}	y_{o2}	a_p	b	e
Ranges	[0.2, 0.6]	[0.15, 0.45]	[0.1, 0.3]	[0.1, 0.3]	[0.2, 0.6]
Units	m	m	m	m	m

Table 6.4.4 Motion and search ranges.

Orientations and positions	Values	Units
x_e	-0.1: 0.05: 0.1	m
y_e	-0.1: 0.05: 0.1	m
z_e	0.2: 0.05: 0.4	m
$\boldsymbol{\theta_{e1}} = [\theta_{y1} \quad \theta_{e1}]$	$[0 \quad 0]$	rad
$\boldsymbol{\theta_{e2}} = [\theta_{y1} \quad \theta_{e1}]$	$[\pi/6 \quad 0]$	rad
$\boldsymbol{\theta_{e3}} = [\theta_{y1} \quad \theta_{e1}]$	$[0 \quad \pi/6]$	rad

Table 6.4.5 Optimization results.

	x_1	x_2	x_3	x_4	x_5	f_1	f_2	f_3	f_4	f_5
Result 1	0.384	0.301	0.169	0.199	0.325	-77	-105	-81	0.2	1.378
Result 2	0.380	0.368	0.187	0.231	0.398	-105	-85	-90	0.2	1.564
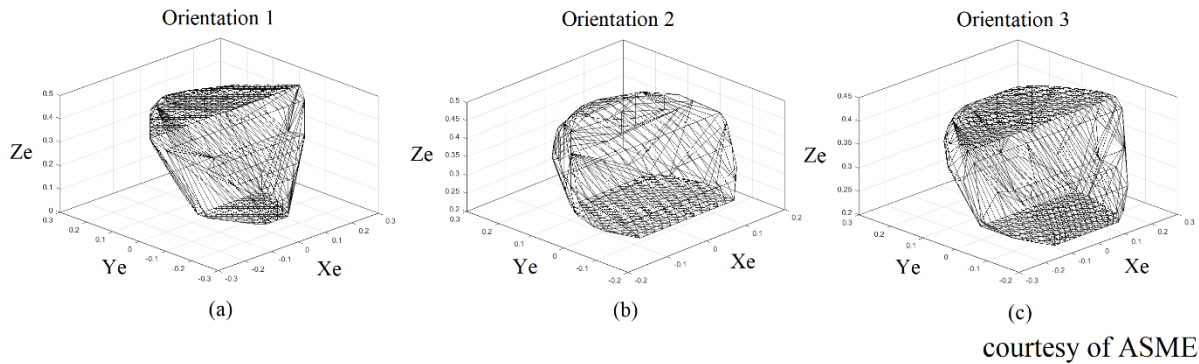
courtesy of ASME

Figure 6.4.5 Full workspace in $\boldsymbol{\theta_{e1}}, \boldsymbol{\theta_{e2}}, \boldsymbol{\theta_{e3}}$ of result 2.
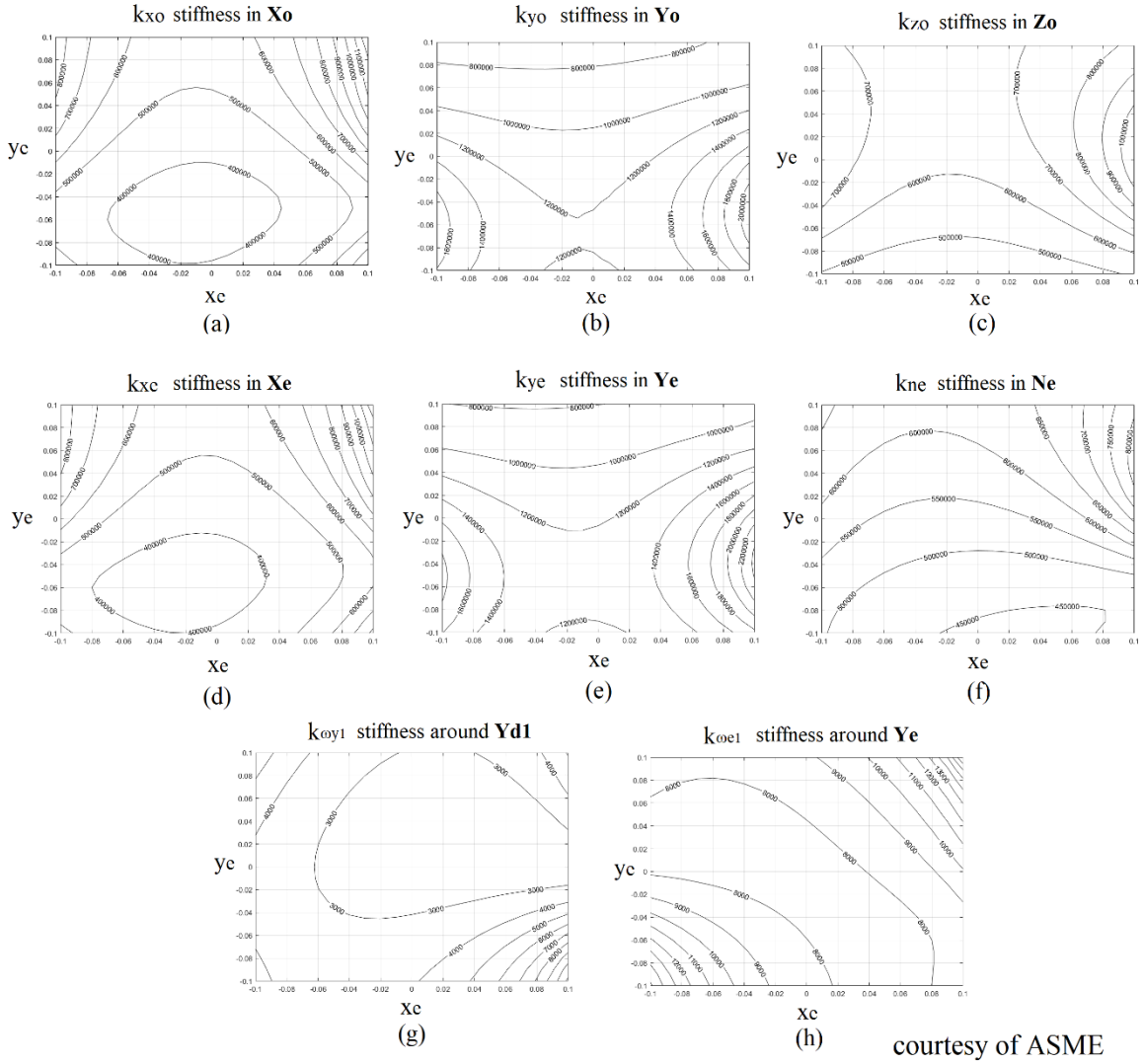
Figure 6.4.6 Stiffness mapping $\boldsymbol{\theta} = [\theta_{y1} \quad \theta_{e1}] = \left[20 \cdot \dfrac{\pi}{180} \quad 10 \cdot \dfrac{\pi}{180}\right]$ and $z_e = 0.3$.

Table 6.4.5 shows the results of the optimization and the cost function values. Two results are selected from the final optimization solutions, with result 1 for the best of f_2; result 2 for the best of f_1, and the best of $f_1 + f_2 + f_3$ coincidently.

The result 2 is selected for the full workspace plotting in $\boldsymbol{\theta}_{e1}$, $\boldsymbol{\theta}_{e2}$ and $\boldsymbol{\theta}_{e3}$ in figure 6.4.5.

154

With the diagonal of K_o and K_e, one gets eight indexes for stiffness, such as k_{xo}, k_{yo}, k_{zo} which indicate the translational stiffness in X_o, Y_o, Z_o (figure 6.4.6. (a) (b) (c)); k_{xe}, k_{ye}, k_{ne} which indicate translational stiffness in X_e, Y_e, N_e (figure 6.4.6. (d) (e) (f)); and k_{wy1}, k_{we1} which indicate the rotational stiffness around Y_{d1}, Y_e (figure 6.4.6. (g) (h)).

6.4.4 Applications

Since the 3T2R parallel manipulator has 5-DOF and lie-flat (deployable) feature, it may find applications where the structure needs to be folded. When compared to other deployable mechanisms, this manipulator has higher DOF than designs in [28] [29] [122] while it is different from a deployable stage [22].

In automobile manufacturing applications, the manipulator could work under the vehicle bodies for drilling, laser cutting or material spraying tasks, when finished it lies flat to let the vehicle passes over it until next vehicle moves over it. It could rise again and work under the vehicle body. Similarly, it could work on the vehicle bodies from top or sides.

It may also find applications for maintenance or power charging of various types of vehicles in the field. For instance, it could work under the drones, rovers or walking robots that stop over it, then it extends its 5-DOF moving platform to reach the area on the bottoms of these vehicles. Just like the solar trackers with lie-flat features which could supply power to this 5-DOF manipulator, they both can lie flat when destructive storms strike. This feature allows the structure to lie close to floor as to protect the structure from being destroyed in strong storms. Besides, it could also serve as a signal receiver stand.

When less than 5 DOFs are needed, the redundant mobilities could be adjusted for higher stiffness in demanded mobilities.

Whatever the applications, the manipulator could lie-flat close to the surface it is mounted on, to give space or to protect itself.

6.4.5 Section Conclusion

A 5-DOF 3T2R parallel manipulator with each limb in two perpendicular planes is design from synthesis method based on motion sets intersection theory and disseminated Chebychev-Grübler-Kutzbach formula. The link interference detection is checked by boundary offset method considering the width of the links. Multi-objective design optimization has been practiced. Stiffness based on both global coordinate and platform coordinate are calculated and plotted for the loading analysis of the moving platform. Potential applications of the manipulator both indoor and outdoor have been discussed.

6.5 Chapter Conclusion

A 5-DOF parallel manipulator and a 6-DOF parallel manipulator are designed that have deployable function. The 6-DOF manipulator has full mobilities and is designed with three identical 6-DOF limbs, while the 5-DOF manipulator with non-identical limbs in three mobile vertical planes is designed based on intersection of motion sets and disseminated G-K formula. The method could be adopted to develop more high-DOF deployable manipulators with limbs in mobile vertical planes. The actual DOF is verified by Jacobian matrix.

The 6-DOF manipulator interference is checked with pentagon identification, and the Point-line criteria, while the 5-DOF manipulator interference is checked with link boundary offset method. The link boundary offset method would be more generally applicable for interference identification in parallel layers.

Jacobian matrix is modified for translational or rotational stiffness evaluation in any direction. (example in 3-[(2-RR)UU])

Chapter 7 Dissertation Conclusion and Outlook

7.1 Conclusion of Research

Parallel manipulators generally have the advantages of high stiffness and precision compared to serial manipulators, however their workspaces are limited. The workspace may be further compromised when additional design requirements set constraints to the design.

Dynamic balancing and deployable feature are significant for manipulators in applications of precise manufacturing and outdoor solar tracking. The dynamically balanced manipulators contain additional balancing components, thus the link interference needs to be avoided and its energy consumption needs to be minimized. The deployable feature in non-configurable platform parallel manipulator is still rare and needs more research.

When designing dynamically balanced manipulators and deployable manipulators of high DOF (spatial mobilities greater than three), the link to link interference needs to be checked and avoided. The parallel manipulators with limbs in fixed or mobile vertical planes have the properties that provide solutions for dynamic balancing, deployable feature and interference avoidance. Novel design principles and evaluation methods are discussed. The design of parallel manipulators follows the process of task, design/evaluation and optimization.

In chapter 4, dynamically balanced planar 2-DOF, 3-DOF and spatial 2R1T 3-DOF machines are developed. The limbs are balanced in horizontal plane (planar manipulator) or fixed vertical planes (2R1T manipulator) at revolute joints. The middle joint angles are reversed to avoid link to link interference. The structural adaption and motion planning are employed for optimal energy

consumption results in the 2R1T 3-DOF spatial manipulator. By comparison of the optimization results, the combination of two approaches works better than structural adaption alone. The (2-$\underline{R}$R)R or (2-$\underline{R}$R)$\underline{R}$ planar manipulator has two base joints capable of relocation (four optimization variables on structure). The 3-$\underline{R}$RS spatial manipulator has three base joints capable of relocation (three optimization variables on structure). The adjustable variables are offered by kinematic redundancy. The 3-DOF balanced planar manipulator and 3-DOF spatial balanced manipulator can be combined to make a 6-DOF balanced manipulator. The combination yields a 6-DOF dynamically balanced machine with five adaptive base joints (seven optimization variables on structure) for optimization opportunities.

In chapter 5, two members of the 2R1T 3-DOF P*U* parallel manipulator family, 3-$\underline{P}$RS and 3-R$\underline{P}$S, are re-designed with deployable function which is useful for storm protection of outdoor working robots. For a useful but redundant motion (translation in z axis), a minimum height algorithm is developed to rapidly calculate eligible workspace. Jacobian transformation matrix is developed to calculate stiffness in any directions. The 2R1T manipulators have limbs in three fixed vertical planes and are free from interference. The kinematic redundancy in the fixed vertical planes offers optimization opportunities and wind energy harvesting opportunities.

In chapter 6, the deployable design is expanded to higher-DOF structures. A 6-DOF manipulator and a 5-DOF manipulator are designed. Their limbs are in mobile vertical planes. This design has the property of avoiding link interference and large workspace. The parallel actuation in horizontal plane that moves the vertical planes need interference check. Parallel horizontal layers partially avoid the interference and several methods are developed for convenient detection.

Genetic algorithm is suitable for complex non-linear problem optimization. The design optimization could be practiced before operation optimization. The design optimization deals with design parameters. The operation optimization deals with structural adaptive features and (or) motion planning for optimal performance of a specific task. Both design optimization and operation optimization can be single-objective or multi-objective. Among the designs from above chapters where applicable, maximum total workspace, minimum sizes and (or) minimum lie-flat height are considered as design optimization objective(s), while the minimum energy consumption for certain trajectories, maximum workspace at certain operation mode, maximum workspace at certain area, maximum and (or) maximum general stiffness at certain area are considered as operation optimization objective(s).

7.2 Research Contributions

Novel design principles and evaluation algorithms are developed. The detailed research contributions are given below.

7.2.1 Dynamic Balanced Various DOF Manipulators

1) The configuration change on original (2-$\underline{R}$R)R or (2-$\underline{R}$R)$\underline{R}$ and 3-$\underline{R}$RS through middle joint angles reversal avoids link interference.

2) Spatial 3-$\underline{R}$RS manipulator is designed with three force balanced limbs and two moment balancing flywheels.

3) Structural adaption and motion planning are integrated to seek optimization for minimum energy consumption in a spatial manipulator. (example in 3-RRS)

4) The combination of two balanced interference-free manipulators provides a higher DOF balanced manipulator of large workspace. The DOF and structural adaption from the two individual manipulators are combined.

7.2.2 Re-design of 3-PRS and 3-RPS Deployable Manipulators

1) The 3-PRS and 3-RPS are re-designed with deployable function (lie-flat feature).

2) The 3-RPS hybrid energy harvester harvests wind loads on solar panel through leg deformations.

3) Minimum platform height algorithm rapidly checks eligibility of possible pose of workspace and shortens the optimization time. (example in 3-RPS)

4) Jacobian matrix transformation for stiffness evaluation in any direction. (example in 3-RPS)

7.2.3 Novel Design of 5-DOF and 6-DOF Deployable Manipulators

1) The 6-DOF (2-RR)UU limb is designed. It has large workspace and is deployable which serves as limbs for deployable 6-DOF 3-[(2-RR)UU] and 5-DOF PRPU/2-[(2-RR)UU].

2) Link interference is avoided as each limb is distributed in a mobile vertical plane and multiple horizontal layers. Link boundary offset method rapidly detects link interference for links on a same horizontal layer. (example in PRPU/2-[(2-RR)UU])

3) Jacobian matrix is modified for stiffness evaluation in any direction. (example in 3-[(2-RR)UU])

7.3 Future Research

1.a) The 6-DOF dynamically balanced machine combined by (2-$\underline{RR}$)$\underline{R}$ and 3-$\underline{R}$RS manipulators could be optimized for minimal energy consumption with the five relocatable base joins and motion planning

1.b) The active force compensation may need to be considered for operations when there includes large amount material addition or removal which may affect the dynamic balancing.

2.a) The piezo chips on the legs of the 3-R$\underline{P}$S hybrid harvester can harvest mechanical energy and sense the deformation as well. Machine learning algorithm needs to be developed to recognize the loading condition on the solar panel through piezo chips. This could save the sensor cost of the model and help to promote the hybrid harvesters to the commercial market.

2.b) A family of high DOF deployable can be designed with the design principles given in above chapters. Thanks to the composition of vertical and horizontal multiple planar linkages, the possibilities of linkage of a given DOF might be generated with computer program in each plane. The computing algorithm will need to be developed.

2.c) The family could be further classified to groups of sub-class manipulators where their unique properties will be analyzed to match certain categories of applications.

7.4 An Outlook of the Clean Powered Robotic Systems

The figure 7.4.1 shows a system of robots.

deployable manipulator

factory
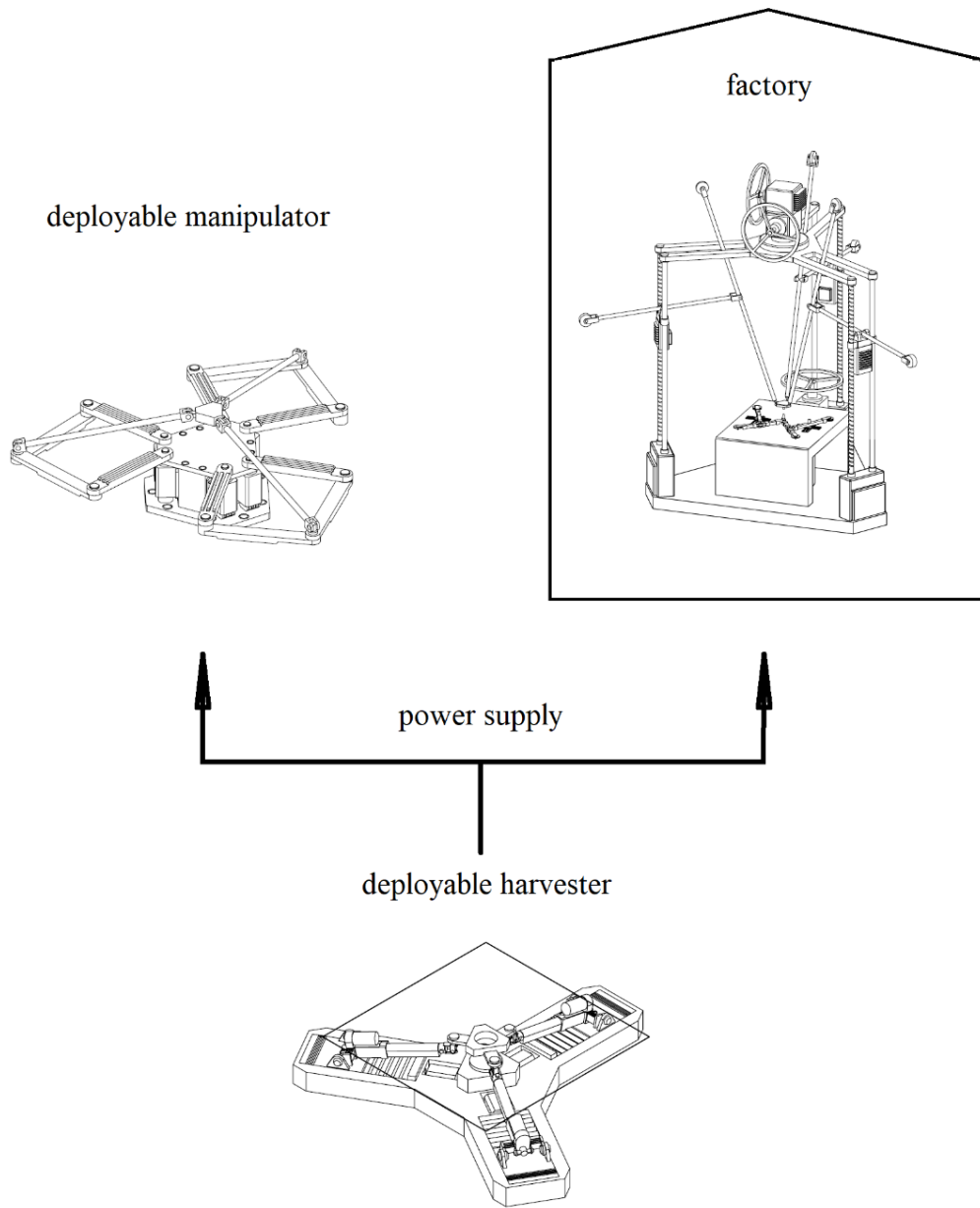
power supply

deployable harvester

Figure 7.4.1 A robotic system of balanced and deployable manipulators green energy powered.

With the manipulators developed in the previous chapters, one could have an outlook to the future

indoor and outdoor robotic system that run on solar and wind energy.

The balanced manipulator is working in the factory that has low noise and vibration, and is energy saving.

The deployable manipulator is serving the drones and unmanned vehicles which are transporting parts between factories. The deployable harvesters supply clean energy to the above manipulators. The deployable manipulators and deployable harvesters can lie flat to protect themselves from natural disasters.

This robotic system is operating in a green way and working harmoniously with nature.

References

[1]   Zamalloa, I., Kojcev, R., Hernandez, A., Muguruza, I., Usategui, L., Bilbao, A., Mayoral, V., 2017, "Dissecting Robotics - Historical Overview and Future Perspectives," ArXiv 2017.

[2]   Royakkers, L., and Van Est, R., 2015, "A Literature Review on New Robotics: Automation from Love to War," International Journal of Social Robotics, 7(5), pp. 549-570.

[3]   Ting, C., Yeo, W., King, Y., Yea Dat, C., Lee, J., and Khaw, W., 2014, "Humanoid Robot: A Review of the Architecture, Applications and Future Trend," Research Journal of Applied Sciences, Engineering and Technology, 7(7), pp. 1364-1369.

[4]   Angeles, J., 2007, Fundamentals of Robotic Mechanical Systems: Theory, Methods, and Algorithms, Springer, New York.

[5]   Raibert, M., Blankespoor, K., Nelson, G., Playter, R., 2008, "BigDog, the Rough-Terrain Quadruped Robot," IFAC Proceedings Volumes, 41(2), pp. 10822-10825.

[6]   Hung, S., Liu, C., Tsai, A., and Lin, T., 2008, "Design and Implementation of an Intelligent Robotic Fish," 2008 IEEE Workshop on Advanced Robotics and Its Social Impacts, Taipei, August 23-25, 2008, pp. 1-5.

[7]   Xu, Y., and Wang, H., 2013, "Flying Robot with Undulating Wings," IFAC Proceedings Volumes, 46(30), pp. 181-186.

[8]   Hodgins, J., 2018, "H-Delta: Design and Applications of a Novel 5 Degree of Freedom Parallel Robot," Ph.D. dissertation, University of Ontario Institute of Technology, Oshawa, ON.

[9]   Arns, M., 2019, "Novel Reconfigurable Delta Robot Dual-functioning as Adaptive Landing Gear and Manipulator," Master thesis, York University, Toronto, ON.

[10]   "The Shuttle Remote Manipulator System -- The Canadarm," accessed 2019, https://www.ieee.ca/millennium/canadarm/canadarm_technical.html

[11]   Gasparetto, A., and Scalera, L., 2019, "A Brief History of Industrial Robotics in the 20th Century," Advances in Historical Studies, 8(1), pp. 24-35.

[12]   Nam, H., Riviere, E., and Verlinden, O., 2016, "Milling Simulations with a 3-DOF Flexible Planar Robot," International Journal of Mechanical, Aerospace, Industrial, Mechatronic and Manufacturing Engineering, 10(9).

[13]   Subhashini, P., Raju, N., and Venkata Rao, G., 2014, "Modeling, Simulation and Analysis of a SCARA Robot for Deburring of Circular Components," ARPN Journal of Engineering and Applied Sciences, 9(4), pp. 398-404.

[14]   Zhang, D., 2010, Parallel Robotic Machine Tools, Springer, New York.

[15]   Hamdoun, O., Baghli, F., and Bakkali, L., 2015, "Inverse Kinematic Modeling of 3RRR Parallel Robot," 22ème Congrès Français de Mécanique, Lyon, France, August 24-28.

[16]   Patel, Y., and George, P., 2012, "Parallel Manipulators Applications-A Survey," Modern Mechanical Engineering, 2(3), pp. 57-64.

[17]   Küçük, S., 2012, Serial and parallel robot manipulators: Kinematic dynamics, control and Optimization, IntechOpen.

[18]   Stewart, D., 1965, "A Platform with Six Degrees of Freedom," Proceedings of the Institution of Mechanical Engineers, 180(1), pp. 371-386.

[19]   Qian, S., Zi, B., Shang, W., and Xu, Q., 2018, "A Review on Cable-driven Parallel Robots," Chinese Journal of Mechanical Engineering, 31(66).

[20]   Mohamed, M., and Gosselin, C., 2005, "Design and Analysis of Kinematically Redundant Parallel Manipulators with Configurable Platforms," IEEE Transactions on Robotics, 21(3), pp. 277-287.

[21]   Jin, X., Fang, Y., Qu, H., and Guo, S., 2018, "A Class of Novel 4-DOF and 5-DOF Generalized Parallel Mechanisms with High Performance," Mechanism and Machine Theory, Volume 120, February 2018, pp. 57-72.

[22]   Zeng, Q., and Ehmann, K., 2014, "Design of Parallel Hybrid-loop Manipulators with Kinematotropic Property and Deployability," Mechanism and Machine Theory, Volume 71, January 2014, pp. 1-26.

[23]   Tian, C., Fang, Y., and Guo, S., 2016, "Structural Synthesis of a Class of 2R2T Hybrid Mechanisms," Chinese Journal of Mechanical Engineering, 29(4), pp. 703-709.

[24]   Tian, C., Fang, Y., and Ge, Qi., 2017, "Structural Synthesis of Parallel Manipulators with Coupling Sub-chains," Mechanism and Machine Theory, 118, December 2017, pp. 84-99.

[25]   Gosselin, C., 2008, "Gravity Compensation, Static Balancing and Dynamic Balancing of Parallel Mechanisms," Smart Devices and Machines for Advanced Manufacturing. Wang, L., and Xi, J., eds., Springer, London.

[26]   Yang, Z., and Zhang, D., (under peer-review/revision 2019), "Novel Planar Balanced Adaptive (2-RR)R Parallel Manipulator," International Journal of Robotics and Automation.

[27]   Yang, Z., and Zhang, D., (accepted in February 2019), "Energy Optimal Adaption and Motion Planning of a 3-RRS Balanced Manipulator," International Journal of Robotics and Automation.

[28]   Yang, Z., and Zhang, D., 2017, "Reconfigurable 3-PRS Parallel Solar Tracking Stand," Proceedings of the ASME 2017 International Design Engineering Technical Conferences and Computers and Information in Engineering Conference, Cleveland, Ohio, USA, August 6-9, 2017, ASME Paper No. DETC2017-67275.

[29]   Yang, Z., and Zhang, D., 2018, "Hybrid Harvester 3-RPS Robotic Parallel Manipulator," 2018 2nd International Conference on Artificial Intelligence Applications and Technologies (AIAAT 2018), Shanghai, China, August 8-10, 2018.

[30]   Yang, Z., and Zhang, D., 2018, "Novel Design of a 3-RRUU 6-DOF Parallel

Manipulator", 2018 4th International Conference on Mechanical and Aeronautical

Engineering (ICMAE 2018), Bangkok, Thailand, December 13-16, 2018.

[31]   Yang, Z., and Zhang, D., 2019, "Novel Design of a 3T2R 5-DOF Parallel

Manipulator", Proceedings of the ASME 2019 International Design Engineering

Technical Conferences and Computers and Information in Engineering Conference,

Anaheim, CA, USA, August 18-21, 2019, ASME Paper No. IDETC2019-97088.

[32]   Yang, T., Liu, A., Shen, H., Hang, L., Luo, Y., and Jin, Q., 2018, Topology Design

of Robot Mechanisms, Springer, Singapore.

[33]   Huang, T., Zhao, D., Yin, F., Tian, W., and Chetwynd, D., 2019, "Kinematic

Calibration of a 6-DOF Hybrid Robot by Considering Multicollinearity in the

Identification Jacobian," Mechanism and Machine Theory, Volume 131, January

2019, pp. 371-384.

[34]   Zhang, D., and Wang, L., 2005, "Conceptual Development of an Enhanced Tripod

Mechanism for Machine Tool," Robotics and Computer-Integrated Manufacturing,

Volume 21, Issues 4-5, pp. 318-327.

[35]   Li, J., 2009, "Design of 3-DOF Parallel Manipulators for Micro-motion

Applications," Master Thesis, University of Ontario Institute of Technology,

Oshawa, ON.

[36]   Gogu, G., 2005, "Mobility of Mechanisms: A Critical Review," Mechanism and

Machine Theory, 40(9), pp. 1068-1097.

[37]   Gogu, G., 2005, "Chebychev–Grübler–Kutzbach's Criterion for Mobility Calculation of Multi-loop Mechanisms Revisited via Theory of Linear Transformations," European Journal of Mechanics - A/Solids, 24(3), pp. 427-441.

[38]   Zhao, J., Zhou, K., and Feng, Z., 2004, "A Theory of Degrees of Freedom for Mechanisms," Mechanism and Machine Theory, 39(6), pp. 621-643.

[39]   Huang, Z., Liu, J., and Li, Y., 2011, "150-year Unified Mobility Formula Issue," Journal of Yanshan University, 35(1), pp. 1-14.

[40]   Angeles, J., and Gosselin, C., 1988, "Determination Du Degre De Liberte Des Chaines Cinematique," Transactions of the Canadian Society for Mechanical Engineering, Volume 12, No. 4, pp. 219-226.

[41]   Gosselin, C., 1990, "Stiffness Mapping for Parallel Manipulators," IEEE Transactions on Robotics and Automation, Volume 6, Issue 3, pp. 377-382.

[42]   Yang, D., Xiong, J., and Yang, X., 2008, "A Simple Method to Calculate Mobility with Jacobian," Mechanism and Machine Theory, 43(9), pp. 1175-1185.

[43]   Qu, S., Li, R., and Bai, S., 2017, "Type Synthesis of 2T1R Decoupled Parallel Mechanisms Based on Lie Groups and Screw Theory," Mathematical Problems in Engineering, Volume 2017, pp. 1-11.

[44]   Gosselin, C., 1988, "Kinematic Analysis, Optimization and Programming of Parallel Robotic Manipulators," Ph.D. dissertation, McGill University, Montreal, QC.

[45]   Tsai, L., 2000, Mechanism Design: Enumeration of Kinematic Structures According to Function, CRC Press.

[46]   Wang, X., Baron, L., and Cloutier, G., 2008, "Topology of Serial and Parallel Manipulators and Topological Diagrams," Mechanism and Machine Theory, 43(6), pp. 754-770.

[47]   Gao, F., Yang, J., and Ge, Q., 2011, "Type Synthesis of Parallel Mechanisms Having the Second Class GF Sets and Two Dimensional Rotations," Journal of Mechanisms and Robotics Transactions of the ASME, 3(1).

[48]   Landure, L., and Gosselin, C., 2018, "Kinematic Analysis of a Novel Kinematically Redundant Spherical Parallel Manipulator," Journal of Mechanisms and Robotics Transactions of the ASME, 10(2).

[49]   Li, Q., Chai, X., and Chen, Q., 2017, "Review on 2R1T 3-DOF Parallel Mechanisms," Chinese Science Bulletin, Volume 62, pp. 1507-1519.

[50]   Siciliano, B., 1999, "The Tricept Robot: Inverse Kinematics, Manipulability Analysis and Closed-loop Direct Kinematics Algorithm," Robotica, Volume 17, pp. 437-445.

[51]   Chen, X., Liu, X., Xie, F., and Su, Tao., 2014, "A Comparison Study on Motion/Force Transmissibility of Two Typical 3-DOF Parallel Manipulators: The Sprint Z3 and A3 Tool Heads," International Journal of Advanced Robotic Systems, pp. 1-10.

[52]   Zhang, D., and Gosselin, C., 2002, "Kinetostatic Analysis and Design Optimization of the Tricept Machine Tool Family," Journal of Manufacturing Science and Engineering, Transactions of the ASME, 124(3).

[53]   Gao, Z., and Zhang, D., 2014, "Performance Analysis, Mapping, and Multiobjective Optimization of a Hybrid Robotic Machine Tool," IEEE Transactions on Industrial Electronics, Volume 62, Issue 1, pp. 423-433.

[54]   Bi, Z., and Jin, Y., 2011, "Kinematic Modeling of Exechon Parallel Kinematic Machine," Robotics and Computer-Integrated Manufacturing, 27(1), pp. 186-193.

[55]   Mejia, L., Simas, H., and Martins. D., 2015, "Force Capability in General 3 DoF Planar Mechanisms," Mechanism and Machine Theory, Volume 91, pp. 120-134.

[56]   Qin, Y., Hai, Y., Zhou, C., and Cao, Y., 2015, "Structural Synthesis of 3T2R Five-Degree-of-Freedom (DoF) Hybrid Mechanism," The 5th Annual IEEE International Conference on Cyber Technology in Automation, Control and Intelligent Systems, Shenyang, China, June 8-12, 2015, pp. 65-70.

[57]   Lu, Y., and Dai, Z., 2016, "Dynamics Model of Redundant Hybrid Manipulators Connected in Series by Three or More Different Parallel Manipulators with Linear Active Legs," Mechanism and Machine Theory, Volume 103, pp. 222-235.

[58]   Chablat, D., Wenger, P., and Angeles, J., 1998, "The Kinematic Design of a 3-dof Hybrid Manipulator," Integrated Design and Manufacturing in Mechanical Engineering, Compiègne, France, pp.1-8.

[59]   Yeshmukhametov, A., Kalimoldayev, M., Mamyrbayev, O., and Amirgaliev, Y., 2017, "Design and Kinematics of Serial/Parallel Hybrid Robot," 2017 3rd International Conference on Control, Automation and Robotics (ICCAR), Nagoya, Japan, April 24-26, 2017, pp. 162-165.

[60]   Lin, R., Guo, W., and Gao, F., 2016, "Type Synthesis of a Family of Novel Four, Five, and Six Degrees-of-Freedom Sea Lion Ball Mechanisms with Three Limbs," Journal of Mechanisms and Robotics Transactions of the ASME, 8(2).

[61]   Behi, F., 1988, "Kinematic Analysis for a Six-Degree-of-Freedom 3-PRPS Parallel Mechanism," IEEE Journal on Robotics and Automation, 4(5), pp. 561-565.

[62]   Simaan, N., Glozman, D., and Shoham, M., 1998, "Design Considerations of New Six Degrees-of-Freedom Parallel Robots," Proceedings of 1998 IEEE International Conference on Robotics and Automation, Leuven, Belgium, May 1998, pp. 1327-1333.

[63]   Alizade, R., Tagiyev, N., and Duffy, J., 1994, "A Forward and Reverse Displacement Analysis of a 6-DOF In-Parallel Manipulator," Mechanism and Machine Theory, Volume 29, Issue 1, pp. 115-124.

[64]   Kim, J., Park, F. C., Ryu, S. J., Kim, J., Hwang, J. C., Park, C., and Iurascu, C. C., 2001, "Design and Analysis of a Redundantly Actuated Parallel Mechanism for Rapid Machining," IEEE Transactions on Robotics and Automation, 17(4), pp. 423-434.

[65]   Chen, C., Gayral, T., Caro, S., Chablat, D., Moroz, G., and Abeywardena, S., 2012, "A Six Degree of Freedom Epicyclic-Parallel Manipulator," Journal of Mechanisms and Robotics, Transactions of the ASME, 4(4).

[66]   Tahmasebi, F., and Tsai, L., 1992, "Jacobian and Stiffness Analysis of a Novel Class of Six-DOF Parallel Mini Manipulators", 22nd ASME Biennial Mechanisms Conference, Scottsdale, AZ, September 1992.

[67]   Li, W., and Angeles, J., 2017, "A Novel Three-loop Parallel Robot with Full Mobility: Kinematics, Singularity, Workspace, and Dexterity Analysis," Journal of Mechanisms and Robotics, Transactions of the ASME, 9(5).

[68]   Monsarrat, B., and Gosselin, C., 2003, "Workspace Analysis and Optimal Design of a 3-Leg 6-DOF Parallel Platform Mechanism," IEEE Transactions on Robotics and Automation, 19(6), pp. 954-966.

[69]   Yang, G., Chen, I., Chen, W., and Lin, W., 2004, "Kinematic Design of a Six-DOF Parallel-Kinematics Machine with Decoupled-Motion Architecture," IEEE Transactions on Robotics and Automation, 20(5), pp. 876-884.

[70]   Lee, S., and Kim, S., "Kinematic feature analysis of parallel manipulator systems," Proceedings of IEEE/RSJ International Conference on Intelligent Robots and Systems (IROS'94), Munich, Germany, 1994, Volume 2, pp. 1421-1428.

[71]   Guo, S., and Qu, H., 2016, Structural Synthesis of Redundant Parallel Robots and Its Applications, Science Press China, Beijing, China.

[72]   Luces, M., and Mills, J., and Benhabib, B., 2017, "A Review of Redundant Parallel Kinematic Mechanisms," Journal of Intelligent & Robotic Systems, 86(2), pp. 175-198.

[73]   Gosselin, C., & Schreiber, L., 2018, "Redundancy in Parallel Mechanisms: A Review," Applied Mechanics Reviews, Transactions of the ASME, 70(1).

[74]   Fahimi, F., 2009, Autonomous Robots: Modeling, Path Planning, and Control. Springer, New York.

[75]   Gosselin, C., Laliberte, T., and Veillette, Audrey., 2015, "Singularity-Free Kinematically Redundant Planar Parallel Mechanisms with Unlimited Rotational Capability," IEEE Transactions on Robotics, 31(2), pp. 457-467.

[76]   Santos, J., Rocha, D., and Silva, M., 2014, "Performance Evaluation of Kinematically Redundant Planar Parallel Manipulators," ABCM Symposium Series in Mechatronics, Volume 6, pp. 391-401.

[77]   Varalakshmi, K., and Srinivas, J., 2014, "Optimized Configurations of Kinematically Redundant Planar Parallel Manipulator following a Desired Trajectory," Procedia Technology, Volume 14, pp. 133-140.

[78]   Maraje, S., Nurahmi, L., and Caro, S., 2016, "Operation Modes Comparison of a Reconfigurable 3-PRS Parallel Manipulator Based on Kinematic Performance," ASME 2016 International Design Engineering Technical Conferences and Computers and Information in Engineering Conference, Charlotte, North Carolina, USA, August 21-24, 2016, ASME Paper No. DETC2016-59804.

[79]   Kotlarski, J., Abdellatif, H., and Heimann, B., 2008, "Improving the Pose Accuracy of a Planar 3RRR Parallel Manipulator Using Kinematic Redundancy and Optimized Switching Patterns," 2008 IEEE International Conference on Robotics and Automation, Pasadena, CA, USA, May 19-23, 2008, pp. 3863-3868.

[80]   Liu, H., Huang, T., Kecskeméthy, A., and Chetwynd, D., 2015, "Force / Motion / Stiffness Transmissibility Analyses of Redundantly Actuated and Overconstrained Parallel Manipulators," The 14th IFToMM World Congress, Taipei, Taiwan, October 25-30, 2015.

[81]   Mueller, A., 2008, "Redundant Actuation of Parallel Manipulators," Parallel Manipulators, Towards New Applications. Wu, P., eds., I-Tech Education and Publishing, Vienna, Austria, pp. 87-108.

[82]   Cheng, H., Liu, G., Yiu, Y., Xiong, Z., and Li, Z., 2001, "Advantages and Dynamics of Parallel Manipulators with Redundant Actuation," Proceedings of the 2001 IEEE/RSJ International Conference on Intelligent Robots and Systems, Maui, Hawaii, USA, Oct 29-Nov 03, 2001, pp. 171-176.

[83]   Wu, J., Chen, X., Li, T., and Wang, L., 2013, "Optimal Design of a 2-DOF Parallel Manipulator with Actuation Redundancy Considering Kinematics and Natural Frequency," Robotics and Computer-Integrated Manufacturing, 29(1), pp. 80-85.

[84]   Arakelian, V., 2015, "Optimum Shaking Force Balancing of Planar 3-RRR Parallel Manipulators by Means of an Adaptive Counterweight System," Journal of Robotics and Mechanical Engineering Research, 1(2), pp. 36-41.

[85]   Dresig, H., and Dien, N., 2011, "Complete Shaking Force and Shaking Moment Balancing of Mechanisms Using a Moving Rigid Body," TECHNISCHE MECHANIK, 31(2), pp. 121-131.

[86]   Coppola, G., 2014, "Advances in Parallel Robotics for Flexible and Reconfigurable Manufacturing," Ph.D. dissertation, University of Ontario Institute of Technology, Oshawa, ON.

[87]   Coppola, G., Zhang, D., and Liu, K., 2014, "A New Class of Adaptive Parallel Robots," Journal of Mechanisms and Robotics, Transactions of the ASME, 6(4).

[88]   Bi, Z., Lin, Y., and Zhang, W., 2010, "The General Architecture of Adaptive Robotic Systems for Manufacturing Applications," Robotics and Computer-Integrated Manufacturing, 26(5), pp. 461-470.

[89]   Zhang, T., Zhang, W., and Gupta, M., 2018, "An Underactuated Self-Reconfigurable Robot and The Reconfiguration Evolution," Mechanism and Machine Theory, Volume 124, pp. 248-258.

[90]   Li, J., Wang, J., Chou, W., Zhang, Y., Wang, T., and Zhang, Q., 2001, "Inverse Kinematics and Dynamics of the 3-RRS Parallel Platform," Proceeding of the 2001 IEEE International Conference on Robotics & Automation, Seoul, Korea, May 21-26, 2001, pp. 2506-2511.

[91]   Li, Y., and Xu, Q., 2004, "Kinematics and Stiffness Analysis for a General 3-PRS Spatial Parallel Mechanism", ROMANSY Conference 2004, Montreal, Canada, June 14-18, 2004.

[92]   Babu, S., Raju, V., and Ramji, K., 2013, "Design for Optimal Performance of 3-RPS Parallel Manipulator Using Evolutionary Algorithms", Transactions of the Canadian Society for Mechanical Engineering, Vol. 37, No. 2, pp. 135-160.

[93]   "D'Alembert's Principle," accessed 2016, https://en.wikipedia.org.

[94]   Rahmat Abadi, B., Taghvaei, S., and Vatankhah, R., 2016, "Optimal Motion Planning of a Planar Parallel Manipulator with Kinematically Redundant Degrees of Freedom," Transactions of Canadian Society for Mechanical Engineering, 40(3), pp. 383-397.

[95]   "MathWorks Documentations: Mechanical Dynamics," accessed 2017, https://www.mathworks.com/help/physmod/sm/mech/ug/mechanical-dynamics.html.

[96]   Sun, Z., Zhang, B., Cheng, L., and Zhang, W., 2011 "Application of the Redundant Servomotor Approach to Design of Path Generator with Dynamic Performance Improvement," Mechanism and Machine Theory, 46 (11), pp. 1784–1795.

[97]   Hu, J., Zhang, X., and Zhan, J., 2008, "Trajectory Planning of a Novel 2-DoF High-Speed Planar Parallel Manipulator," Intelligent Robotics and Applications. ICIRA 2008. Lecture Notes in Computer Science. Xiong, C., Huang, Y., Xiong, Y., and Liu, H., eds, Springer, Berlin.

[98]   Abdellatif, H., and Heimann, B., 2005, "Adapted Time-Optimal Trajectory Planning for Parallel Manipulators with Full Dynamic Modelling," Proceedings of the 2005

IEEE International Conference on Robotics and Automation, Barcelona, Spain, April 2005, pp. 411-416.

[99]   Lorenz, M., Paris, J., Haschke, T., Schöler, F., Hüsing, M., and Corves, B., 2017, "A Study on Efficient Motion Design for Redundantly Actuated Parallel Kinematic Manipulators," 2017 IEEE/RSJ International Conference on Intelligent Robots and Systems (IROS), Vancouver, BC, Canada, September 24-28, 2017, pp. 5638-5645.

[100]   Mei, Y., Lu, Y., Hu, Y., and Lee, C., 2004, "Energy-efficient Motion Planning for Mobile Robots," Proceedings of the 2004 IEEE International Conference on Robotics and Automation, New Orleans, LA, USA, April 2004, pp. 4344-4349.

[101]   "Polynomial Interpolation," accessed 2017, http://wikipedia.org.

[102]   "Genetic Algorithm: Find Global Minima for Highly Nonlinear Problems," accessed 2016, https://www.mathworks.com/discovery/genetic-algorithm.html.

[103]   Chong, E., and Zak, S., 2013, An Introduction to Optimization (Fourth Edition), John Wiley & Sons, Canada.

[104]   "Multi-objective Optimization," accessed 2016, https://en.wikipedia.org.

[105]   Zhang, D., and Wei, B., 2016, Dynamic Balancing of Mechanisms and Synthesizing of Parallel Robots, Springer International Publishing.

[106]   Wei, B., 2016, "Performance Improvement for Robotic Mechanisms by: Synthesis Design, Dynamic Balancing and Adaptive Control Techniques," Ph.D. dissertation, University of Ontario Institute of Technology, Oshawa, ON.

[107]   Zhang, D., and Wei, B., 2015, "Dynamic Balancing of Parallel Manipulators Through Reconfiguration," Proceedings of the ASME 2015 Dynamic Systems and Control Conference, Columbus, Ohio, USA, October 28-30, 2015, ASME Paper No. DSCC2015-9669.

[108]   Zhang, D., and Wei, B., 2017, "Dynamic Balancing of Robotic Mechanisms via Reconfiguration and Integration Design," International Journal of Robotics and Automation, 32(6), pp. 551-559.

[109]   Arakelian, V., and Smith, M., 2005, "Shaking Force and Shaking Moment Balancing of Mechanisms: A Historical Review with New Examples," Journal of Mechanical Design, Transactions of the ASME, 127(2), pp. 334-339.

[110]   Ricard, R., and Gosselin, C., 2000, "On the Development of Reactionless Parallel Manipulators," Proceedings of DETC'00 ASME 2000 Design Engineering Technical Conferences and Computers and Information in Engineering Conference, Baltimore, Maryland, September 10-13, 2000, ASME Paper No. DETC2000/MECH-14098.

[111]   Wu, Y., and Gosselin, C., 2005, "Design of Reactionless 3-DOF and 6-DOF Parallel Manipulators Using Parallelepiped Mechanisms," IEEE Transactions on Robotics, 21(5), pp. 821-833.

[112]   Coppola, G., Zhang, D., Liu, K., and Gao, Z., 2013, "Design of Parallel Mechanisms for Flexible Manufacturing with Reconfigurable Dynamics," Journal of Mechanical Design, Transactions of the ASME, 135(7).

[113]   Ouyang, P., and Zhang, W., 2005, "Force Balancing of Robotic Mechanisms Based on Adjustment of Kinematic Parameters," Journal of Mechanical Design, Transactions of the ASME, 127(3), pp. 433-440.

[114]   Buganza, A., and Acevedo, M., 2011, "Dynamic Balancing of a 2-DOF 2 RR Planar Parallel Manipulator by Optimization," 13th World Congress in Mechanism and Machine Science, Guanajuato, Mexico, June 19-25, 2011.

[115]   Wang, K., Luo, M., Mei, T., Zhao, J., and Cao, Y., 2013, "Dynamics Analysis of a Three-DOF Planar Serial-Parallel Mechanism for Active Dynamic Balancing with Respect to a Given Trajectory," International Journal of Advanced Robotic Systems, Volume 10.

[116]   Wijk, V., and Herder, J., 2010, "Active Dynamic Balancing Unit for Controlled Shaking Force and Shaking Moment Balancing," Proceedings of the ASME Design Engineering Technical Conference, Montreal, Quebec, Canada, Aug. 15-18, 2010, ASME Paper No. DETC2010-28423.

[117]   Arakelian, V., and Smith, M., 2008, "Design of Planar 3-DOF 3-RRR Reactionless Parallel Manipulators," Mechatronics, 18(10), pp. 601-606.

[118]   Wijk, V., and Herder, J., 2008, "Dynamic Balancing of Mechanisms by using an Actively Driven Counter-Rotary Counter-Mass for Low Mass and Low Inertia," Proceedings of the Second International Workshop on Fundamental Issues and Future Research Directions for Parallel Mechanisms and Manipulators, Montpellier, France, September 21-22, 2008, pp. 241-251.

[119]   "Tropical Storm Risk (TSR)," accessed 2017, http://www.tropicalstormrisk.com.

[120]   "Solar Field in Ontario Sees Damage Following Winter Storm," last modified November 26, 2016, accessed 2017, http://13wham.com/news/top-stories/solar-field-in-ontario-sees-damage-following-winter-storm.

[121]   Thurston, C., 2015, "Ensuring Your Solar Array Doesn't Get Caught in the Wind," Renewable Energy World, 18(4).

[122]   Zhao, D., Zhao, J., and Yan, Z., 2016, "Planar Deployable Linkage and Its Application in Overconstrained Lift Mechanism," Journal of Mechanisms and Robotics, Transactions of the ASME, 8(2).

[123]   Liu, X., Wang, J., and Pritschow, G., 2005, "A New Family of Spatial 3-DoF Fully-Parallel Manipulators with High Rotational Capability," Mechanism and Machine Theory, Volume 40, Issue 4, 2005, Pages 475-494.

[124]   Liu, X., Wang, J., and Kim, J., 2009, "A New Family of Spatial 3-DOF Parallel Manipulators with Two Translational and One Rotational DOFs," Robotica, 27(2), pp. 241-247.

[125]   Li, B., Yu, H., Deng, Z., Yang, X., and Hu, H., 2010, "Stiffness Modeling of a Family of 6DoF Parallel Mechanisms with Three Limbs Based on Screw Theory," Journal of Mechanical Science and Technology, 24(1), pp. 373-382.

[126]   Merlet, J., 1992, "Geometrical Determination of the Workspace of a Constrained Parallel Manipulator", Advances in Robot Kinematics, Ferrare, September 7-9, 1992, pp. 326-329.

[127] Zaidie Abdul Majid, M., Huang, Z., and Yao, Y., 1999, "Workspace Analysis of a New Parallel Manipulator," Transactions of NAMRI/SME, Volume XXVII, 1999, pp. 305-310.

[128] Merlet, J., Gosselin, C., and Mouly, N., 1998, "Workspaces of Planar Parallel Manipulators," Mechanism and Machine Theory, Volume 33, Issues 1-2, pp. 7-20.

[129] Lumelsky, V., 1985, "On Fast Computation of Distance Between Line Segments," Information Processing Letters, Volume 21, Issue 2, pp. 55-61.

[130] Merlet, J., 1995, "Determination of the Orientation Workspace of Parallel Manipulators," Journal of Intelligent and Robotic Systems, Volume 13, Issue 2, pp. 143-160.

[131] Zhang, F., Zhu, Y., Furukawa, T., and Song, W., 2015, "Kinematic Analysis of a Partially Decoupled 3-DOF Parallel Wrist," Journal of Robotics, 2015(9), pp. 1-9.

[132] Tao, Z., and An, Q., 2013, "Interference Analysis and Workspace Optimization of 3-RRR Spherical Parallel Mechanism," Mechanism and Machine Theory, Volume 69, pp. 62-72.

[133] Sen, D., and Joshi, V., 2004, "Issues in Geometric Synthesis of Mechanisms," Mechanism and Machine Theory, Volume 39, Issue 12, pp. 1321-1330.

[134] Ling, Z., and Chase, T., 1996, "A Priori Geometric Design of an Interference Free Complex Planar Mechanism," Mechanism and Machine Theory, Volume 31, Issue 4, pp. 513-524.

[135] Schreiber, L., and Gosselin, C., 2017, "Passively Driven Redundant Spherical Joint with Very Large Range of Motion," Journal of Mechanisms and Robotics, Transactions of the ASME, 9(3).

[136] Talaba, D., 2012, "The Angular Capacity of Spherical Joints Used in Mechanisms with Closed Loops and Multiple Degrees of Freedom," Robotics and Computer-Integrated Manufacturing, Volume 28, Issue 5.

[137] Hudgens, J., and Arai, T., 1993, "Planning Link-interference-free Trajectories for a Parallel Link Manipulator," Proceedings of IECON '93 - 19th Annual Conference of IEEE Industrial Electronics, Maui, Hawaii, USA, Nov. 15-19, 1993, pp. 1506-1511.

[138] Alici, G., and Shirinzadeh, B., 2004, "Optimum Dynamic Balancing of Planar Parallel Manipulators," Proceedings of the 2004 IEEE International Conference on Robotics and Automation, New Orleans, LA, USA, April 26-May 1, 2004, pp. 4527-4532.

[139] Luo, L., Yuan, C., Yan, R., Yuan, Q., Wu, J., Shin, K., and Han, C., 2015, "Trajectory Planning for Energy Minimization of Industry Robotic Manipulators Using the Lagrange Interpolation Method," International Journal of Precision Engineering and Manufacturing, 16(5), pp. 911-917.

[140] Gregory, J., Olivares, A., and Staffetti, E., 2013, "Energy-Optimal Trajectory Planning for Planar Underactuated RR Robot Manipulators in the Absence of Gravity," Abstract and Applied Analysis, Volume 2013.

[141] "Back EMF in a Motor," accessed 2016, https://www.researchgate.net.

[142] Gu, S., 2007, Fundamentals of Electrical Machines and Drives, 4th Edition, China Machine Press, Beijing.

[143] "Rotation Matrix," accessed 2017, http://en.wikipedia.org.

[144] Tudorache, T., and Kreindler, L., 2010, "Design of a Solar Tracker System for PV Power Plants," Acta Polytechnica Hungarica, Vol. 7, No. 1, pp. 23-39.

[145] "How to Create a Solar Panel that Tracks the Sun," accessed 2016, https://www.pc-control.co.uk/howto_tracksun.htm.

[146] Gnanarathinam, D., Sundaramurthy, S., and Wahi, A., 2015, "Design and Implementation of a Dual Axis Solar Tracking System," International Journal for Research in Applied Science and Engineering Technology, Vol. 3, Issue X.

[147] Cammarata, A., 2014, "Optimized Design of a Large-workspace 2-DOF Parallel Robot for Solar Tracking Systems," Mechanism and Machine Theory, Volume 83, pp. 175-186.

[148] "Design of Multiaxial Parallel Kinematic Machines with High Dynamic Capabilities," accessed 2016, http://www.ehu.eus/compmech/research-2/projects/design-of-multiaxial-parallel-kinematic-machines-with-high-dynamic-capabilities-dynamech/.

[149]   Shyam, R., and Ghosal, A., 2015, "Three-Degree-of-Freedom Parallel Manipulator to Track the Sun for Concentrated Solar Power Systems," Chinese Journal of Mechanical Engineering, 28(4), pp. 793-800.

[150]   Murphy, L., 1980, "Wind Loading on Tracking and Field Mounted Solar Collectors," Solar Energy Research Institute, United States. Doi: 10.2172/6889663.

[151]   Bhadurl, S., and Murphy, L., 1985, "Wind Loading on Solar Collectors," Solar Energy Research Institute, United States.

[152]   Liu, C., 2012, Foundations of MEMS, Second Edition, Prentice Hall, NJ.

[153]   Sirohi, J., and Mahadik, R., 2011, "Piezoelectric Wind Energy Harvester for Low-Power Sensors," Journal of Intelligent Material Systems and Structures, 22(18) pp. 2215-2228.

[154]   Tao, J., Viet, N., Carpinteri, A., and Wang, Q., 2017, "Energy harvesting from Wind by A Piezoelectric Harvester," Engineering Structures, 133(15), pp. 74-80.

[155]   Sirohi, J., and Mahadik, R., 2012, "Harvesting Wind Energy Using a Galloping Piezoelectric Beam," Journal of Vibration and Acoustics, Transactions of ASME, 134(1).

[156]   Yuan, G., and Wang, D., 2017, "A Piezoelectric Six-DOF Vibration Energy Harvester Based on Parallel Mechanism: Dynamic Modeling, Simulation, and Experiment," Smart Materials and Structures, 26(3).

[157]   Linear Table Alpha 15-B-155, HSB alpha Release: 12.12.2016.

[158] Linear Actuators: DLA Series and Accessories, 50 mm to 300 mm stroke 1000 N, Transmotec 2018.

[159] Budynas, R., and Nisbett, J., 2008, Shigley's Mechanical Engineering Design, Ninth Edition, McGraw-Hill, New York, pp.1013.

[160] "Material: Lead Zirconate Titanate (PZT)," accessed 2018, https://www.memsnet.org/material/leadzirconatetitanatepzt/.

[161] Campos, L., Bourbonnais, F., Boney, I., and Bigras, P., 2010, "Development of a Five-Bar Parallel Robot with Large Workspace," Proceedings of the ASME 2010 International Design Engineering Technical Conferences and Computers and Information in Engineering Conference, Montreal, Quebec, Canada, August 15-18, 2010, ASME Paper No. DETC2010-28962, pp. 917-922.

[162] Ferrari, D., and Giberti, H., 2014, "A Genetic Algorithm Approach to the Kinematic Synthesis of a 6-DOF Parallel Manipulator," 2014 IEEE Conference on Control Applications (CCA) Part of 2014 IEEE Multi-conference on Systems and Control, Antibes, France, October 8-10, 2014.

[163] Ayob, M., Zakaria, W., Jalani, J., and Tomari, M., 2015, "Inverse Kinematics Analysis of a 5-axis RV-2AJ Robot Manipulator," ARPN Journal of Engineering and Applied Sciences, Vol. 10, No. 18.

[164] Manjunath, T., 2007, "Kinematic Modelling and Maneuvering of A 5-Axes Articulated Robot Arm," International Journal of Mechanical, Aerospace, Industrial, Mechatronic and Manufacturing Engineering, Vol. 1, No. 4.

[165]   Masouleh, M., Gosselin, C., and Husty, M., 2011, "Forward Kinematic Problem of 5-RPUR Parallel Mechanisms (3T2R) with Identical Limb Structures," Mechanisms and Machine Theory, 46 (7), pp. 945-959.

[166]   Amine, S., Tale-Masouleh, M., Caro, S., Wenger, P., and Gosselin, C., 2011, "Singularity Analysis of 5-DOF Parallel Mechanisms 3T2R Using Grassmann-Cayley Algebra and Grassmann Line Geometry," 13th World Congress in Mechanism and Machine Science, Guanajuato, Mexico, June 19-25, 2011.

[167]   DC motors (15W~120W) DKM AC/DC Geared Motor and Gearhead, RAVEO.

Appendices

Appendix A: List of Papers during PhD Studies

Journal articles

[26]   Yang, Z., and Zhang, D., (under peer-review/revision 2019), "Novel Planar Balanced (2-RR)R Parallel Manipulator Adaptive for Energy Efficiency," International Journal of Robotics and Automation.

[27]   Yang, Z., and Zhang, D., (accepted in February 2019), "Energy Optimal Adaption and Motion Planning of a 3-RRS Balanced Manipulator," International Journal of Robotics and Automation.

Conference articles

[28]   Yang, Z., and Zhang, D., 2017, "Reconfigurable 3-PRS Parallel Solar Tracking Stand," Proceedings of the ASME 2017 International Design Engineering Technical Conferences and Computers and Information in Engineering Conference, Cleveland, Ohio, USA, August 6-9, 2017, ASME Paper No. DETC2017-67275.

[29]   Yang, Z., and Zhang, D., 2018, "Hybrid Harvester 3-RPS Robotic Parallel Manipulator," 2018 2nd International Conference on Artificial Intelligence Applications and Technologies (AIAAT 2018), Shanghai, China, August 8-10, 2018.

[30]   Yang, Z., and Zhang, D., 2018, "Novel Design of a 3-RRUU 6-DOF Parallel Manipulator", 2018 4th International Conference on Mechanical and Aeronautical Engineering (ICMAE 2018), Bangkok, Thailand, December 13-16, 2018.

[31]   Yang, Z., and Zhang, D., 2019, "Novel Design of a 3T2R 5-DOF Parallel Manipulator", Proceedings of the ASME 2019 International Design Engineering Technical Conferences and Computers and Information in Engineering Conference, Anaheim, CA, USA, August 18-21, 2019, ASME Paper No. IDETC2019-97088.

Note:

Paper [26] has been revised according to peer-review comments and has been resubmitted for peer-review. Currently it is waiting for decision from the journal.

Paper [27] is a journal paper. It has been accepted for publication and the final paper has been submitted. Currently it is waiting for publication.

Appendix B: Copyright Permission Letters

Permission for article [27].

Request for Permission to Use Copyrighted Material in a Dissertation

To whom it may concern,

I am Zhongxing Yang, a York University student preparing my dissertation for submission as part of the requirements of my doctoral degree in Mechanical Engineering. The title of my dissertation is: NOVEL DESIGN AND ANALYSIS OF PARALLEL ROBOTIC MECHANISMS.

The reason I am writing is to ask permission to include part or the whole of the following material in my dissertation:

Zhongxing Yang and Dan Zhang, (accepted in February 2019), "Energy Optimal Adaption and Motion Planning of a 3-RRS Balanced Manipulator," International Journal of Robotics and Automation.

The material will be fully cited in my dissertation.

My dissertation will be available on the internet for reference, study and/or copy. The electronic version of my dissertation will be accessible through the York University Libraries website and catalogue, and also through various web search engines. I will be granting Library and Archives Canada a non-exclusive license to reproduce, loan, distribute, or sell single copies of my dissertation by any means and in any form or format. These rights will in no way restrict republication of the material in any other form by you or by others authorized by you.

Could you please confirm by email that these arrangements meet with your approval. If you do not solely control the copyright in the material, please let me know as soon as possible. I would also appreciate any information you can provide about others to whom I should write to request permission.

If you would like to confirm permission by email, you can do so by signing and completing the information below and send me this signed and completed letter. My email address is zxyang@yorku.ca.

Sincerely,
Zhongxing Yang   July 19th 2019

I, the undersigned, hereby represent and warrant that I have authority to grant the permission requested and do grant the permission.

Signature:
Name: MOHAMED HAMZA.

Permission for article [28].

Dear Mr. Yang,
It is our pleasure to grant you permission to use **all or any part of** the ASME paper
"Reconfigurable 3-PRS Parallel Solar Tracking Stand," by Zhongxing Yang; Dan Zhang,
DETC2017-67275, cited in your letter for inclusion in a dissertation entitled NOVEL
DESIGN AND ANALYSIS OF PARALLEL ROBOTIC MECHANISMS to be published by York
University.

Permission is granted for the specific use as stated herein and does not permit further
use of the materials without proper authorization. Proper attribution must be made to
the author(s) of the materials.   **Please note**: if any or all of the figures and/or Tables
are of another source, permission should be granted from that outside source or
include the reference of the original source. ASME does not grant permission for
outside source material that may be referenced in the ASME works.

As is customary, we request that you ensure full acknowledgment of this material, the
author(s), source and ASME as original publisher. Acknowledgment must be retained
on all pages where figure is printed and distributed.

Many thanks for your interest in ASME publications.

Sincerely,

Beth Darchi
Publishing Administrator
ASME

Permission for articles [29] and [30].

Permission for article [31].